

Quantitative fluorescence imaging of the lubricating oil film near microstructures in a sliding-contact tribometer

Von der Fakultät für Ingenieurwissenschaften,
Abteilung Maschinenbau und Verfahrenstechnik der

Universität Duisburg-Essen

zur Erlangung des akademischen Grades

Doktors der Ingenieurwissenschaften

Dr.-Ing.

genehmigte Dissertation

von

Jiyeon Cheong
aus
Seoul (Südkorea)

1. Gutachter: Prof. Dr. Sebastian Kaiser

2. Gutachter: Prof. Dr.-Ing. habil. Lars Zigan

Tag der mündlichen Prüfung: 25.01.2024

Acknowledgements

This thesis was created during my doctoral studies at Mercedes-Benz AG Research & Development center in Ulm and Stuttgart. The university supervision took place at the Institute for Energy and Materials Processes (EMPI, formerly Institute for Combustion and Gas Dynamic, IVG) at the University of Duisburg-Essen.

I would like to express my greatest appreciation to Prof. Dr. Sebastian Kaiser. Without his guidance, expertise and patience, this paper would have never been accomplished. I would like to thank you very much for your great support and understanding over these past four years. I also want to thank Prof. Dr.-Ing. habil. Lars Zigan for his insightful comments and suggestions as the second supervisor.

I am deeply grateful to all my colleagues and fellow students at the tribology group, R&D, Mercedes-Benz AG. I would like to express my sincere gratitude to Dr. Hans-Jürgen Füller for offering me the great opportunity to carry out this research, for his unwavering support at every stage of the project and belief in me. Furthermore, special thanks to my supervisor from Mercedes-Benz AG, Dr. Stefan Wigger for his great guidance and continuous assistance not only in theories but also in practical measurements in the lab, based on his plentiful experience. I learned a lot from you and it was a great honor to work with you during my PhD. My gratitude extends to Andrea Ritzi and Dr. Petra Obert, who shared the office room with me and always gave me invaluable advices on my work as well as daily life in Germany. Moreover, I am grateful to Guntmar Schulz, Dr. Johannes König, Erwin Löffler, Dr. Oliver Essig and Dr. Matthias Martin in our team. I especially thank Jonathan Schöler for the helpful discussions on our common PhD topics. In addition, my appreciation also goes out to my fellow students, Florian Botzenhart and Erkan Akbas for their great support and contribution to this work. From the EMPI at the University of Duisburg-Essen, I would like to thank Matthias Beuting and Julian Heimrath for the cooperation by the temperature measurements at the initial stage and also thank Dr. Daniel Fuhrmann, who introduced this LIF field to me during my master thesis and offered this PhD opportunity after my master degree.

Finally, sincere and warm thanks to my family: to my parents, Seunghee Lee and Gyeongjae Cheong, and my sister Jaeyeon Cheong, for their unconditional love and fundamental support over the physical distance. Last but not least, my acknowledgments definitely belong to my fiancé Innu Park, who was always there for me and made all of this possible. I dedicate this thesis to you.

Lüneburg, November, 2023

Jiyeon Cheong

Abstract

In this work, the oil film thickness and its temperature distribution in an optical tribometer were quantitatively imaged using laser-induced fluorescence (LIF). The optical tribometer was developed as a model experiment for the sliding contact between piston-ring/cylinder liner in an internal combustion engine, and one of the contacting bodies was replaced by a transparent material for optical access.

First, the metal piston ring segment was replaced by a sapphire one to study oil films on the surfaces of the production metal liners. The oil was doped with the laser dye pyrromethene 567 and excited by an Nd:YAG laser at 532 nm. The images clearly showed different oil-filled structures of the liner surface. After an *in-situ* calibration and stray light correction, the minimum film thickness was quantitatively evaluated and compared to the corresponding friction coefficient. Compared to honed cast iron, the pores in a spray-coated liner retained more oil and reduced friction at higher loads.

To further investigate this beneficial oil film behavior near the pores, the cylinder liner was replaced with a glass liner and a micropore – a cylindrical depression with vertical walls – was laser-textured into its surface. The oil film thickness was imaged at a magnification of 5 using a long-distance microscope. The results showed that the pore carried oil to the starved outlet, creating a downstream “oil tail” whose morphology and volume were analyzed. Specifically, at low speed, the pore had a wider tail containing a higher volume of oil than at high speeds. This suggests that in a reciprocating engine, porosity on the liner can result in beneficial tribological behavior particularly around the piston-motion reversal points. An additional measurement using total internal reflection was performed and compared to the “standard” LIF measurement. Furthermore, the detection system with the fluorescence long-distance microscope was applied to an optical single-cylinder engine. This allowed imaging the microscopic oil film behavior within the piston assembly group from the top piston ring to the oil control ring with high magnification and resolution.

In proof-of-concept experiments using the long-distance microscope and the tribometer with a glass cylinder liner without pores, the oil film temperature was imaged using two-dye fluorescence thermometry. To this end, the oil was doped with Lumilux CD 345 and pyrromethene 597 and excited by a blue LED (excitation at about 460 nm). The time-averaged results showed physically plausible temperatures and temperature distributions, while single-shot imaging would need higher pulse energies than available from the LED.

Kurzfassung

In dieser Arbeit wurden die Ölfilmstärke und seine Temperaturverteilung in einem optischen Tribometer mittels laserinduzierter Fluoreszenz (LIF) zweidimensional und quantitativ abgebildet. Das Tribometer wurde als Modellversuch für den Gleitkontakt zwischen Kolbenring und Zylinderbuchse in einem Verbrennungsmotor entwickelt und einer der Kontaktkörper wurde für einen optischen Zugang durch ein transparentes Material ersetzt.

Zunächst wurde das Metallkolbenringsegment durch ein Saphirringsegment ersetzt, um Ölfilme auf der Zylinderwand der serienmäßigen Metalzylinderbuchse zu untersuchen. Das Öl wurde mit dem Laserfarbstoff Pyrromethen 567 dotiert und mit einem Nd:YAG-Laser bei 532 nm angeregt. Die Bilder zeigten verschiedene ölgefüllte Strukturen der Zylinderwand. Nach einer *In-situ*-Kalibrierung und Streulichtkorrektur wurde die minimale Ölfilmstärke quantitativ ausgewertet und mit dem entsprechenden Reibungskoeffizienten verglichen. Im Vergleich zur geschliffenen Grauguss-Zylinderwand banden die Poren auf der thermisch gespritzten Zylinderwand mehr Öl und reduzierten die Reibung bei höheren Belastungen.

Um dieses vorteilhafte Verhalten des Ölfilms in der Nähe der Poren genauer zu untersuchen, wurde im nächsten Schritt die metallische Zylinderbuchse durch eine Glaszylinderbuchse ersetzt und in ihre Oberfläche eine Mikropore – eine zylindrische Vertiefung mit vertikalen Wänden – lasertexturiert. Der Ölfilm wurde mit einem Fluoreszenzfernfeldmikroskop bei einer Vergrößerung von 5 quantitativ abgebildet. Die Ergebnisse zeigten, dass die Pore Öl zum ausgehungerten Auslass transportierte und einen stromabwärts gelegenen „Ölschweif“ bildete, dessen Morphologie und Volumen analysiert wurden. Insbesondere wies die Pore bei niedrigen Geschwindigkeiten einen breiteren Ölschweif auf, der ein höheres Ölvolumen enthielt als bei hohen Geschwindigkeiten. Dies legte nahe, dass bei einem Hubkolbenmotor die Porosität der Zylinderbuchse zu einem vorteilhaften tribologischen Verhalten führen kann, vor allem im Bereich der Umkehrpunkte der Kolbenbewegung. Eine zusätzliche Totalreflexionsmessung wurde dann mit der LIF-Standardmessung verglichen. Das Detektionssystem wurde weiterhin mit dem Fernfeldmikroskop auf einen optischen Einzylindermotor angewendet und ermöglichte die Abbildung des mikroskopischen Ölfilmverhaltens innerhalb der Kolbengruppe vom oberen Kolbenring bis zum Ölabstreifring mit hoher Vergrößerung und Auflösung.

Unter Verwendung des Fernfeldmikroskops und des Tribometers, das mit einer Glaszylinderbuchse ohne Pore ausgestattet war, wurde die Ölfilmtemperatur als Proof-of-Concept-Messung mittels Zweifarbstoff-Fluoreszenzthermometrie abgebildet. Das Öl wurde mit Lumilux CD 345 und Pyrromethen 597 dotiert und durch eine blaue LED (bei ca. 460 nm) angeregt. Die über die Zeit gemittelten Ergebnisse zeigten physikalisch plausible Temperaturverteilungen, während für die Einzelaufnahme höhere Pulsenergien erforderlich wären, als sie die LED bietet.

Contents

Acknowledgements	I
Abstract.....	II
Kurzfassung	III
Contents.....	IV
List of abbreviations and symbols.....	VII
1 Introduction	1
2 Scientific background	3
2.1 Theoretical background.....	3
2.1.1 Fundamentals of Tribology.....	3
2.1.2 Piston assembly group in an engine as tribosystem	7
2.1.3 Fluorescence.....	11
2.2 State of the art.....	18
2.2.1 Oil film thickness measurement.....	18
2.2.2 Surface texturing.....	25
2.2.3 Fluorescence-based temperature imaging in liquid films	29
3 Oil film thickness imaging on the metal cylinder liner.....	32
3.1 Methods	32
3.1.1 Initial setup of the RRV-Tribometer	32
3.1.2 RRV-Tribometer with periscope optic	37
3.1.3 Contact surfaces	39
3.1.4 Experimental parameters and procedure.....	40
3.1.5 Optical system for laser-based oil film thickness measurements	41
3.1.6 Image acquisition	48
3.1.7 Image processing	50
3.1.8 Effect of fluorescence stray light on measured minimum oil film thickness	56
3.2 Results.....	60
3.2.1 Liner surface structures.....	60
3.2.2 2D-imaging of the oil film behavior	61

3.2.3	Minimum oil film thickness compared to the Stribeck curve	65
3.3	Chapter conclusions	67
4	Oil film around a cylindrical micropore visualized by fluorescence microscopy	68
4.1	Methods	68
4.1.1	90° rotated tribometer and redesign	68
4.1.2	Contact surfaces	71
4.1.3	Experimental parameters and procedures	72
4.1.4	Image acquisition	73
4.1.5	Image processing	77
4.1.6	Assessment of the stray light effect	80
4.2	Results	82
4.2.1	Spatiotemporal evolution of the oil tail	82
4.2.2	Influence of sliding speed on the evolution of oil tail volume	83
4.2.3	Influence of sliding speed and load	85
4.2.4	Influence of pore depth	88
4.2.5	Comparison to total internal reflection fluorescence (TIRF)	90
4.3	Application in a single-cylinder optical engine	93
4.3.1	Experimental set-up	93
4.3.2	Results	96
4.4	Chapter conclusions	98
5	Temperature imaging in the oil film by a ratiometric two-color, two-dye fluorescence scheme	100
5.1	Methods	100
5.1.1	Fluorescence excitation and detection for LED-based temperature measurements	100
5.1.2	Experimental arrangement and parameters	103
5.1.3	Image processing including stray light correction and calibration	104
5.2	Results	110
5.3	Chapter conclusions	112
6	Conclusion and future work	113

7	References.....	115
8	Appendix	132
8.1	Redesign, adjustment, and calibration of the 90°-rotated tribometer.....	132

List of abbreviations and symbols

List of abbreviations

Abbreviation	Full description
aTDC	after Top-dead center
BDC	Bottom-dead center (piston position)
BG	Background
BP	Band-pass (filter)
bTDC	before Top-dead center
CA	Crank angle
CAD	Computer-aided design
CCD	Charge-coupled device
CFD	Computational fluid dynamics
CL	Cylinder liner
CMOS	Complementary metal-oxide semiconductor (camera)
Cr-Ni	Chromium-nickel
cts	(Camera) counts
cy	Cycle (one period in the Fourier base functions of the MTF)
det	Detected
DIN	Deutsches Institut für Normung (German), German Institute for Standardization
DKD	Deutscher Kalibrierdienst (German), German Calibration Service
DLC	Diamond-like carbon
DOD	Depth-over-diameter (ratio)
<i>e</i>	Laser pulse energy
FF	Flat-field
FOV	Field of view
FWHM	Full width at half-maximum
GfT	Gesellschaft für Tribologie (German), Tribology Society
GG	Grauguss (German), gray cast-iron
gOTV	(gross) Oil tail volume
He-Cd	Helium-Cadmium (laser)
HPLC	High performance liquid chromatography (pump)

HTHS	High temperature high shear
IC	Internal combustion (engine)
IMEP	Indicated mean effective pressure (engine)
IR	Infrared
ISO	International Organization for Standardization
EMPI	Institute for Energy and Materials Processing
LDS	Lichtbogendrahtspritzen (german), Arc-wire spray-coating
LED	Light-emitting diode
LIF	Laser-induced fluorescence
LP	Long-pass (filter)
MTF	Modulation transfer function
Nd:YAG	Neodymium-doped yttrium aluminum garnet (laser)
norm	Normalized (intensity)
nOTV	(net) Oil tail volume
OCR	Oil control ring
OFT	Oil film thickness
PAO	Poly-alpha-olefin
PIV	Particle image velocimetry
PR	Piston ring
PRS	Piston ring segment
PTU	Programmable timing unit
Pyr	Pyrrromethene (dye)
ref	Reference
RGB	Red, green, blue
Rhd	Rhodamine (dye)
ROI	Region of interest
RRV	Rotations-Reib-Verschleiß (tribometer, German), Rotation-Friction-Wear
SAE	Society of Automotive Engineers
TDC	Top-dead center (piston position)
TIRF	Total internal reflection fluorescence
UV	Ultraviolet
Xe	Xenon

List of symbols

Symbol	Description	Unit
c	Dye concentration	mmol/L
D	Pore diameter	μm
d	Width of unblocked region next to the evaluation area (stray light correction)	mm
F_N	Normal load	N
F_R	Friction force	N
h	Oil film thickness	μm
h_{dep}	Pore depth	μm
I	Intensity (generic)	cts
I_0	Incident light intensity	cts
I_a	Absorption intensity	cts
I_B	Blue channel intensity	cts
I_f	Fluorescence intensity	cts
I_R	Red channel intensity	cts
I_{reflect}	Reflected intensity	cts
I_{sat}	Saturation fluence	mJ/cm^2
I_{scatter}	Scattered intensity	cts
I_{transmit}	Transmitted intensity	cts
n	Refractive index	-
N	Rotational speed	m/s
p	Pore position (center) from the min. PR/CL gap	mm
P	Average load	N
P_R	Frictional power	$\text{N}^*\text{m}/\text{s}$
r_{pivot}	Distance between the pivot point and the PR/CL contact line in tribometer	mm
R	Intensity ratio between the red and blue channels	-
R_q	Root-mean-square roughness	μm
$S_1, S_2\dots$	Electronic singlet states	eV
S_k	Core height	μm
S_{pk}	Reduced peak height	μm
S_q	Root mean square height	μm

s_R	Sliding distance	m
S_{vk}	Reduced valley depth	μm
T	Temperature	$^{\circ}\text{C}$ or K
T_1	First triplet state	eV
t_{cal}	Calibration factor	cts/ μm
v	Sliding speed	m/s
W_R	Frictional work	$\text{N}\cdot\text{m}$
X_{stray}	Proportion of the stray light across the field	-
ε	Absorption coefficient	-
η	Imaging-train detection efficiency	-
η_{vis}	Viscosity	$\text{Pa}\cdot\text{s}$
θ	Incidence angle of the laser (TIRF)	$^{\circ}$
θ_c	Critical angle (TIRF)	$^{\circ}$
λ	Ratio between OFT and surface roughness	-
μ	Friction coefficient	-
σ	Sum of surface roughness	μm
Φ	Quantum yield fraction	-
Ω	Geometric collection efficiency	-

1 Introduction

The issues of dwindling resources, energy- and environmental problems have consistently grown over the last several decades. In this context, the energy efficiency of machines and reliability of mechanical systems have gained significant interest. Part of those can be achieved by reducing friction losses and improving the tribological performance of mechanical components such as bearings, mechanical face seals and piston assembly group in internal combustion (IC) engines. Indeed, friction losses consume 11.5 % [1] of the total fuel energy in a passenger car. Among these, the engine system accounts for 35 % [1] and in an engine, about 45 % [1] of the friction loss occurs in the piston assembly group, which includes the piston rings and the cylinder liner (Figure 1.1).

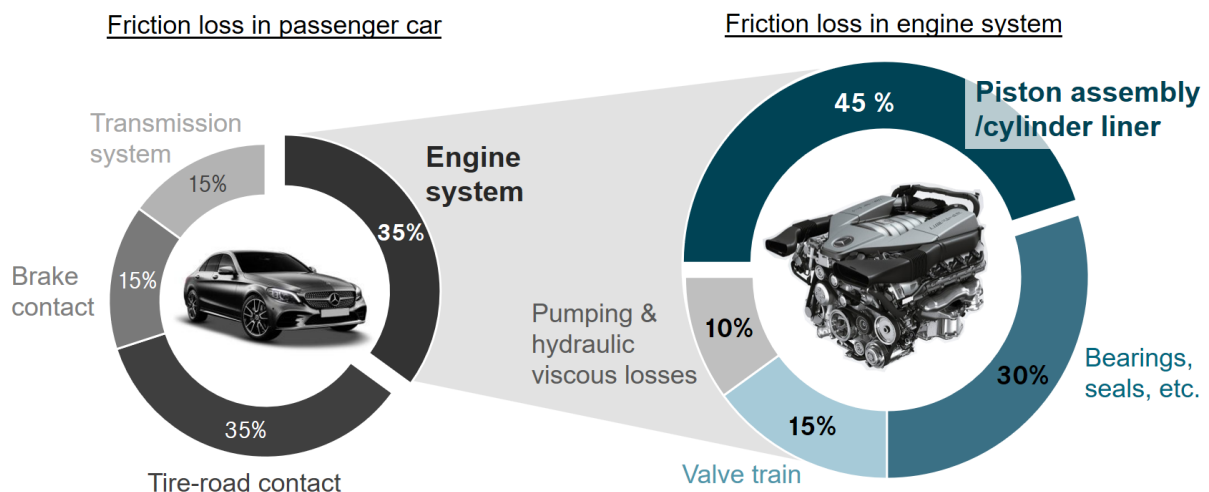


Figure 1.1: Friction loss distribution in a passenger car and an engine system. Based on [1].

Many frictional contacts employ lubricant oil to minimize the friction and wear, to protect metals against corrosion and to wash out contaminants. Thus, the study of the lubricant behavior in such contact under various conditions comes recently more into the focus. For instance, in an IC engine, the oil film thickness (OFT) on the cylinder liner should be maintained in a proper level. Very thin films result in high wear rate of the cylinder liner and a scuffing of the piston rings, while an excessively thick film can enter the combustion chamber to be burned along with fuel, leaving a residue that actually increases friction [2]. Especially near the piston reversal points (top and bottom dead center in an engine), extremely thin OFT and oil starvation have been often reported. For an optimal oil distribution, surface textures can be applied on the frictional contact surfaces including cylinder liners. The approach with surface textures has shown evident benefits: reduced friction [3] and better engine performance [4]. Thermo-mechanical failure in an IC engine, i.e., thermal fatigue and scuffing, is detrimental not only to the engine efficiency but also to the durability of components. This occurs due to the heat from combustion and the friction heat dissipation in the piston-ring/cylinder-liner (PR/CL)

contact. Thus, it is partially avoidable with better insight of the thermal behavior of the oil film in such contact. Despite its significance, a detailed understanding of the oil film behavior remains still incomplete.

In this work, the oil film in the sliding PR/CL contact of an IC engine is reproduced using a rotational tribometer. Visualization of the OFT and the temperature distribution is realized based on laser-induced fluorescence (LIF) of dyed oil. Optical access is achieved by replacing either the piston ring segment (PRS) or the cylinder liner with a transparent material. To quantify the OFT from the LIF image, some image processing methods are developed.

One of the goals of this study is to understand the two or three-dimensional behavior of the oil film on the liner surfaces as they come from the production line, e.g., with honing structures or with fine pores. Via a sapphire PRS and a periscope-like optic, different oil-filled structures of the liner with its real surface properties as well as lubricating phenomena under different operating conditions are investigated. Furthermore, the minimum OFT on the liners is studied with corresponding friction coefficients.

Since the oil film on the spray-coated liner with a porosity has a better frictional behavior, this work further focuses on detailed lubrication mechanisms near a single pore. A micropore was laser-textured into the surface of the glass liner, which rotates against a metal PRS in the tribometer. Fluorescence microscopy enables imaging the pore with a diameter of a few hundred micrometers and investigating its interaction with the neighboring oil film. Additional measurements via total internal reflection fluorescence method support the result and the fluorescence microscope is additionally applied to an optical research engine

Finally, since temperature is an important parameter in viscous flows, the last goal of this research is visualizing the oil film temperature in the PR/CL contact. For that, a two-color/two-dye fluorescence ratiometric scheme is employed with a blue LED (excited at about 460 nm). The temperature distribution of the externally heated oil film is imaged through a glass liner and studied.

2 Scientific background

2.1 Theoretical background

2.1.1 Fundamentals of Tribology

The word, “tribology”, which is derived from the Greek word *tribos* meaning rubbing, was first used in a landmark report by Jost in 1966 [5]. “Tribology is the science and technology of mutually interacting surfaces in relative motion. It encompasses the entire field of friction and wear, as well as lubrication and the corresponding interfacial interactions between solids, between solids and liquids, or between solids and gases”, according to the former standard DIN 50323 and the GfT (Gesellschaft für Tribologie, in English: Tribology society) [6]. The fundamental objects of study in tribology are tribosystems, which are physical systems including all of the materials relevant to the tribological stress and their properties resulting from changes as well as characteristic processes and quantities of the stress. Tribology is one of the significant industrial issues in modern machinery using sliding and rolling surfaces, since the study in that field can minimize and eliminate the losses from friction and wear at all levels of technology and yield long-term reliability and cost savings.

Friction

Friction is the resistance to motion during sliding or rolling, when one solid body moves tangentially over another with which it is in contact. Figure 2.1 shows different types of friction. Each is described below [5] [7].

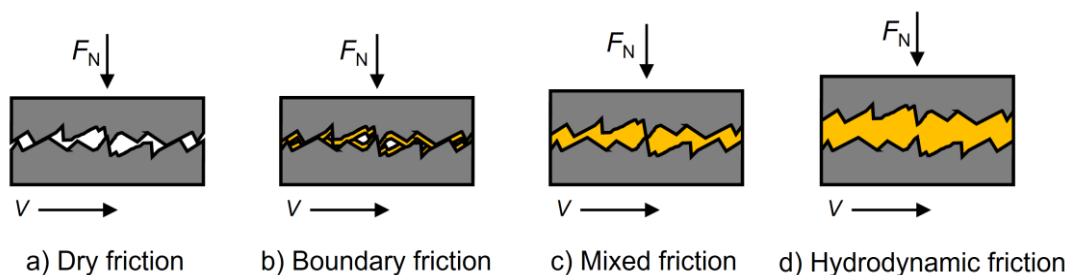


Figure 2.1: Different types of friction.

a) *Dry friction* is the tangential component of the direct contact force that exists when two dry surfaces (tend to) move relative to one another without lubricant.

b) *Boundary friction* is the condition in which the solid surfaces are so close together that surface interaction between monomolecular or multimolecular films of lubricants (liquids or gases) and the solid asperities dominate the contact.

c) *Mixed friction* is the transition between the boundary and hydrodynamic friction. A part of the surface is supported by the partial hydrodynamic film, but the solid contacts still occur.

d) *Hydrodynamic friction* separates the surfaces with an enough lubricant film layer capable of withstanding the normal pressure, thereby avoiding the possibility of asperity contact.

Figure 2.2 shows a free-body diagram of a solid body stressed by normal and tangential forces on a plane.

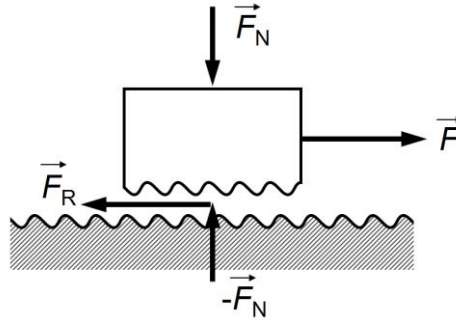


Figure 2.2: A solid body stressed by normal and tangential forces on a plane. The reaction force and frictional force can be also seen. The roughness of the contact surfaces is exaggeratedly illustrated. Based on [5] [8].

If the tangential force F is sufficiently small, the body does not move (static friction). Friction force F_R arises in part from the interactions of the roughness or asperities of the contacting surfaces. Once the body begins instantly to move, the frictional resistance generally decreases (dynamic friction) from the static friction force. In this work, only the case of the dynamic friction is discussed. The friction force F_R is proportional to the normal force F_N , the proportionality constant being the friction coefficient μ .

$$F_R = \mu \cdot F_N \quad (2.1)$$

The frictional work of a relative movement W_R with a sliding distance s_R leads to conversion of the mechanical energy into heat.

$$W_R = F_R \cdot s_R \quad (2.2)$$

The power lost resulting from this frictional process is referred to as a frictional power P_R :

$$P_R = F_R \cdot v \quad (2.3)$$

where v indicates the sliding speed.

Wear

Wear is the surface damage or removal of material from one or both of two solid surfaces in a sliding, rolling, or impact motion relative to one another. In most cases, wear occurs through surface interactions at asperities [5]. Its basic mechanisms and micro-effects are shown in Figure 2.3. These can occur individually, successively or concomitantly.

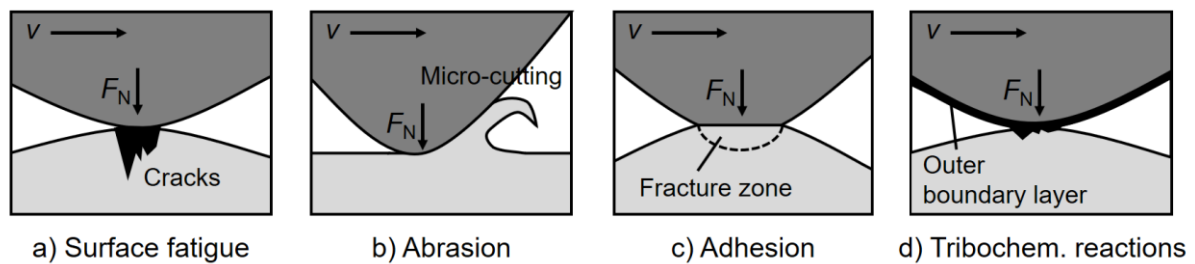


Figure 2.3: Basic wear mechanisms and micro effects. Based on [9].

a) *Surface fatigue* is the cracking, crack growth and subsequent pitting of surfaces subjected to alternating loads and stresses in near-surface zones of the base body and counterbody. Fatigue wear occurs from the detachment of wear particles by cyclic crack growth.

b) *Abrasion wear* is the removal (i.e., micro-cutting) of a softer material surface by a harder material impinging on or sliding against the surface under load. In the case of most metals and alloys, a plastic deformation is predominant, though a brittle fracture can be caused.

c) *Adhesion wear* occurs when the atomic bonding forces (microwelds) between the materials on the interface of the base- and counterbody are stronger than the strength of the surrounding area in either of the materials at the asperity contacts with possibly broken protective surface layers [10]. As the sliding continues, it may result in the fracture by a fatigue procedure.

d) In *tribochemical reactions*, the tribological stress on the surface induces chemical reactions on the interface of the base- and counterbody with elements of the lubricant or ambient medium. The property of the surfaces may be altered and it can yield the brittle chipping or even reduce the friction and wear.

The Stribeck curve

The Stribeck curve is a graphical representation of the frictional characteristics in fluid-lubricated contacts, including the boundary, mixed and hydrodynamic lubrication regimes. Stribeck [11] [12], Gümbel [13] and Hersey [14] studied the journal bearing frictions and contributed to the discovery of the Stribeck curve, which commonly plots the friction coefficient as a function of a dimensionless Hersey number.

$$\text{Hersey number} = \frac{\eta_{vis} N}{P} \quad (2.4)$$

Hersey showed that the friction due to the viscous shear is a unique function of the product of viscosity (η_{vis}) by rotational speed (N) divided by the average load (P), which is called Hersey number. A typical Stribeck curve is schematically shown in Figure 2.4. The indicated lubrication regimes are relevant as well to the friction types described in Figure 2.1.

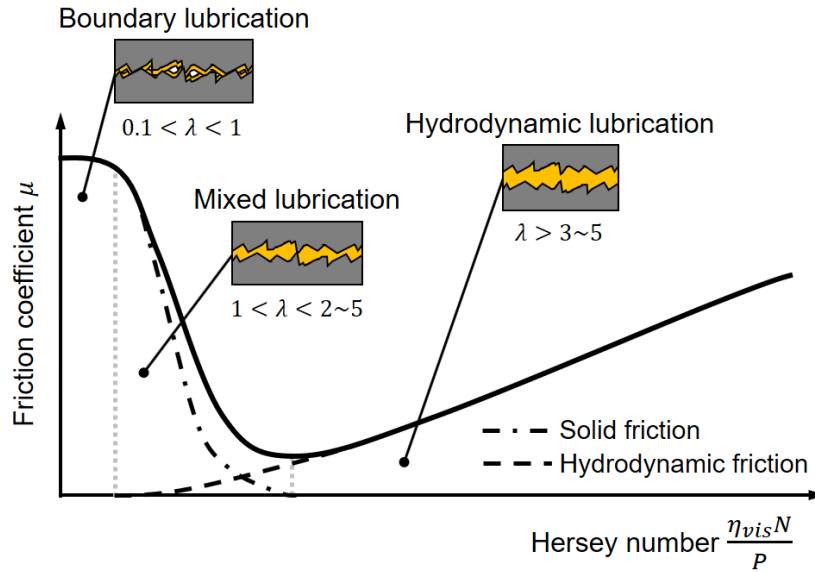


Figure 2.4: Typical Stribeck curve with lubrication regimes.

Alternatively, a dimensionless ratio λ between the oil film thickness (h) and the surface roughness (σ) can alter the horizontal axis of the Stribeck curve.

$$\lambda = \frac{h}{\sigma} \quad (2.5)$$

where $\sigma = \sqrt{R_{q,1}^2 + R_{q,2}^2}$ is the sum of the surface roughness of both surfaces ($R_{q,1}, R_{q,2}$).

At the boundary lubrication regime, the solid surfaces are under the direct asperity contact, the load is supported mainly by the surface asperities and it shows high friction. Here, the λ is in a range of 0.1 to 1. The mixed lubrication regime is a transition period or the combination of the boundary and hydrodynamic regimes. The friction coefficient generally decreases to the minimum point and $1 \leq \lambda \leq 2 \sim 5$ corresponds to this regime. The lubrication between the piston rings and liner contact in the vicinity of top- and bottom dead centers (TDC, BDC) is mostly found at the boundary- and mixed regime. In the hydrodynamic lubrication regime, the asperity contact is negligible, since the surfaces are largely separated by the fluid. The load is mainly supported by hydrodynamic pressure and the friction is mostly caused by the viscous dissipation. The corresponding λ is above 3~5. The friction coefficient increases with increasing Hersey number, but the increasing rate is smaller than the decreasing rate in the mixed regime. The surface contacts within the piston rings and the liner around midstroke are relevant to this regime [15] [16] [17].

2.1.2 Piston assembly group in an engine as tribosystem

An internal combustion engine converts thermal energy into mechanical work, generally through a reciprocating motion. Combustion of the air/fuel mixture generates thermal energy inside the engine cylinder. Figure 2.5 shows a schematic overview of the basic components of a common four-stroke engine and the piston assembly group.

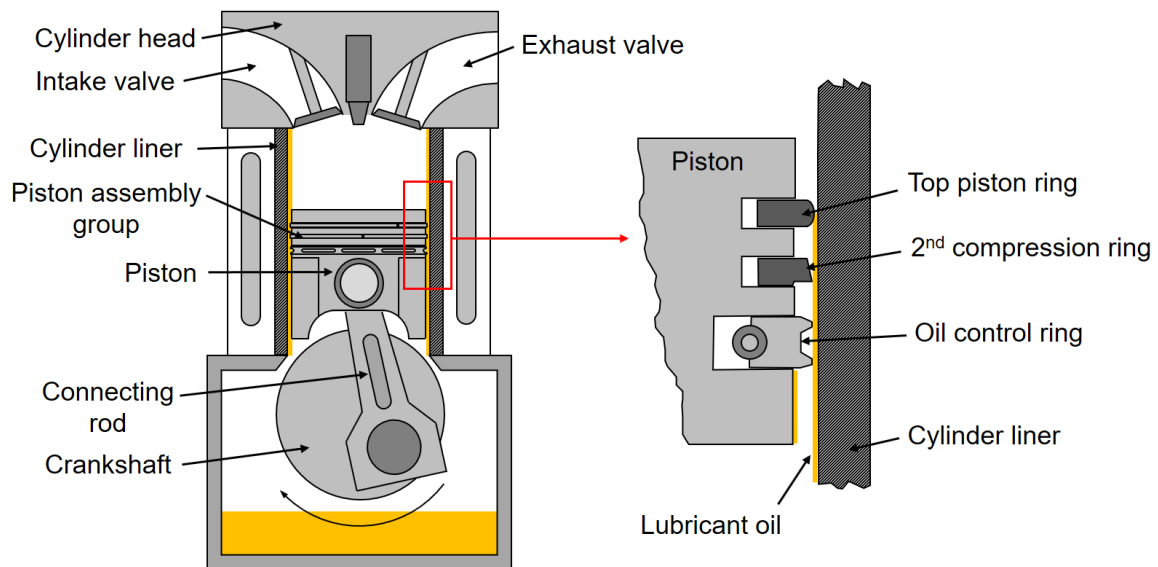


Figure 2.5: Schematic overview of the basic components of the common four-stroke engine (left) and the piston assembly group (right). Based on [18].

During a stroke, the piston in the cylinder liner moves from the TDC to the BDC or vice versa. A connecting rod attached to the piston transfers the reciprocating motion to the rotation of the crankshaft. The cylinder head contains the intake valves, which open to let the cylinder be filled with fresh air and the exhaust valves that allow the combustion gases to escape. The piston assembly group includes typically three piston rings in grooves in the outer diameter of the piston. Engine oil lubricates the surface between the piston rings and the cylinder liner. These components are discussed more in details below.

Piston rings

The piston rings play a significant role in the efficiency and performance of the IC engine. Their main function is to seal the combustion chamber and to prevent its loss of gases into the crankcase so that expansion in the combustion process is able to deliver maximum work to the piston. An insufficient sealing of the piston rings against the cylinder wall would result in excessive blow-by, which is the leakage of the gas from the combustion chamber, and it decreases the engine efficiency as well as damages the lubricant oil [19]. Since a part of the combustion chamber heat energy is transferred through the piston to the piston boundaries, i.e. the piston skirt and rings, the secondary role of the piston rings is cooling the piston crown

by conducting heat away from the piston to the cylinder wall, in which it can be transferred out of the engine by the cooling system. Third, the piston rings maintain the proper amount of oil flow between the piston and the cylinder wall by scraping oil from the cylinder wall back into the sump during the downstroke. It prevents excess lubrication oil from moving into the combustion chamber. The piston rings are located in the ring grooves on the piston circumference as shown in Figure 2.5 (right), where they are free to rotate, twist and undergo limited axial movement.

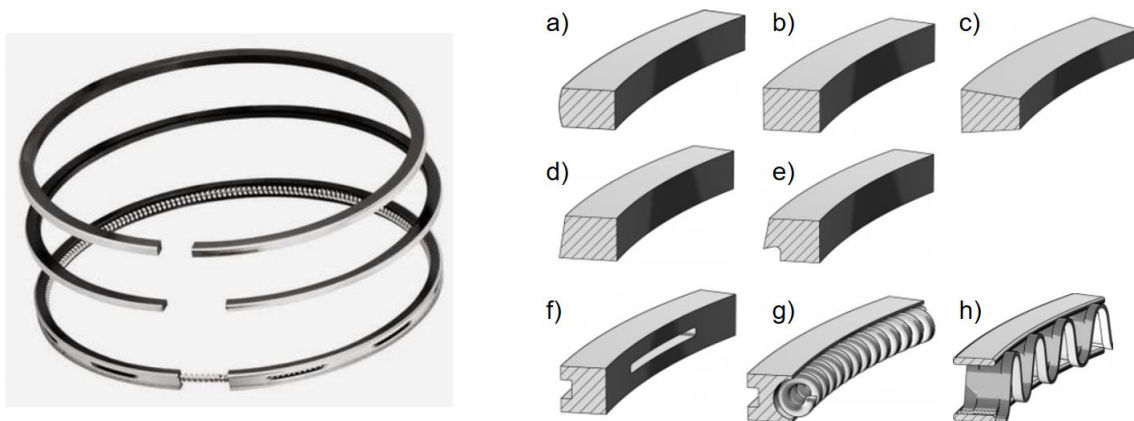


Figure 2.6: Typical ring pack (left) and piston ring types (right). a-e) Compression ring. f-h) Oil control ring. [20]

In general, a modern engine for a passenger or commercial vehicle uses three piston rings as shown in Figure 2.5 (right) and Figure 2.6 (left); and they are referred to as a ring pack. Each ring in the pack has different characteristics in design for its function: (1) the top piston ring (compression ring) has typically a barrel shape (Figure 2.6a) on the contact surface and it is typically coated with wear-resistant coatings such as chromium or plasma-sprayed molybdenum. Its main function is a gas seal between the piston and the liner wall. Its free diameter is larger than the cylinder bore, it is open at one location, at the ring gap (Figure 2.6 left), and has a given mounting pretension. A barrel faced, rectangular, keystone and taper faced rings in Figure 2.6b-d respectively can be used as a top piston ring. (2) The second compression ring acts also as a gas seal, but generally performs an additional significant role in the control of oil flow. It is normally taper faced (Figure 2.6d) or stepped (Figure 2.6e). (3) The oil control ring (OCR) does not have any gas sealing function but regulates the oil flow to the other rings in the ring pack. It has two narrow contact rails loaded against the cylinder wall usually by means of a coil spring which is incorporated into the back of the ring. This ring has slots in the peripheral region, through which the excess scraped oil can drain away into the crankcase. A single-piece OCR, such as a slotted OCR in Figure 2.6f, two-piece OCR like a coil spring loaded slotted OCR in Figure 2.6g and three-piece OCR, e.g., MF system with an expander-spacer consists of a Cr-Ni steel strip in Figure 2.6h are usually used. [21] [22]

Cylinder liner

Traditionally, the cylinder liners (sleeves) are produced from cast iron and inserted into the engine block, which is often aluminum, to form the inner wall of the cylinder. The classic lamellar graphite cast iron is inexpensive, stable and offers good machinability, however the liner's relatively thick thickness yields a weight disadvantage. To its surface, a machining process known as honing is typically used to improve the geometric form of the surface and the surface finish. The grooves from the honing process are expected to control the amount of oil available in the contact by retaining the oil inside and distributing it more evenly as well as to prevent a high wear rate of the surface by collecting the wear debris. A honing stone composed of abrasive grains is used to the honing process. This is usually turned in the bore while being moved in and out to generate a typical cross-hatch pattern on the inner surface of the cylinder liner. A typical honing process and the resulting surface structure are shown in Figure 2.7.

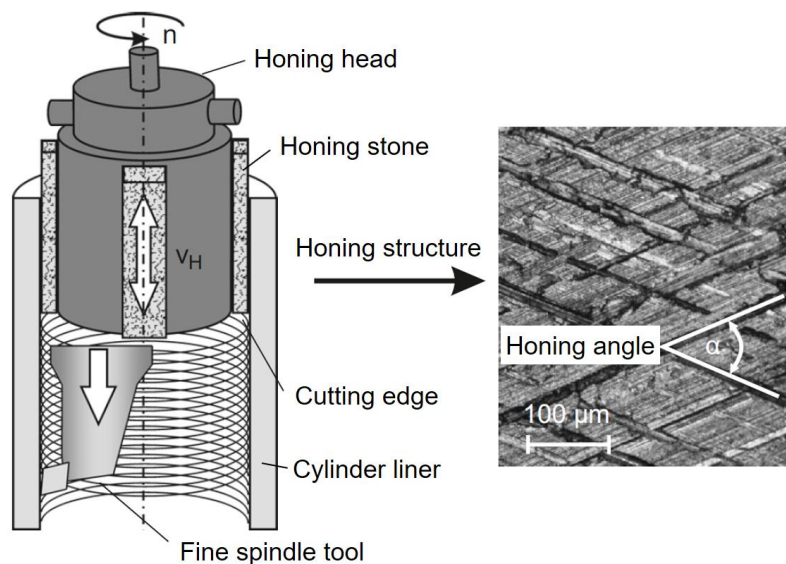


Figure 2.7: Honing process in the cylinder liner and resulted surface structure with a cross-hatch pattern [23].

Alternatively, without a sleeve, a wear-resistant coating such as Nikasil® or thermal-sprayed bores can form the cylinder wall. Mercedes-Benz AG developed the NANOSLIDE® technology (Figure 2.8) including a twin wire arc spray process, i.e., arc spraying melts iron/carbon wires with a high temperature up to 6500°C and sprays them through compressed air and nozzle finely onto the cylinder surfaces of the aluminum cylinder block as shown in Figure 2.9. In this work, the cylinder liner produced with this process is called “LDS liner” (LDS in German: Lichtbogendrahtspritzen). Additionally, honing is used as the final step to create a smooth surface. As a result, the surface has a fine porosity with a mirror-like finish [24] [25]. This can

reduce the engine weight and is expected to decrease friction loss in a piston assembly group in comparison with gray cast iron liners as well as wear rate and exhaust-gas emission [1] [26].

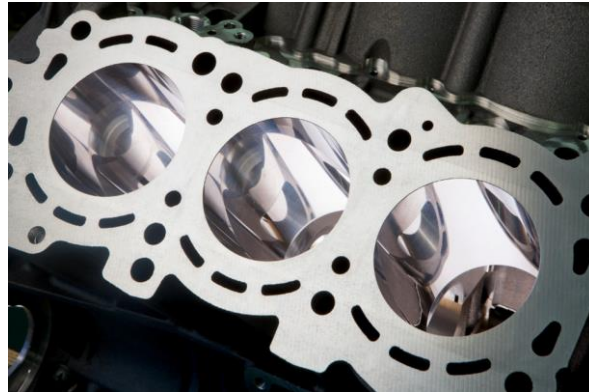


Figure 2.8: Cylinder crankcase with NANOSLIDE® technology [25]. Printed with permission of Springer Nature BV.

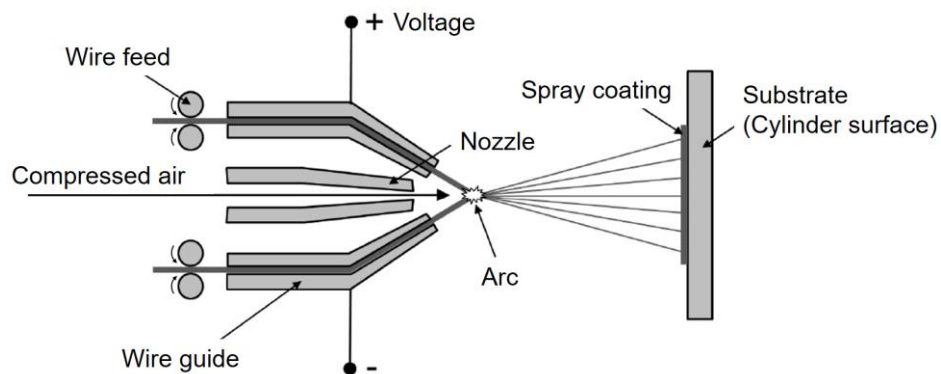


Figure 2.9: Twin arc-wire spray coating process [27].

Engine oil

In a piston assembly group, the engine oil lubricates the contact surface between the components. It is composed of two main components — base oil and additives. The main role of the engine oil is to separate and lubricate the engine's moving parts. It thus reduces the friction and engine wear. It also helps to remove the heat that is generated through the combustion and friction between mechanical parts via the lubrication circuit. In addition, it removes dirt and microscopic deposits from the combustion residue to prevent clogging of the engine. The engine oil flow continuously carries impurities to the oil filter, where they are trapped. It also has the ability to prevent or minimize internal component corrosion, which can damage metal parts in an engine. This is carried out by chemically neutralizing corrosive products or by forming a barrier between the components and the corrosive material with the help of additives. Finally, it also acts as a dynamic seal. A protective layer is deposited between the various parts, sealing any clearances that may arise. At the end, the proper usage of the engine oil allows a longer lifespan of the engine, enhances the engine's performance and its

fuel efficiency as well as decreases CO₂ emission. Usually, the additives in the engine oil account for 15 to 25 percent by weight [28] and they include among other things: dispersants, detergents, anti-wear additives, friction modifiers, antioxidants, anti-foam additives, corrosion inhibitors, viscosity index improvers and pour point depressants [29].

Engine oils can be classified and rated by their grade and viscosity with a numerical code system from the Society of Automotive Engineers (SAE). An oil can either be single-grade, with a set viscosity level, or multi-grade, where the oil can act at two different viscosities depending on its temperature. According to the SAE viscosity rating system, lower number of an oil indicates higher viscosity, i.e., thicker oil, and vice versa. When the oil is multi-grade, it can be designated, for example, 10W-30, which is a common multi-grade oil. The first number '10W' is the equivalent grade of the single grade oil that has the oil's viscosity at cold temperature (for winter) and the second number is the grade of the equivalent single-grade oil that describes its viscosity at 100 °C. On the other hand, engine oils are increasingly having to perform in high temperature high shear (HTHS) environments within the engine and thus, the HTHS viscosity becomes the current industry standard that best predicts the lubricant behavior. HTHS measures the viscosity (resistance to flow) of an engine oil at elevated temperatures (150°C) under constant shear, simulating the narrow tolerances and high speeds between moving parts in a hot engine. Here, the lower the measured torque, the lower the HTHS viscosity, which yields a higher fuel efficiency. A typical HTHS viscosity of the engine oil is about 2 - 4 mPa*s.

2.1.3 Fluorescence

Fluorescence is a photophysical process, in which the absorbed laser light (i.e., a photon) causes the excitation of a molecule to the higher electronic energy state, and its return to the electronic ground state also occurs with emission of a photon [30]. The process between the absorption and emission of the light is often described by the Jablonski diagram (Figure 2.10).

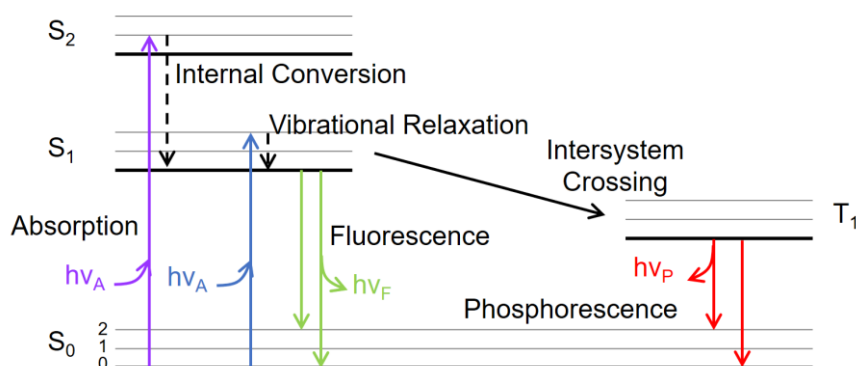


Figure 2.10: Jablonski diagram [31] showing the process between the absorption and emission of light.

Each thick black line and S_i (i = 0, 1, 2) indicate a singlet state, where all electrons in the

molecule are spin-paired. The singlet ground, first, and second electronic states are described by S_0 , S_1 , and S_2 , respectively. At each of these electronic energy levels, the molecules can exist in a number of vibrational energy levels, depicted by 0, 1 and 2 and thin gray line. Absorption and emission occur mostly from the molecules with the lowest vibrational energy. When the molecules are illuminated by the proper wavelength of light, the light is absorbed and the molecules are excited with an energy $h\nu_A$ to the higher vibrational level of either S_1 or S_2 from the ground state S_0 in a very short time of about 10^{-15} s. Normally, the molecules in condensed phases rapidly relax to the lower vibrational level within the same electronic state in 10^{-12} s and this process is called *vibrational relaxation*. The molecules in a higher singlet electronic state can also undergo *internal conversion* to a lower lying singlet electronic state, which is followed immediately by vibrational relaxation to the lowest vibrational level of the electronic state. From that state, the molecules may transition to one of the vibrational energy levels of the ground state S_0 , emitting photons with energy equivalent to the energy difference of the transition $h\nu_F$, which is fluorescence. This is mostly red-shifted, i.e., has longer wavelengths than the absorption wavelength. It is shown in Figure 2.11, which is typical absorption- and emission spectrum of an often-used fluorescent dye, Rhodamin B.

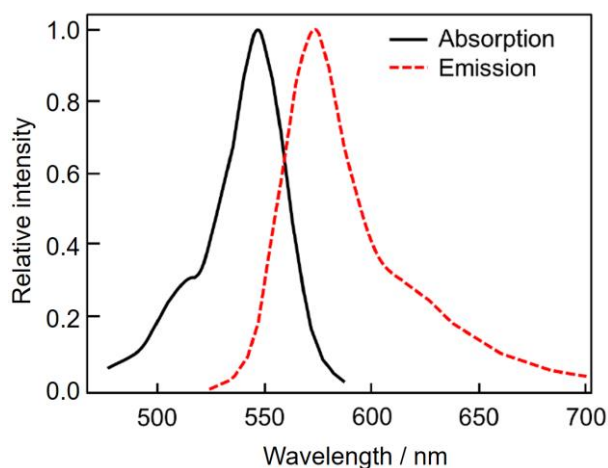


Figure 2.11: Typical absorption- and emission spectrum of a dye, Rhodamin B. Based on [18].

Its duration is on a time scale of nanoseconds (10^{-9} to 10^{-8} s). As an alternative, electrons in the S_1 state can also undergo *intersystem crossing*, which is a spin conversion to the first triplet state T_1 . This yields phosphorescence, an emission from T_1 , which has generally longer wavelengths (lower energy) and much longer duration (10^{-6} to 10^{-3} s) than fluorescence [31] [32].

Dye

In fluorescence diagnostics, two different approaches concerning the fluorophore are distinguished. In the first case, fluorescence is excited in a chemical species naturally present in the sample. (In biology, this is often called “autofluorescence”). Generally, this approach can

be used only for a qualitative measurement, not for quantitative one, because considerable number of fluorescing species which are unknown gives rise to highly undetermined fluorescence signal. For example, some typical commercial fuels, such as gasoline, diesel and kerosene, are included in this case. For quantitative analysis, it is desired to replace the fluorescing components of fuel by non-fluorescing surrogate components, either only except one single fluorescing component or as adding one additional fluorescing compound which was not included in original fluid. About this single species, the function of the external condition, such as pressure or temperature, should be known for a quantitative calibration. The second case is that the fluid of interest does not show measurable fluorescence. For this kind of fluid, one or multiple dyes can be selectively added in a low concentration not to disturb chemical properties of original fluid.

For quantitative fluorescence imaging of the oil film, organic molecules are commonly used as fluorescent tracers. In particular, pyrromethene (pyr) and rhodamine (rhd) dyes were successfully employed, because of their low triplet extinction coefficients, high quantum efficiencies, well-known spectral features, pH, and temperature dependencies, as well as their photochemical robustness [33] [34] [35] [36]. Thirouard [37] investigated these dye families for the LIF imaging of the oil film in a research engine that are soluble in oil and can be excited by the second harmonic of an Nd:YAG laser (532 nm). The considered dyes were pyr 567, pyr 597, pyr 650, rhd 590, rhd 610 and rhd 640. One of the pyrromethene family was combined with one of rhodamine family to compensate their intensity dependence on the temperature using a dual emission method. In the end, he chose the dye combination of pyr 567 and rhd 640 with a concentration of 0.1 mmol/L for each dye. As mentioned in chapter 2.2.1, some other authors also selected this dye combination [18] [38] [39] for similar reasons or a single dye of rhd B [40], rhd 6G [41] or pyr 567 [42].

Laser

The laser (light amplification by the stimulated emission of radiation) is a typical light source for fluorescence excitation (laser-induced fluorescence, LIF). It is a device that can produce a highly directional, intense, monochromatic and coherent beam [43]. Among some commercial lasers, an Nd:YAG (neodymium-doped yttrium aluminum garnet) laser is used in chapters 3 and 4. The Nd:YAG laser is optically pumped using a flashtube or laser diodes and initially emits light with a wavelength of 1064 nm, in the infrared [44]. It has different options for harmonic generation to emit typically 532 nm, 355 nm or 266 nm light, and in this work, a second harmonic generator is used to emit 532 nm laser light, which is a green-color beam.

LED

A light-emitting diode (LED) has been often employed in the fluorescence technique as a good alternative light source instead of lasers, since it is relatively less expensive and easy to use.

It is a semiconductor device that emits light when an electric current is passed through it. When the particles that carry the current (i.e., electrons from the N-side and holes from the P-side) combine within the semiconductor material, the energy is released in the form of light and heat. LEDs are solid-state devices, where the light is generated within a semiconductor material. Thus, it is distinguished from other lighting technologies using heated filaments (incandescent and tungsten halogen lamps) or gas discharge (fluorescent lamps). The electrons and holes inside the semiconductor of the LED are contained within energy bands. The bandgap (separation of the bands) determines the energy of photons, that is the emitted spectrum by the LED, and hence its color [45]. Modern LEDs are available throughout all the wavelength range from ultraviolet (UV), visible to infrared (IR). LEDs are less expensive than lasers, robust, consume lower energy, have longer lifetime and a compact size. The operation of a pulsed LED allows also overdriving, i.e., currents above the damage threshold, which is given by the manufacturer and relatively low without a pulsed operation. On the other hand, LEDs are neither spectrally coherent nor monochromatic compared to lasers; however, they show sufficiently narrow emission spectrum in comparison to the halogen lamps or gas-discharge lamps. In general, the maximum brightness of LED is lower than that from the typical laser and it has lower power than a laser. Nevertheless, it has been used instead of lasers in some measurements of Mie scattering [46] [47], DBI (diffuse back-illumination) imaging [48] [49] and schlieren imaging [50] [51]. In this work, the LED is employed as a light source in chapter 5.

Fluorescence for film thickness measurement

Beer-Lambert's law describes the decrease in intensity as light passes through an absorbing medium, for example one containing dyes, as shown in Figure 2.12.

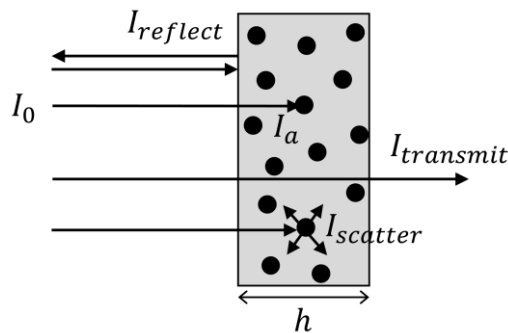


Figure 2.12: Light interaction with an absorbing medium relative to the Beer-Lambert's law.

When the incident light (I_0) enters the absorbing medium, a part of the light can be reflected ($I_{reflect}$), scattered ($I_{scatter}$), transmitted ($I_{transmit}$) or absorbed (I_a):

$$I_0 = I_{reflect} + I_{scatter} + I_{transmit} + I_a \quad (2.6)$$

where I indicates the light intensity. With the assumption that reflection and scattering is negligible, the absorbed light intensity I_a is

$$I_a = I_0 - I_{transmit}. \quad (2.7)$$

According to the Beer-Lambert's law, the transmitted light intensity $I_{transmit}$ is a function of the absorption coefficient ε , the dye concentration c , and the oil film thickness h :

$$I_{transmit} = I_0 e^{-\varepsilon ch}. \quad (2.8)$$

A fraction Φ (the quantum yield) of the absorbed light is re-emitted as fluorescence with intensity I_f .

$$I_f = \Phi I_a = \Phi I_0 (1 - e^{-\varepsilon ch}). \quad (2.9)$$

If the OFT h is thin and the dye concentration c is low, a linear approximation may sufficiently accurately relate the detected intensity $I_{f,det}$ and h ,

$$I_{f,det} = \Omega \eta I_f = \Omega \eta \Phi I_0 \varepsilon ch \quad (2.10)$$

where $\Omega \eta$ is the detection efficiency described as the product of geometric collection efficiency and imaging-train detection efficiency, respectively. This detection efficiency may vary across the image and needs to be determined from so-called "flat fields" in separate calibration experiments. According to the equation (2.10), the local OFT where a dye is mixed with an oil can be deduced from the ratio between the measured fluorescence intensity and the reference fluorescence intensity of the known OFT, when the other parameters are constant.

Fluorescence for temperature measurements

Two-color/two-dye ratiometric scheme for measuring the temperature distribution in chapter 5 is based on the different temperature dependence of the fluorescence intensities of two dyes. With the employed dye combination in chapter 5, an emission reabsorption can occur principally, since the emission spectrum of the dye 1 overlaps the absorption spectrum of the dye 2 (Details are discussed in chapter 5.1.1). According to Hidrovo [38], this has two effects: (1) *it increases the fluorescence emission of the dye 2 as, in addition to the external light source excitation, it is being excited by the fluorescence of the dye 1.* (2) *The fluorescence emission of the dye 1 is reduced since it is being reabsorbed by the dye 2.* He however argued that the first effect can be mostly neglected, because the external illumination intensity in LIF (with laser) is generally much greater than dye fluorescent emission. Unlike his argument, an LED is used in chapter 5 as a light source instead of a laser with much lower illumination intensity. Thus, we here consider the first effect as well and this is depicted in Figure 2.13.

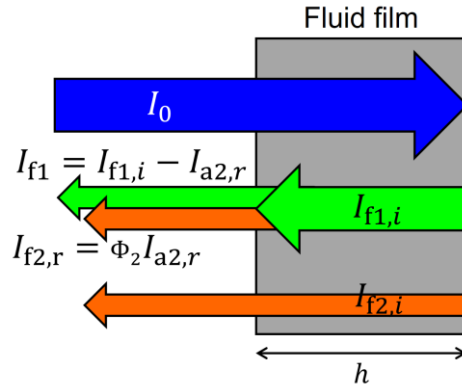


Figure 2.13: Principle of the fluorescence from the fluid film mixed with two dyes. Emission reabsorption occurs with the dye 2.

Each dye's fluorescence intensity detected through the filter 1 and filter 2 (for detecting the dye 1 and 2, respectively) can be calculated from the equation (2.9):

$$I_{f1,det} = \eta_1(I_{f1,i} - I_{a2,r}) = \eta_1 I_{f1,i} e^{-\varepsilon_2 c_2 h} = \eta_1 \Phi_1 I_0 (1 - e^{-\varepsilon_1 c_1 h}) e^{-\varepsilon_2 c_2 h} \quad (2.11)$$

$$\begin{aligned} I_{f2,det} &= \eta_2(I_{f2,r} + I_{f2,i}) \\ &= \eta_2(\Phi_2 \Phi_1 I_0 (1 - e^{-\varepsilon_1 c_1 h})(1 - e^{-\varepsilon_2 c_2 h}) + \Phi_2 I_0 (1 - e^{-\varepsilon_2 c_2 h})) \end{aligned} \quad (2.12)$$

where η denotes each dye-relative detection efficiency within each filter, i subscript is the one excited from the incident light and r subscript is the reabsorption. However, according to Hidrovo [38] [52], for reabsorption to play a significant role on the fluorescence (in its own thickness), the system must be optically thick. Whereas, our system in chapter 5 is optically thin (will be shown in chapter 5.1.3) and thus, when the h approaches zero, those can be approximated without reabsorption as:

$$I_{f1,det} = \eta_1 \Phi_1 I_0 \varepsilon_1 c_1 h \quad (2.13)$$

$$I_{f2,det} = \eta_2 \Phi_2 I_0 \varepsilon_2 c_2 h. \quad (2.14)$$

Their intensity ratio R is expressed as:

$$R = \frac{I_{f2,det}}{I_{f1,det}} = \frac{\eta_2 \Phi_2 \varepsilon_2 c_2}{\eta_1 \Phi_1 \varepsilon_1 c_1} \quad (2.15)$$

which implies that the intensity ratio is independent on the fluid film thickness. Thus, this method can be employed to measure the film temperature without film thickness information [38]. For better insight, when we expand the h range to the optically thick region, the equations (2.11), (2.12) and their ratio can be schematically depicted as in Figure 2.14.

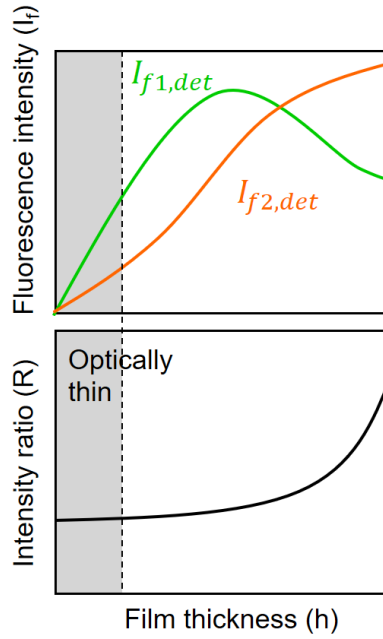


Figure 2.14: Fluorescence intensity of each dye in a function of the film thickness (top) and their intensity ratio (bottom). Optically thin region is marked with a gray color.

In the full range of the film thickness, the reabsorption plays a significant role in the optically thick region as stated by Hidrovo and the film thickness information is contained in the intensity ratio. Hence, he suggested to use this region to measure the film thickness with a ratiometric scheme. Our system is optically thin as will be shown in chapter 5.1.3, hence we can employ the same method from [38] to measure the film temperature in this work. When the absorptivity of the dye 2 is a function of temperature T (decrease of absorptivity with temperature),

$$\varepsilon_2(T) = \varepsilon_{2,0} - kT \quad (2.16)$$

where $\varepsilon_{2,0}$ is dye 2 absorption coefficient at zero temperature reference value and k is molar absorption coefficient temperature dependence proportionality constant [38]. We can rewrite the equation (2.15) as:

$$R(T) = \frac{\eta_2 \Phi_2 c_2}{\eta_1 \Phi_1 \varepsilon_1 c_1} (\varepsilon_{2,0} - kT) = A - BT \quad (2.17)$$

where

$$\frac{\eta_2 \Phi_2 c_2}{\eta_1 \Phi_1 \varepsilon_1 c_1} \varepsilon_{2,0} = \text{constant} = A \quad (2.18)$$

$$\frac{\eta_2 \Phi_2 c_2}{\eta_1 \Phi_1 \varepsilon_1 c_1} k = \text{constant} = B. \quad (2.19)$$

With this equation, the temperature in fluids can be determined, when A and B are known from a calibration experiment.

2.2 State of the art

2.2.1 Oil film thickness measurement

The lubricant film distribution as well as its thickness plays an important role in reducing friction losses in a mechanical device with a sliding contact, such as a PR/CL assembly of an IC engine. Thus, there have been lots of efforts to understand the lubricant film's behavior and dynamics in the contact better. Particularly interesting are quantitative measurements of the OFT as well as qualitative visualization of the lubricant distribution on a tribometer or a cylinder liner. Previous experimental methods for measuring the OFT in such contact can be roughly categorized into electrical techniques and optical techniques.

Electrical techniques

- *Capacitance method:* The capacitance of two parallel separated metal plates varies in inverse proportion to their separation. The measurement of the capacitance in a two-plate combination of this type has been used as the basis for industrial proximity transducers. Hamilton et al. [53] designed and embedded small flat capacity gauges in the cylinder liner of diesel engine; and observed OFT in the range of 0.4 – 2.5 μm .

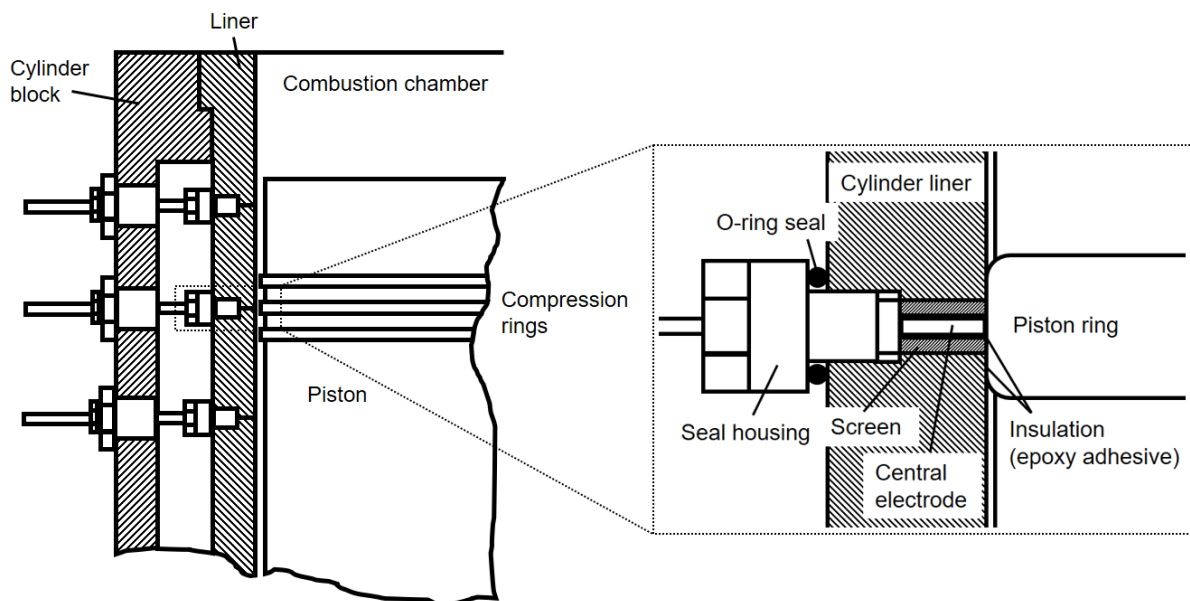


Figure 2.15: View of cylinder block of AV1L diesel engine showing assembly and position of capacitance gauges, based on Hamilton et al. [53].

On the other hand, Shin et al. [54] fixed the capacitance transducers in the piston ring allowing OFT to be measured over the complete piston stroke and the measured OFT was about 0.7 μm . Brown et al. [55] and Moore et al. [56] studied in this method the inlet starvation of the compression rings. In addition, Moore et al. [57] reported the detailed oil film close to TDC using this method. Mattsson [58] also measured the OFT between PR/CL in a heavy duty

2. Scientific background

directly injected diesel engine using the electrical capacitance and observed a gas pocket appearing between top-ring/liner at increasing speeds and loads.

- *Inductance method*: Inductive proximity sensors employ the electromagnetic coupling that occurs between a wire coil and a magnetic material. With an alternating current applied to the wire coil, eddy currents are induced in the material. The inductance depends on the proximity of the material and thus, the distance between the PR/CL can be evaluated by the inductance transducer. Wing and Saunders [59] placed self-inductance transducers behind a ring in a diesel engine and recorded the distance between the piston and the back of the ring to deduce the OFT indirectly, since the transducers were too large to be embedded in the ring. Dow et al. [60] mounted an inductance sensor in the end face of the ring in a motored rig and monitored changes in the ring gap. This enabled the circumferential average OFT to be estimated, but only with the knowledge of the cylinder and ring expansion's influences on the ring gap. Later, Tamminen et al. [61] located inductance sensors in the liner of a medium-speed diesel engine and measured OFT with different loads.

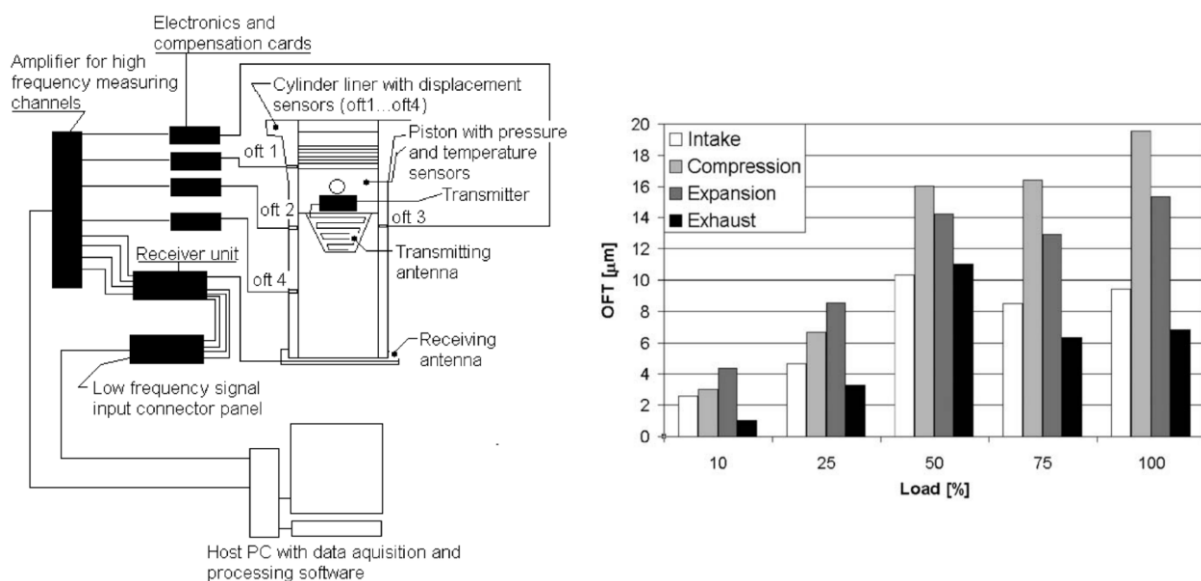


Figure 2.16: Schematic of measurement system including four eddy current displacement sensors at a cylinder liner (left) and measured OFT between the first compression ring and the cylinder liner at the location of displacement sensor no. 1, on the thrust side, close to TDC (right) from Tamminen et al. [61]. Printed with permission of Elsevier.

- *Resistance method*: This method is a relatively simple approach that the resistance of an oil film is measured as its thickness changes over the stroke. Early methods, such as Courtney-Pratt et al. [62] and Furuhashi et al. [63], electrically insulated the whole or a part of a piston ring from the rest of the piston and a current passed through the ring to the liner. This approach, however, yielded many individual short circuits occurred between PR/CL, not a smooth change in resistance along the piston stroke. More recently, Saad et al. [64] measured a voltage drop

(resistance) between the piston ring and two electrically insulated electrodes located in the cylinder wall with improved resolution in the range of $<10\ \mu\text{m}$.

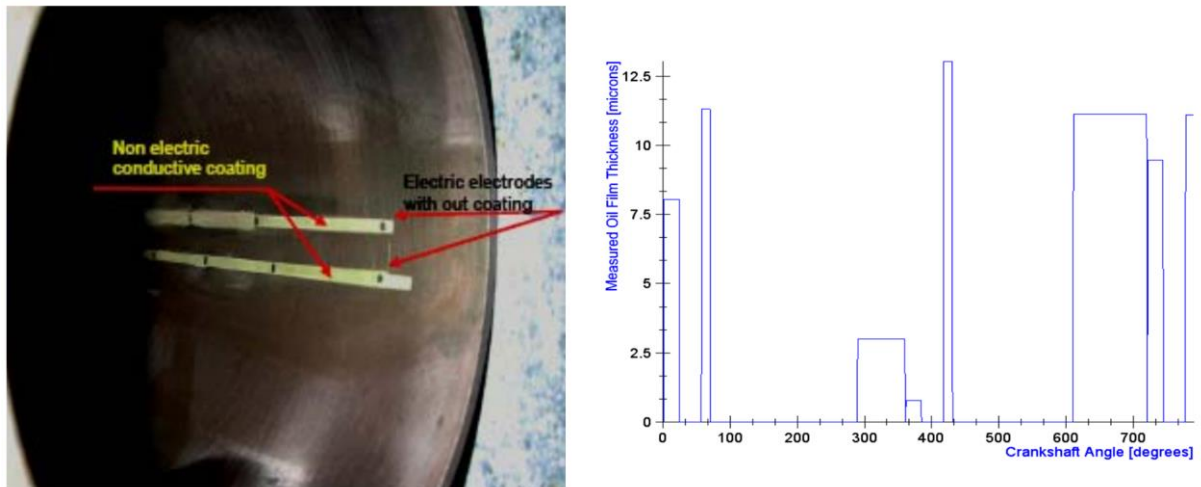


Figure 2.17: Cylinder liner equipped with two electric electrodes (left) and measured OFT between the top piston ring-liner at 1400 rpm engine speed and 80 [ft-lb] torque vs. crankshaft angle (right) from Saad et al. [64]. Printed with permission of SAE International.

It is apparent that these electrical techniques, however, actually measure the separation between two surfaces, not the film thickness itself. Some optical techniques can directly measure the OFT.

Optical techniques

Optical techniques allow the direct, spatially resolved measurement of the OFT, typically by (partially) replacing one of the metal tribo-partners with a transparent window.

- *Interferometry*: This technique relies on the interference of two or more superimposed reflections of the input laser beam. Wakuri et al. [65] measured the OFT between a reciprocating piston ring specimen and a plane glass plate substituting for a cylinder surface by means of a thin film interferometry and reported its good agreement to the theoretical OFT. After that, the authors also measured the squeeze velocity and the separation boundary of the oil film simultaneously using the same method [66]. This technique has been often employed to measure the elastohydrodynamic lubrication (EHL) film in a ball-on-disk apparatus. Luo et al. [67] studied the mechanism of the transition from EHL to thin film lubrication (TFL) by measuring the OFT from the optical interference intensity. Krupka et al. [68] analyzed the influence of surface texturing on EHL lubrication film formation by thin film colorimetric interferometry. While, Vladescu et al. [69] studied the transient changes in film thickness with textured- and non-textured surfaces under sliding, mixed lubrication conditions in a reciprocating tribometer by means of a modified ultrathin film interferometry, which enabled measuring the OFT $< 50\ \text{nm}$.

2. Scientific background

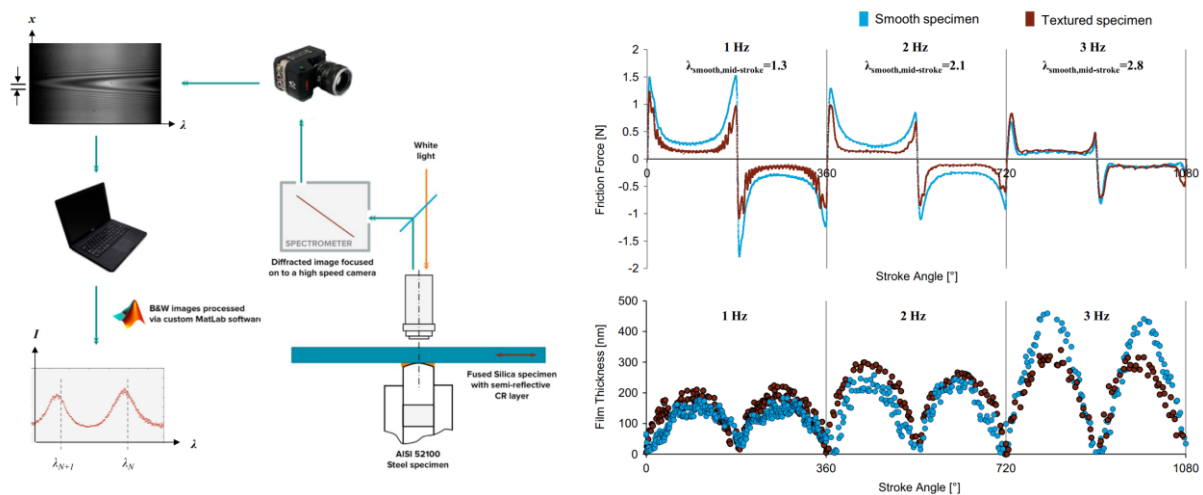


Figure 2.18: Schematic diagram of the interferometry set-up (left) and simultaneous friction force and OFT measurements, comparing textured and non-textured samples and showing the transition from mixed to full film lubrication (test conditions: crank angular velocity: 1, 2 and 3 Hz, normal load: 10 N, oil temperature: 45 °C) from Vladescu et al. [69]. Printed with permission of Elsevier.

- *Laser-induced fluorescence (LIF)*: Other researchers used laser-induced fluorescence to image oil films. Here, a fluorescent dye is added to the oil and illuminated by laser light. The intensity of the mostly red-shifted fluorescence light depends on the local OFT. Thus, direct, two-dimensional, and potentially quantitative visualization of the OFT can be achieved. Some authors employed model test benches or tribometers, which were designed for generating a sliding contact with a thin oil film and simplifying the system for well-controlled parameters, and additionally one of the contacting bodies had to be replaced by a transparent material to get an optical access for using LIF. Poll et al. [70] studied the oil film in sealing contacts by means of a 3D-mapping with LIF. A glass shaft rotated against a radial seal lip, filtered blue spectra from the laser light close to UV illuminated the oil film and its fluorescence was detected by a microscope with a CCD camera. Dearlove et al. [71] employed a reciprocating tribometer representing the friction motion of a single piston ring against a liner segment and simultaneously measured the friction and the OFT by LIF using a He-Cd laser with 441.6 nm excitation wavelength. An optical access was often achieved by quartz windows installed in one of the tribo-partners. Sugimura et al. [72] measured the OFT in a ball-on-disk tribometer, which was a steel-ball/glass-disk configuration. A fluorescence microscope with a filtered excitation light in the range of 330-380 nm from Hg light source detected the oil film. They reported difficulties in this method, such as light interference within thin films and a significant background effect from outlet cavities. With a similar test rig, Myant et al. [73] and Fowell et al. [41] investigated the OFT in a compliant, sliding contact within an optical ball-on-disk tribometer, for which an elastomer specimen (a hemisphere or an O-ring) and a glass disc (or a concave cylindrical glass lens) were employed in an oil bath. The contact was illuminated with 532 nm laser and visualized with a fluorescence microscope.

2. Scientific background

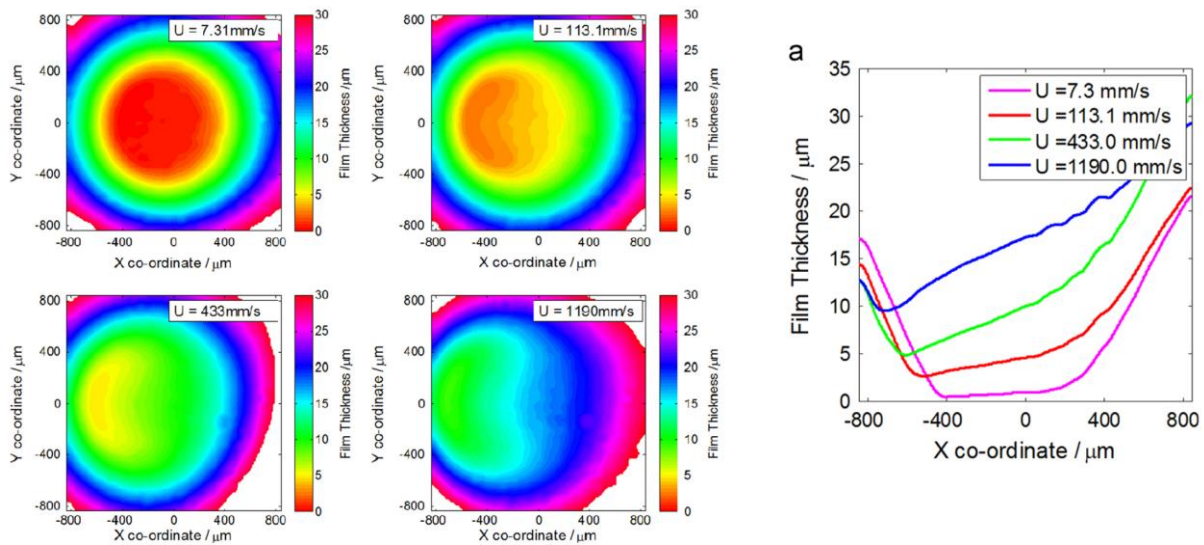


Figure 2.19: Maps of lubricant film thickness via LIF for a PDMS hemisphere on a glass disk (ball-on-disk tribometer) under pure sliding at an applied load of 23.5 mN (left) and plot of lubricant film thickness along the x axis at $y=0$ for a PDMS hemisphere on a flat glass disk under pure sliding for selected entrainment speeds, at an applied load of 23.5 mN (right) from Fowell et al. [41]. Printed with permission of Elsevier.

Vladescu et al. [74] [75] imaged the oil film behavior around the surface texture qualitatively in a reciprocating tribometer simulating a piston ring–cylinder liner pair. Patterned plane fused silica surfaces, which slid against a convex steel pad, enabled an optical access for LIF using a Mercury–Xenon light source.

In our own group, Wigger et al. [76] substituted the conventional metal cylinder liner with a quartz one in a rotational tribometer and measured the OFT in a sliding contact of the glass liner and a metal PRS via LIF method. The oil film could be studied at constant sliding speed with this test rig, whereas reciprocating tribometers or engines generate a wide range of speeds. Laser light of 532 nm excited the oil film, which was doped with a combination of pyromethene 567 and rhodamine 670, and the OFT was quantitatively investigated under varied conditions, such as oil viscosity, sliding speed and normal load.

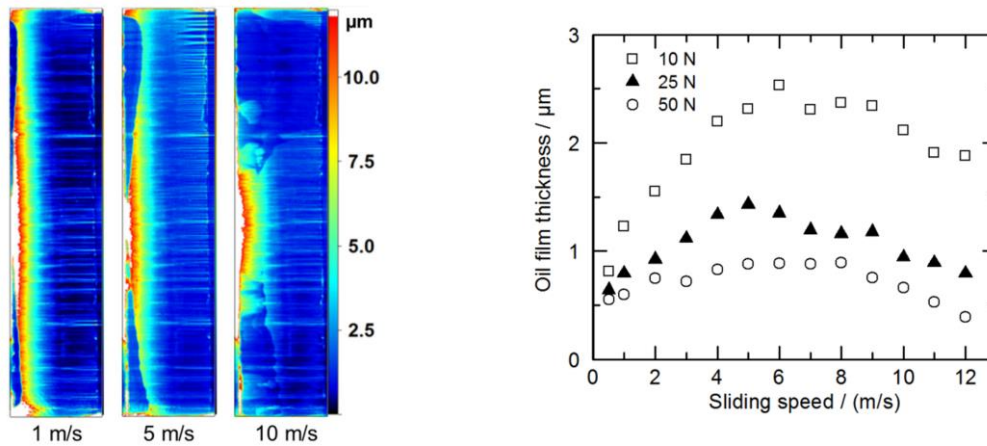


Figure 2.20: Maps of oil film thickness in the RRV tribometer via LIF for a normal force of 25 N and for different sliding speeds (left). Measured OFT averaged over an area of $0.08 \times 6.4 \text{ mm}^2$ in the lateral center of the piston ring segment for a variation of sliding speed and load (right) from Wigger [18]. Printed with permission of the author.

Obert et al. [77] used the same light source and dye combination as those of Wigger. They imaged the OFT under starved lubrication conditions within a quartz liner segment and a metal PRS contact using a reciprocating tribometer. Full-field as well as line-shaped views (latter one employed a sheet-of-light method to avoid a scattered light effect) of the oil film were achieved and the scuffing initiation mechanism in the PR/CL contact was clarified.

For the OFT measurement in a research engine, Greene [78] first implemented the LIF technique. He replaced the cylinder with a glass one within a simplified single-cylinder research engine. The oil film in the PR/CL was visualized using two methods: first one was a UV-light LIF method using a natural fluorescence from the mineral oil and the second one was a total reflection based scattered light method that used a xenon flash tube as a light source and illuminated the glass cylinder directly from its head to yield the total reflection of the light inside the material. Ting [79] also equipped a single-cylinder engine with a transparent sleeve and measured the oil film behavior via LIF without calibration. The light source was a He-Cd laser with an excitation of 442 nm wavelength and the oil was non-colored. Hout et al. [80] continued Ting's study. They used an optical engine with a quartz window on the cylinder wall, added Coumarin 523 as a dye into the oil, which was illuminated by the same laser as that of Ting, and developed calibration methods to present the OFT quantitatively. Since then, more studies have adopted the LIF method in an engine to investigate oil films in the piston-cylinder assembly. Some authors inserted one or more fiber optic lines into the cylinder liner that enabled point measurements of the OFT [2] [81] [82] [83]. However, this approach allowed only the OFT data of one or few points at a time. Thus, the others embedded windows (quartz or sapphire) in the cylinder or replaced an entire cylinder with a glass one to visualize the OFT in two-dimension in an engine. Inagaki et al. [84] developed a two-dimensional LIF diagnostic system, which consists of a Xe-flash lamp and a CCD camera. This was installed in an optical

single cylinder diesel engine, where two types of cylinder liners were prepared – a whole transparent glass liner for the motoring test and a cast iron liner embedded with a pair of slit sapphire windows for the firing test. In addition, the output of the Coumarin-doped oil film filled between a cylindrical block and a flat glass enabled an OFT calibration with a sufficient OFT resolution of sub-micron order. Thirouard et al. [85] [86] mounted a honed quartz window in the cylinder. They doped the oil with rhodamine 590 and used 532 nm excitation light from an Nd:YAG laser. With the resulted images, several mechanisms of oil transport, e.g., on/around the piston second land, were studied. Subsequently, in the same group, possible dye candidates were further studied and a combination of pyrromethene 567 and rhodamine 640 was chosen to visualize more detailed oil transport and its exchange in the same research engine [37] [87] [88] [89]. Kato [40] combined the LIF method with a particle image velocimetry (PIV) to measure the OFT and its velocity distributions simultaneously in a test engine. The test engine is a two-cylinder model engine with a motored operation, where one entire cylinder was replaced by a sapphire one. A dye of rhodamine B is added to the oil and an Nd:YAG laser with 532 nm illuminated this.

In our own group, Wigger [18] imaged qualitative oil- or fuel film distributions respectively on the cylinder wall through a sapphire window in a single-cylinder direct-injection engine. The window allowed a view between the crankcase and the combustion chamber. For the oil measurement, laser light of 532 nm was used and the oil is doped with a combination of pyrromethene 567 and rhodamine 640. As a follow-up, Müller et al. [42] [90] simultaneously visualized the oil film and impinged liquid fuel on the cylinder wall in the same engine as Wigger. Regarding of the oil film, they doped that with a single pyrromethene 567 and analyzed quantitative OFT distributions as well as the piston secondary motion. Schöler [91] visualized the oil transport phenomena in the chamfer beneath the oil control ring of a piston in the engine and compared the results to the three-dimensional volume-of-fluid CFD simulations.

These previous works imaged the oil film in the PR/CL contact or its generic equivalent, but the contact surface was always polished or honed. The oil film on the conventional liners from the production line, recently often with a porosity, was not considered. Because the influence of the surface structure was not the focus of those investigations, the imaging magnification was relatively low, and the detailed microscopic oil film behavior could not be resolved.

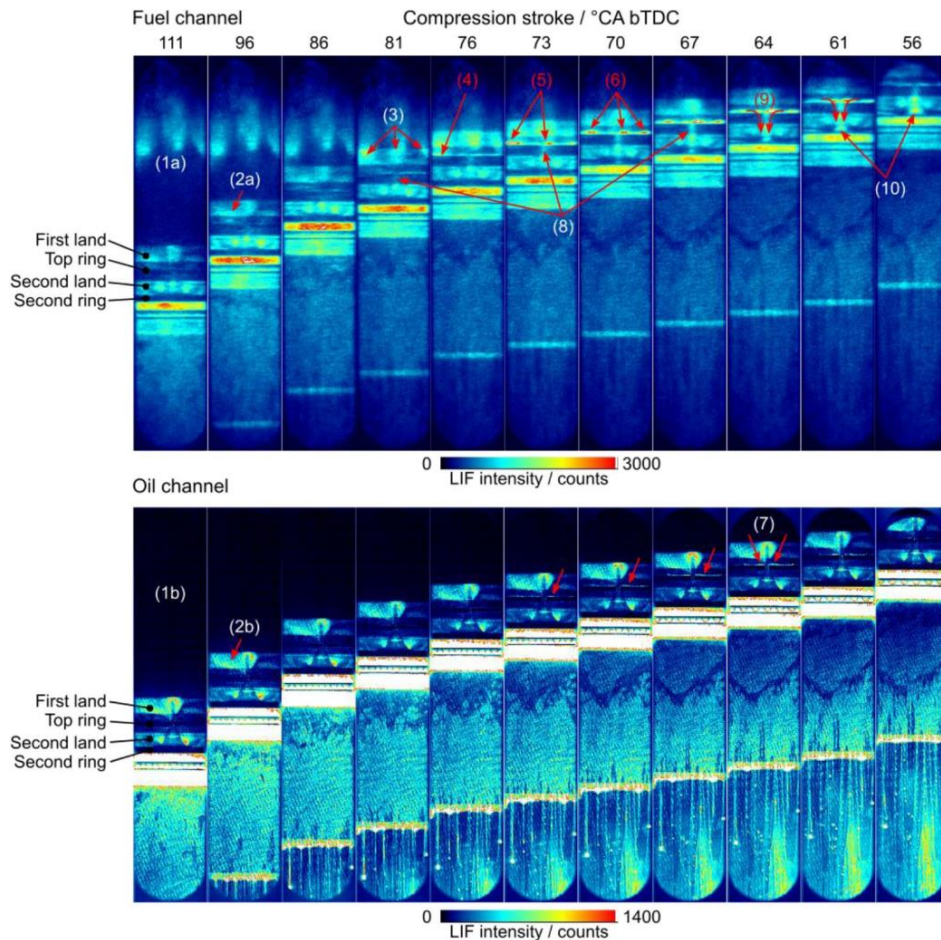


Figure 2.21: LIF images from the compression stroke of a single cycle (first row: fuel channel, second row: oil channel) as showing a fuel transport from the cylinder wall onto the piston lands due to ring scraping from Müller [90]. Printed with permission of SAE International.

2.2.2 Surface texturing

Surface texturing has received interest already since mid-1960s as an effective technique for reducing friction and wear with the study of Hamilton et al. [92]. They argued that micro-irregularities on the surfaces of rotary-shaft seals enabled the contact to generate hydrodynamic pressure and a load carrying capacity. The theoretical results agreed with experimental ones, which showed local cavitation at the divergent region that was responsible for the load support. In 1996, Etsion's group [93] found in one of their first papers on surface texturing that hemispherical dimples on one of the mating sealing surfaces increased load carrying capacity in contact with modelling results and an optimization of the texture size and density was critical. Their subsequent tests also presented that a textured seal could have a threefold increased lifetime than a non-textured one. After these promising results, the effect of the surface texture has been more actively studied due to its broad-range potential in tribological applications. Its main advantageous functions have been reported as following: (1) Textures act as micro-hydrodynamic bearings and generate an additional hydrodynamic

pressure, which results in an increased load carrying capacity and a reduced friction. Some authors argued that local cavitation, which occurs at the divergent part of a texture with a sub-ambient pressure, might be responsible for the phenomenon [94] [95] [96] [97]. (2) Moreover, this sub-ambient pressure in the textures might yield an *inlet suction* effect, which can suck more lubricant into the contact zone than would be without the textures [98] [99]. The effect leads to increase in the maximum pressure and the load carrying capacity. (3) Especially under the boundary and mixed lubrication, the textures reduce the real asperity contact area and thus lower the overall friction [100] [101]. (4) They also can serve as micro-traps collecting the wear debris and minimizing third-body abrasion [102] [103] [104]. (5) In addition, the textures can feed lubricant into the cavitated outlet region and prevent oil starvation especially at a reversal in the reciprocating sliding contact [74] [75]. As a result, the textured surface can lead to a greater OFT, reduce the frictional force, yield an earlier transition between the mixed- and the hydrodynamic lubrication regime and extend the useful lifetime of the surface [99] [105] [106].

With non-connected textures, some phenomena contributing to the increased hydrodynamic pressure and OFT occur often more effectively than with interconnected ones especially under the boundary or mixed lubrication. This might be due to their closed feature, which could retain the oil inside better during the loaded, sliding contact, while the oil could be easily displaced along the open grooves in the case of the interconnected textures [107] [108]. Numerous attempts have been made within the non-connected textures to optimize the texture's parameters, e.g., the pocket shape, by employing the laser surface texturing technique. The most commonly studied shapes are circular, elliptical, rectangular, triangular, chevron and short groove. Among them, the chevron pointing along the sliding direction [94] [109] and short grooves perpendicular on the sliding direction [74] showed the highest tribological effectiveness, yielding a higher hydrodynamic pressure.

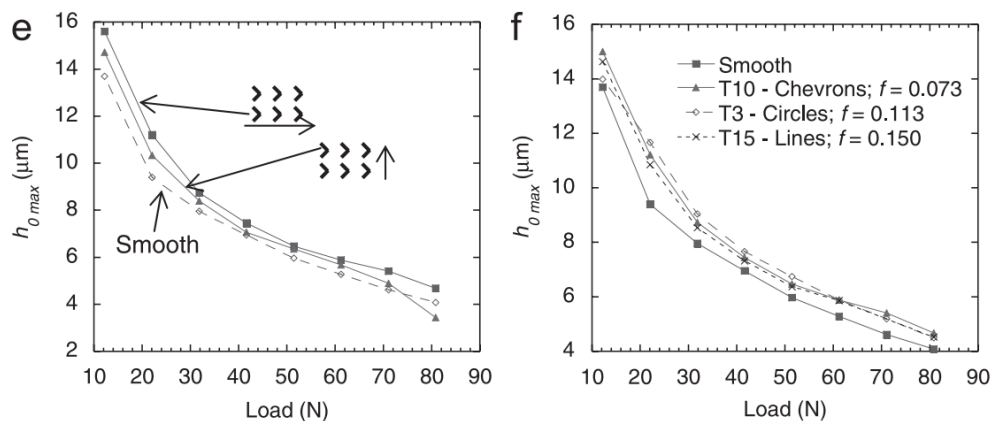


Figure 2.22: Effect on $h_{0\max}$ (OFT) of geometric characteristics of the patterns: e) effect of relative orientation for chevron pockets (left) and (f) effect of different texture shapes (right) from Costa et al. [94]. Printed with permission of Elsevier.

2. Scientific background

Furthermore, the textured pocket's size, depth, aspect ratio (depth over diameter ratio) and area coverage density have been often investigated as design parameters. For example, as far as the aspect ratio is concerned, the optimum ratio of around 0.1 has been repeatedly reported [97] [106] [110] [111]. For the other parameters, it was found that there often exist optimum values under different operating conditions for the best tribological performance respectively and thus they should be carefully chosen [94] [112] [113] [114].

One of the most common, successful applications of the surface texturing is at the surface of the cylinder liners in IC engines, such as micro grooves from honing or, more recently, a fine porosity. Plateau-honed liners are still frequently used in today's combustion engines and lots of analytical studies of that have been conducted. Some authors focused on the effect of the surface roughness from the honing structure. They argued that the reduction of the roughness could offer the lowest friction and oil consumption, although it might yield more vertical flaws (scuffing) on the liner presumably due to its lowered oil holding capability [115] [116] [117] [118] [119] [120]. Others studied the honing groove's cross-hatch angle and reported that the OFT between PR/CL increased as well as the friction decreased with decreasing cross-hatch angle [121] [122] [123] [124] [125].

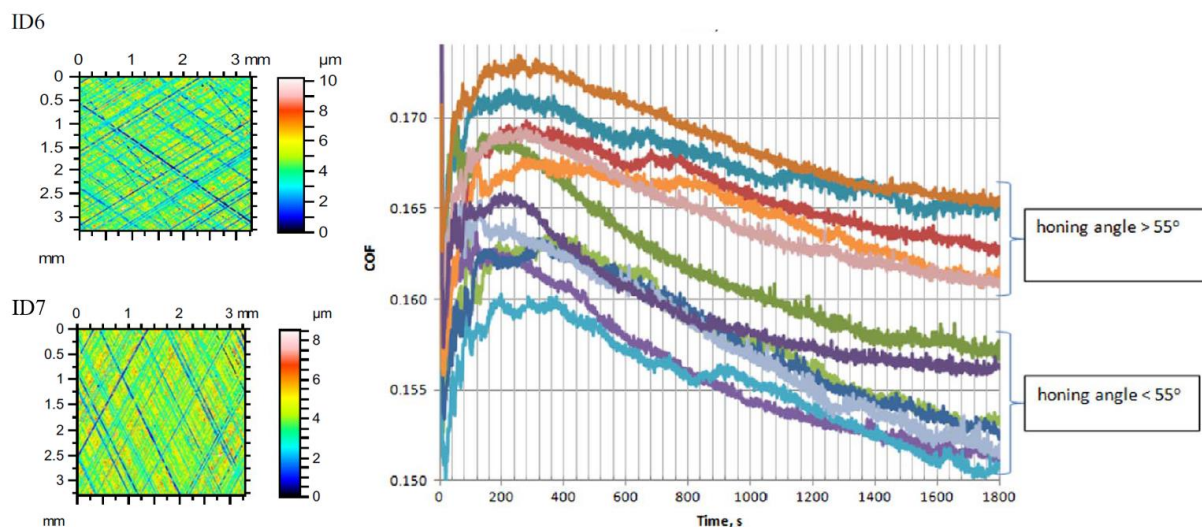


Figure 2.23: Contour plots of honed cylinder liner texture (honing angle of ID6= 125 °, ID7= 28 °) (left) and coefficient of friction versus time for textures with honing angle different than 55 °(right) from Grabon et al. [125]. Printed with permission of Elsevier.

Apart from the honing, the effect of other texture features on the engine performance was also studied. The tribology group at Imperial College focused on grouped, non-connected surface pockets. They employed different micro-texture shapes (transverse, parallel and angular grooves and chevrons) on the liner specimen and the frictional behavior in PR/CL reciprocating motion was compared to that of a non-textured specimen. By means of fluorescence microscopy, the oil film around the pockets was qualitatively visualized at high magnification.

Friction forces with different textures were also measured and these experimental results were compared to the results of numerical modelling. They found that each pocket transferred oil from the inlet to the outlet, which resulted in a more even lubrication distribution, and the presence of the pocket was especially effective in the reversal zone, where boundary and mixed lubrication regime was dominant [74] [126] [127].

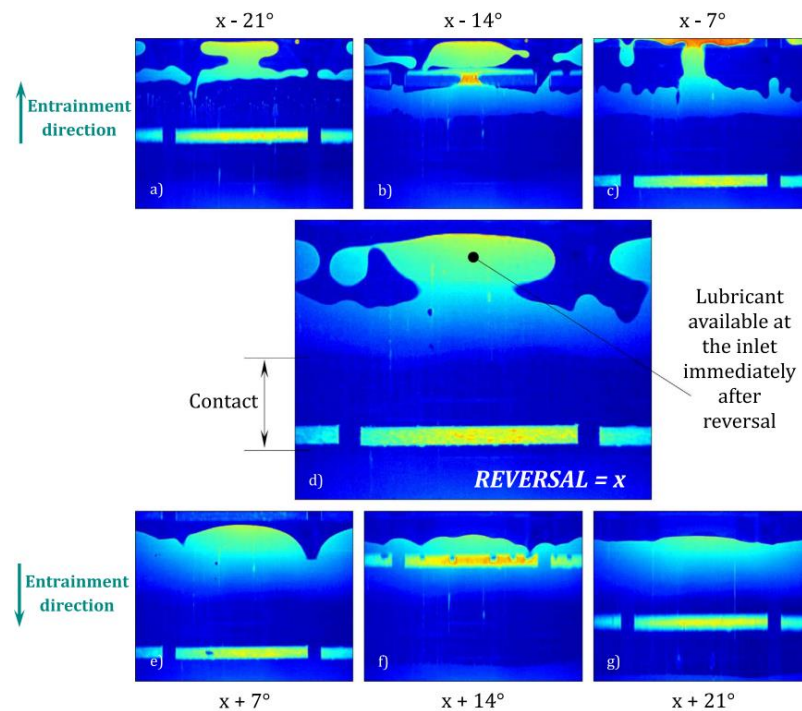


Figure 2.24: Sequence of LIF images of groves pockets transversal to the direction of sliding passing through contact at a step of 7 degrees of crankshaft revolution. Each pocket transferred oil from the inlet to the outlet and it shows the effectiveness of the pockets in the reversal zone. From Vladescu et al. (tribology group at Imperial College) [126]. Printed with permission of Elsevier.

Yin et al. [75] focused on the effect of micro dimples (circular textures) distributed over the entire cylinder liner using a mixed lubrication model and asperity contacts equation. In most regions of the strokes, a hydrodynamic lubrication was formed with the textures, only except the region near the dead points. They also optimized the dimple parameters to obtain a better lubrication effect. Checo et al. [128] implemented numerical simulations of PR/CL, where the liner exhibited a periodic texture, and argued that the piston ring profile determined whether the surface texturing would be advantageous or not. Koszela et al. [129] studied the liner not only with honing but also with circular dimples and a combination of them showed better engine performance, i.e., higher maximum power and torque, than the liner only with honing.

Most of the previous experimental works with the textured surface were focused on grouped pockets. Hence, the detailed oil-film behavior in and around an individual pocket has been rarely investigated. In addition, the limitation of those studies so far is that the oil film around the surface texture was only qualitatively imaged and thus the amount of oil transferred by the

textured pocket or that remaining in the pocket could not be measured. This research gap is filled in this work in chapter 4.

2.2.3 Fluorescence-based temperature imaging in liquid films

Understanding of the thermal behavior of the oil film in the PR/CL contact is crucial in an engine, since it contributes to the thermo-mechanical failure like scuffing and thermal fatigue. More generally, to study the temperature distribution in a fluid contactless, several techniques based on the LIF of the added dye have been developed. They principally rely on the temperature-dependence of the dye emission that originates from the temperature-sensitive quantum yield and/or absorption cross section at the excitation wavelength. A dye with high resistance to the photobleaching is preferred.

The first technique is a single-color/single-dye (1c/1d) technique. It enables a temperature mapping with a single dye and a single spectral band for the detection. The local temperature is measured using a ratio between the measured intensity and the reference intensity of known temperature. Rhodamine B or kition red has been suggested as one of the best dyes for this technique [130] [131] [132].

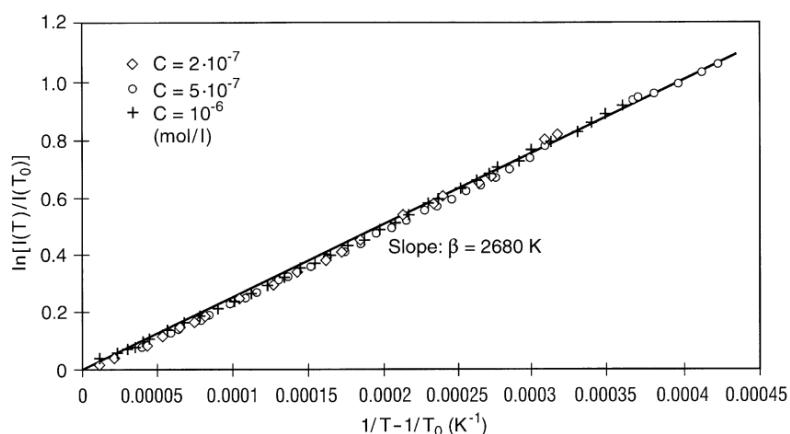


Figure 2.25: Temperature dependence of the fluorescence intensity with different rhodamine B concentration of $\diamond C=2.10^{-7}$; $\circ C=5.10^{-7}$; $+ C=10^{-6}$ (mol/l) from Lemoine et al. [132]. Printed with permission of Springer Nature BV.

However, this technique has some constraints, such as maintaining the dye concentration, probe volume and incident laser intensity constantly during the experiment. If a pulsed laser is used, the fluctuation of the shot-to-shot pulse energy should be also monitored. In addition, the spatial inhomogeneity of the energy distribution in the laser sheet should be corrected [133]. From those reasons, it has been reported that this technique is inappropriate to measure the temperature in sprays and flows with bubbles [134].

A second approach is a two-color/single-dye (2c/1d) technique, which employs the different temperature dependence of the LIF intensity from a single dye in two spectral bands. A

2. Scientific background

ratiometric scheme of the intensities can eliminate the dependence on such as the dye concentration, incident laser intensity, probe volume dimensions and Beer's absorption on the laser beam path [135]. This method is especially suitable to measure the temperature when the dye concentration is not uniform, such as a liquid evaporation or a vapor condensation where the mass transfers occur. The most used dye for this method is rhodamine B and coumarin 152 [136]. This technique has been applied to determine the temperature of evaporating and combusting droplets [135] [137] [138] and single-phase flows [139].

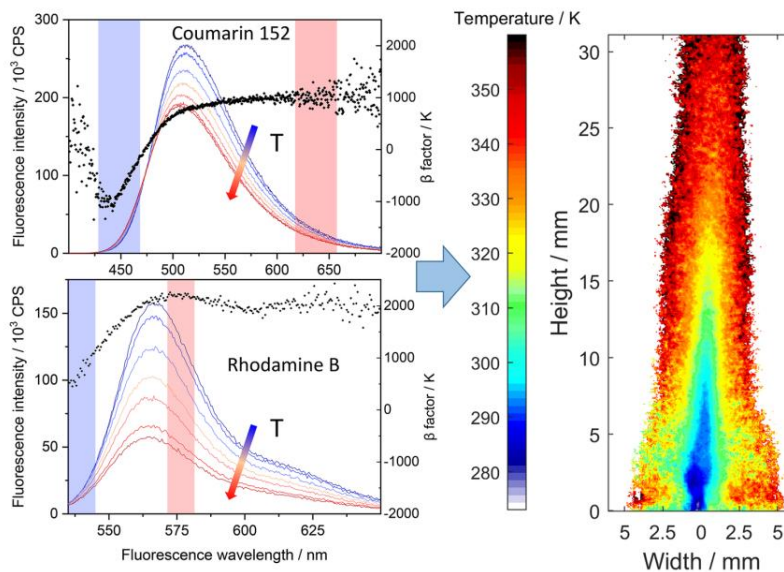


Figure 2.26: Temperature-dependent fluorescence spectra of coumarin 152 and rhodamine B in ethanol excited at 355 nm and 532 nm for each. Black dots: β factor, colored areas: best compromise for blue and red color-band for thermometry (left). Temperature map of the SpraySyn flame operated with ethanol seeded with coumarin 152 (right). Graphic abstract from Prenting et al. [136]. Printed with permission of Springer Nature BV.

The third technique is referred to as two-color/two-dye (2c/2d) method. The fluorescence intensities from a mixture of two different dyes are separately detected in two spectral bands and the intensity ratio between these two bands is used to determine the temperature. To be selected as a pair of dyes, their fluorescence intensities can show an opposite temperature dependence, which yields relatively high temperature sensitivity of the intensity ratio, such as fluorescein 27/rhodamine B or fluorescein 27/kiton red 620 [140]. On the other hand, one temperature-sensitive dye and another temperature-insensitive dye can be paired and some studies suggested pairs of rhodamine B/rhodamine 110 [141] [142] [143], fluorescein disodium/sulforhodamine 640 [134] [144] and rhodamine 6G/pyridine 1 or rhodamine 6G/DCM [145].

2. Scientific background

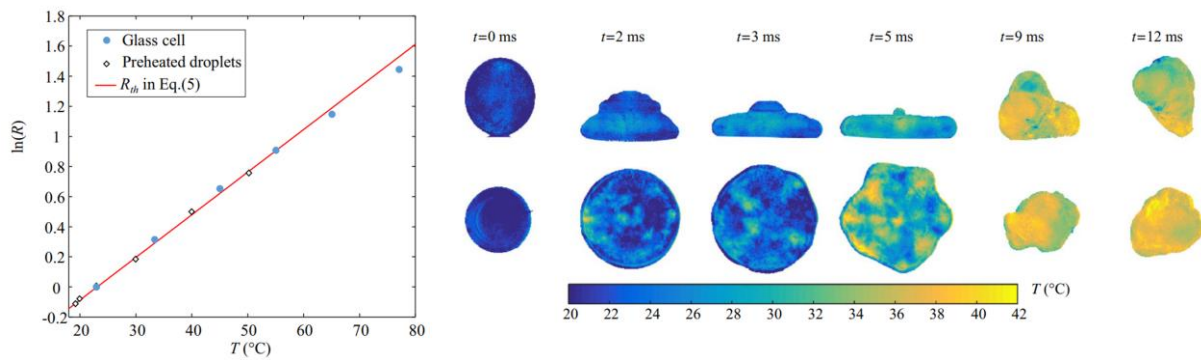


Figure 2.27: Evolution of the fluorescence ratio R (between fluorescein disodium and sulforhodamine 640) as a function of the temperature. R is normalized to be equal to 1 at 23 °C ($C_{\text{SR640}} = 7 \cdot 10^{-7}$ M and $C_{\text{FL}} = 2 \cdot 10^{-4}$ M) (left). Side and bottom views of the temperature field within an impacting droplet at $We = 10.2$ (right) from Chaze et al. [144]. Printed with permission of Springer Nature BV.

The often-used rhodamine family is not considered as a dye candidate in this work in chapter 5, since it has a low oil solubility. Also, the single-dye techniques are excluded due to their relatively low temperature sensitivity. The selected dye combination in this work is Lumilux CD 345/pyromethene 597. Unlike the mostly reported fluid film thermography using a laser, this work employs a LED as a light source. This is because that the selected dye combination should be excited at a specific wavelength, which is rarely available from lasers. In addition, the relatively low energy of the LED prevents the front objective of the long-distance microscope from being damaged in a coaxial illumination through it.

3 Oil film thickness imaging on the metal cylinder liner

This chapter reports on the visualization of the oil film behavior in the PR/CL in a tribometer using laser-induced fluorescence (LIF) with an as-manufactured cylinder liner. This enabled 2D imaging of the oil film with different liner surface structures as well as the quantitative measurement of the minimum oil film thickness for specific parameter sets (e.g. sliding speed and load).

Most of this chapter was presented at the 46th Leeds-Lyon Symposium on Tribology (2019) in Lyon, France, as “High-resolution LIF-imaging of the oil film thickness in the piston-ring / cylinder-liner contact in an optical tribometer”, at the GfT (Gesellschaft für Tribologie e.V.) Tribologie-Fachtagung (2018) in Göttingen, Germany, as “High-resolution imaging of the oil film in an advanced piston-ring model tribometer by laser-induced fluorescence” and was published as “Cheong J, Wigger S, Füßler H-J, Kaiser S. High-resolution LIF-Imaging of the oil film thickness in the piston-ring/cylinder-liner contact in an optical tribometer. *Tribol Int* 2020; 147: 106230”. I designed the modified experimental apparatus, performed the LIF experiments, post-processed, visualized and evaluated the results of the LIF data, wrote the original draft and reviewed it.

3.1 Methods

3.1.1 Initial setup of the RRV-Tribometer

Mechanical configuration

Initially, the RRV (from German, “Rotations-Reib-Verschleiß”, i.e., rotation-friction-wear) tribometer shown in Figure 3.1 was devised as a well-controlled model experiment for reproducing the sliding contact in the PR/CL of an engine and for measuring the friction coefficient at specific parameter.

3. Oil film thickness imaging on the metal cylinder liner

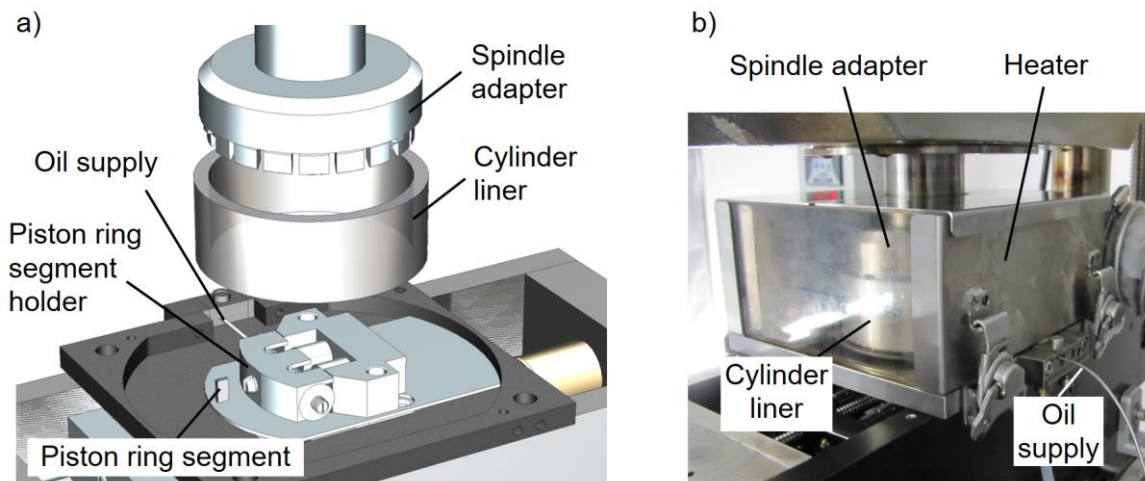


Figure 3.1: a) Initial RRV tribometer setup (CAD exploded view). b) Photo of the assembled initial RRV tribometer with a heater.

It converts the reciprocating motion of the piston in an engine into the steady rotating motion of a cylinder liner against a static PRS (see Figure 3.2). This enables investigating the oil film at constant sliding speed, whereas reciprocating tribometers or research engines produce a wide range of sliding speeds from zero in the reversal points to a mid-stroke maximum.

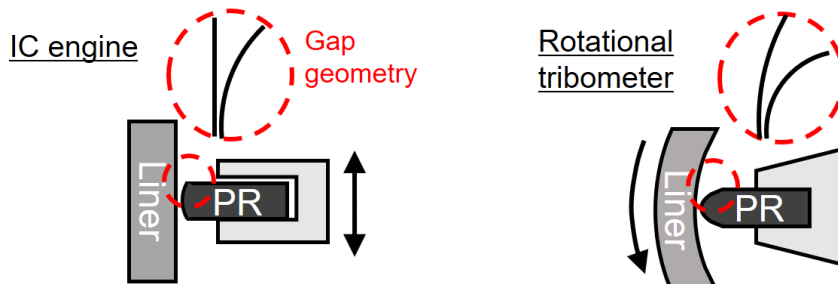


Figure 3.2: Transfer of the piston ring's reciprocating motion in an IC engine to the liner's rotating motion in a rotational tribometer, maintaining the gap geometry and the line contact.

For comparability of these two contact situations, the liner and piston ring are suitably modified. A cylinder liner from the engine is shortened to a height of 35 mm and clamped to a spindle adapter in rotating motion as shown in Figure 3.1. The top piston ring is cut into a piston ring segment with a lateral radius of 20 mm to maintain the same geometric conformity with the liner radius of 41.5 mm as that of a typical top piston ring in an IC engine, as shown in Figure 3.2 and Figure 3.3. The piston ring segment is fastened by the piston ring segment holder. The PRS holder pivots around a point at the center of the PRS height, and the normal force F_N is applied here. This compensates any slight eccentricity of the liner surface and allows steady line contact during the liner's rotation. Lubricant oil is constantly supplied with a HPLC pump via a glass capillary and sprayed onto the inside of the liner with a constant amount of 0.1 mm^3 per rotation. With this initial setup, a hot-air heater heats the air as shown in Figure 3.1b; and

3. Oil film thickness imaging on the metal cylinder liner

it is measured and controlled by the K-type thermocouple inserted into the hole of the PRS, shown in Figure 3.3a. Here, the measurement uncertainty of the temperature caused by the thermocouple is $\pm 0.8\%$.

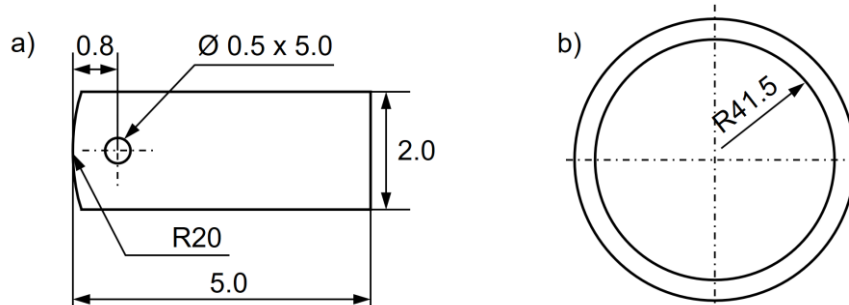


Figure 3.3: a) Geometrical dimension of the metal piston ring segment (top view). b) Geometrical dimension of the metal cylinder liner (top view)

Figure 3.4 shows the position of each normal- and friction force sensor inside of the tribometer after disassembly. Two normal force sensors from the company *disynet* lie inside of the bottom housing. They are connected to each other by a crossbar and the bar is fixed to the piston ring segment holder to perceive the normal force from the piston ring segment. Each sensor has a measurement range of 60 N, which corresponds to the total maximum of 120 N. Each output voltage-signal from each sensor lies in the range of 0 to 10 V and two signals show the same sign and direction. On the other hand, two friction force sensors measure the shear force and they are positioned directly behind the piston ring segment holder. (PRS holder is detached in Figure 3.4 and not shown.) The sensors are connected to each other by a cylindrical connector, where the friction force is applied. Each sensor measures the force in the range of 20 N and it allows the total maximum detectable force of 40 N. One of the output voltage-signals shows a positive sign and the other shows a negative, since the applied shear force compresses one sensor, but simultaneously stretches the other sensor. The signals are in the range of ± 0 to 10 V.

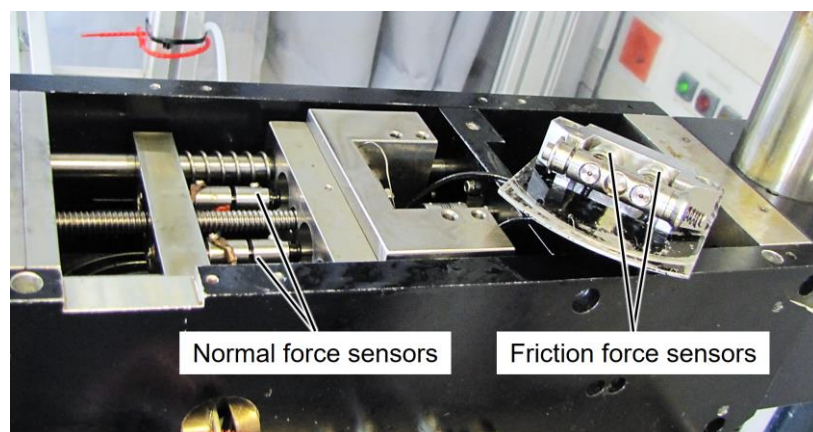


Figure 3.4: Position of the normal- and friction force sensors inside of the tribometer after disassembly.

Operating conditions

With this initial RRV tribometer, basically, the measurements of the friction coefficient and the Stribeck curve have been carried out under varied operating conditions, such as different normal loads, sliding speeds, temperatures. The available operating parameters in RRV tribometer are based on the Mercedes-Benz M270/274 engine.

Figure 3.5a and b show the trace of the combustion chamber pressure and the sliding speed with the crank angle in the engine, respectively. At 5000 min^{-1} , the maximum pressure is 93 bar, which corresponds to about 100 N under the RRV tribometer condition and thus, the normal load in the tribometer can be set up to 100 N [18]. The maximum sliding speed in the engine is 25 m/s at 5000 min^{-1} , however it is reached only in a small area of the piston stroke. Hence, the maximum sliding speed in the tribometer is limited to 10 m/s.

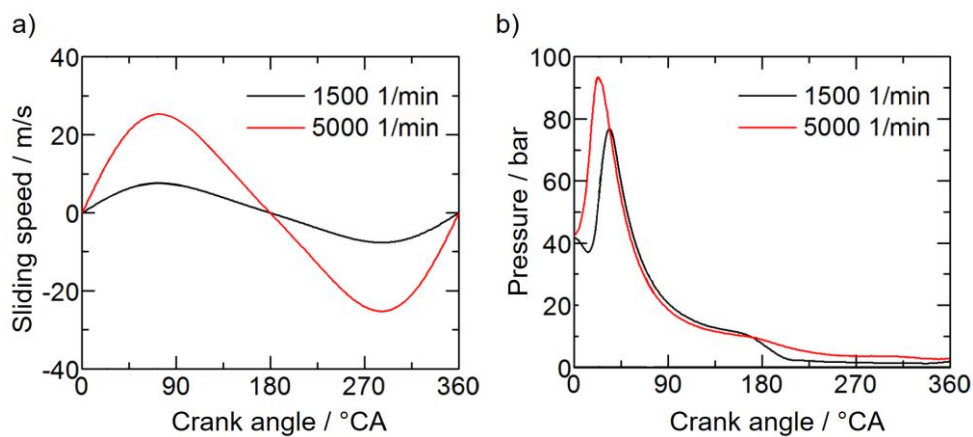


Figure 3.5: a) Trace of the sliding speed and b) the combustion chamber pressure in the Mercedes-Benz M270/M274 engine with the crank angle at the two rotational speeds [18]. Printed with permission of the author.

Figure 3.6 presents a typical progression of different operating parameters in the RRV tribometer during the test for the friction coefficient and Stribeck curve measurement.

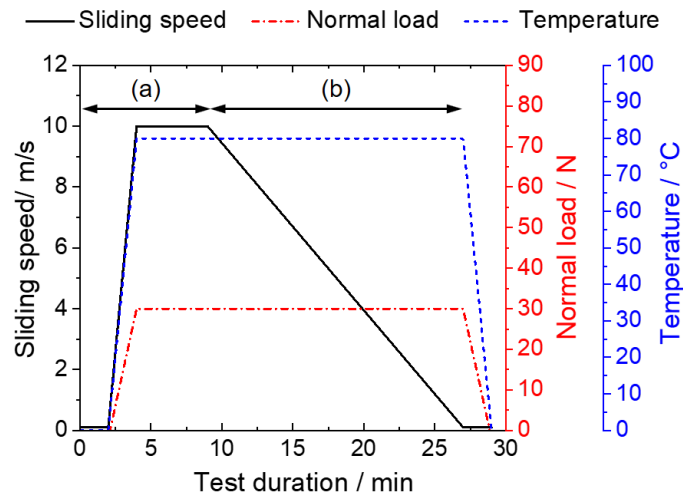


Figure 3.6: Typical progression of the operating parameters in RRV tribometer for measuring friction coefficient and Stribeck curve. (a) and (b) indicate the preparation time and the test time, respectively.

In first 2 min, the liner rotates slowly without given normal load to be sufficiently lubricated by the oil supply. After that, the sliding speed increases with a gradient of 5 m/s per minute up to the maximum speed, e.g., 10 m/s. At the same time, the normal load and temperature increases as well up to its given condition (e.g., 30 N and 80 °C in Figure 3.6). For the next 5 minutes, the maximum sliding speed is maintained for the system stabilization. Until here is the preparation time for the measurement. After that in the region (b), the speed decreases with the gradient of -0.55 m/s per minute until it reaches the sliding speed of 0.1 m/s and the Stribeck curve is plotted with the result in this region. At the end, the temperature of 0 °C (or room temperature) and the normal load of -2 N (without contact) are given with the lowest sliding speed of 0.1 m/s in order to reset the system. All of the Stribeck curves in this work are measured with this procedure. This can be repeated successively if necessary and the given operating parameters can be modified. For an optical measurement at each specific sliding speed, the procedure (a) is solely performed and the LIF image is recorded while the sliding speed is constantly maintained.

Modified configuration and material arrangement

Based on the initial configuration of the RRV tribometer shown in Figure 3.1, the material arrangement is modified in this work. In chapter 3.1.2, the metal PRS is replaced with a sapphire one to investigate oil films on the production metal liner surfaces. For that, a periscope optic system is newly designed and some parts of the initial configuration are altered. Inversely in chapter 4 and 5, the conventional metal liner is replaced with a quartz one, while the metal PRS is employed again, to get an access of a microscope for a higher magnification. This material arrangement was firstly used by Wigger [18] in our group. Figure 3.7 shows the material inversion in the RRV-Tribometer used in the next chapters.

3. Oil film thickness imaging on the metal cylinder liner

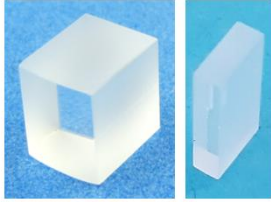


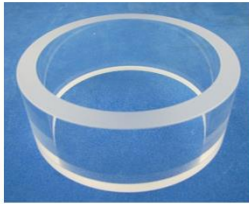
	Material arrangement in chapter 3	Material arrangement in chapter 4 and 5
Piston ring segment	Glass 	Metal 
Cylinder liner	Metal 	Glass 

Figure 3.7: Material inversion in RRV-Tribometer.

3.1.2 RRV-Tribometer with periscope optic

As discussed above, in our group, Wigger [18] substituted the conventional metal liner with a quartz one to visualize quantitative OFTs via LIF within the initial configuration of the RRV tribometer and studied the lubrication behavior under varied conditions. However, this restricted the liner surface material to quartz or potentially sapphire. To allow investigating oil films on the production metal liner surfaces, this material arrangement is now inverted as shown in Figure 3.7 and Figure 3.8a, such that optical access to the contact area is achieved through a sapphire PRS via a periscope-like mirror configuration. For that, some parts of the tribometer, e.g., the sapphire PRS and its holder, were newly designed and replaced (Figure 3.8a).

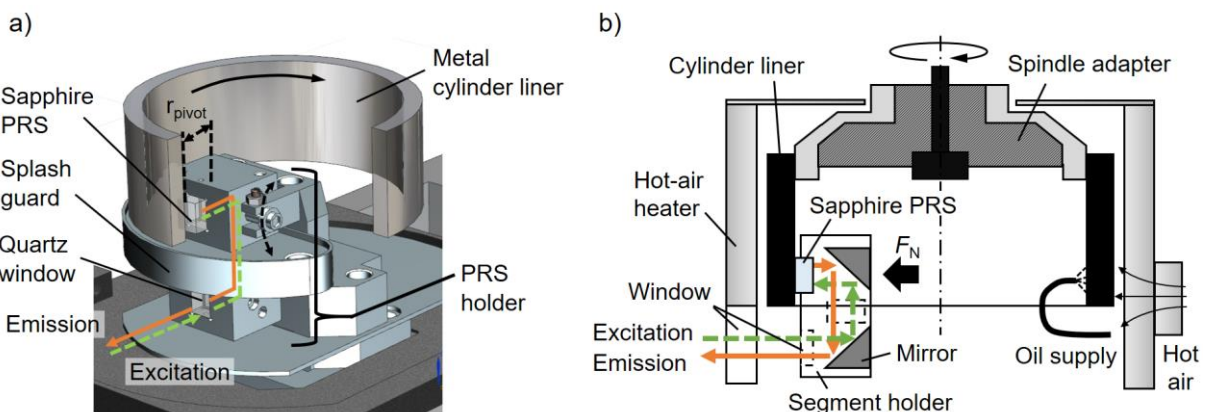


Figure 3.8: a) New arrangement that can employ conventional cylinder liners with a sapphire PRS and a periscope optic arrangement. b) Schematic representation of a cut section, also showing spindle, heater, and oil supply.

A wider sapphire PRS is mounted and sealed with a heat-resistant silicon adhesive in a PRS holder that includes two reflecting mirrors arranged as a periscope (Figure 3.8b). As mentioned in chapter 3.1.1, the PRS holder pivots also around a point at the center of the PRS height, the normal force F_N is applied here and this pivot point lies 14.5 mm (r_{pivot} in Figure 3.8a) behind the PR/CL contact line. Oil is sprayed onto the inside of the liner. To avoid fouling of the optical parts by the oil, a splash guard is placed under the liner as shown in Figure 3.8a. In the lower part of the PRS holder, under the guard, a quartz window is inserted to prevent oil from penetrating the housing. Like the initial RRV tribometer setup, the heater box covers the entire setup shown in Figure 3.8 and heated temperature-controlled air is blown in near the PRS. A thermocouple is not inserted in the hole of the PRS, since it may obstruct the view of the oil film, but the temperature is measured by the thermocouple hung near the PRS. The measured temperature difference between inside of the PRS hole and near the PRS was about 0.5 °C, which is within the given measurement tolerance of the K-type thermocouple.

The optically accessible configuration of the RRV with the sapphire PRS is not equipped with sensors for the friction force. To compare the OFT with the corresponding friction coefficient, separate experiments were performed with the RRV in the configuration shown in Figure 3.1 without an optical access. Here, a sapphire PRS with a width of 2 mm was used to fit into the initial PRS holder and a conventional metal liner was employed to keep the material pair and arrangement the same as in the optical experiments.

3.1.3 Contact surfaces

In order to examine the surface topography, a confocal microscope (μ Surf Custom and μ Surf Cylinder, NanoFocus AG) was used. Using a 20x objective (800XS) in this work, the lateral resolution is given as 0.95 μ m.

In chapter 3, the measurements were carried out with two different types of cylinder liners. First, a gray cast-iron liner (GG - in German: Grauguss) with a plateau-honed surface was used. The honing is rather fine (“A1” according to the Mercedes-Benz internal standard MBN 37800-1, summarized in [146]). The second liner was equipped with an arc-wire sprayed surface (LDS), using Nanoslide® technology, in which arc spraying melts iron/carbon wires and sprays them finely onto the cylinder surfaces of the aluminum cylinder block. As a result, the surface is honed with a fine porosity in the otherwise mirror-like finish. This results in reduced friction losses compared to the gray cast-iron liner as well as high wear resistance and exhaust-gas emission reductions [25]. Figure 3.9 shows the surface topographies of both liners, and the areal surface texture parameters according to ISO 25178 [147] measured by confocal microscopy. Here, S_q is a root mean square height of the surface according to that standard [147], while additionally in this work S_q^* was evaluated in a smaller region (1.5 \times 1.5 mm), excluding deep pores on the LDS liner.

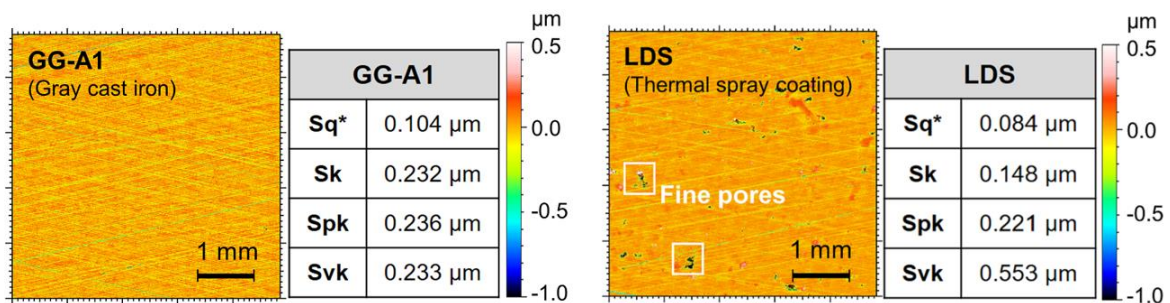


Figure 3.9: Surface topographies and areal texture parameters of the gray cast iron (GG) liner and the LDS (Mercedes-Benz Nanoslide® technology) liner measured by confocal microscopy. S_q^* values were individually evaluated in a smaller region (1.5 \times 1.5 mm) excluding pores in the LDS liner.

The sapphire PRS (Figure 3.10a) has a radius of 20 mm on the contacting side and a wider width of 8 mm for larger optical access and higher mechanical strength compared to the typical 2 mm steel PRS used in the previous arrangement (see Figure 3.3 and Figure 3.7). In Figure 3.10, the contact line shape and roughness are shown, again characterized by confocal microscopy. From the finishing process, the surface is slightly convex along the longitudinal axis. This is not desired but has minor influence on the measured minimum OFT, because over a central small region of interest (1.16 mm high) – shown enlarged in Figure 3.10b – the curvature is negligible.

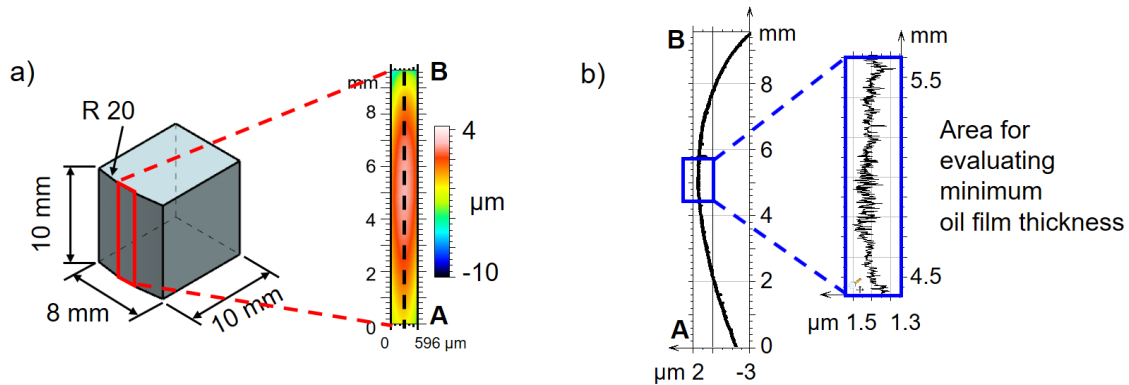


Figure 3.10: a) Geometry of the sapphire PRS and the contact surface topography. b) Vertical scan along the center line A-B of the topography with the blue box marking the section used for evaluating the minimum oil film thickness.

3.1.4 Experimental parameters and procedure

The operating parameters for the experiments on the tribometer were based on the load/sliding-speed trace of a typical 4-cylinder spark-ignition engine from Mercedes-Benz AG, shown in Figure 3.11. The latter was calculated by a Mercedes-Benz internal simulation tool at 6100 rpm. For the experiments in this chapter, a range of sliding speeds from 0-10 m/s was chosen, limited by the rotational speed of the RRV tribometer, and the normal loads were set to 10, 30, and 60 N. The lubricant used in this work was 0W-20 “first fill” engine oil with an HTHS (high temperature, high shear) viscosity of 2.6 mPa*s. The oil supply was adjusted to 0.1 mm³ per rotation. The hot-air temperature near the PRS was maintained at 80 °C.

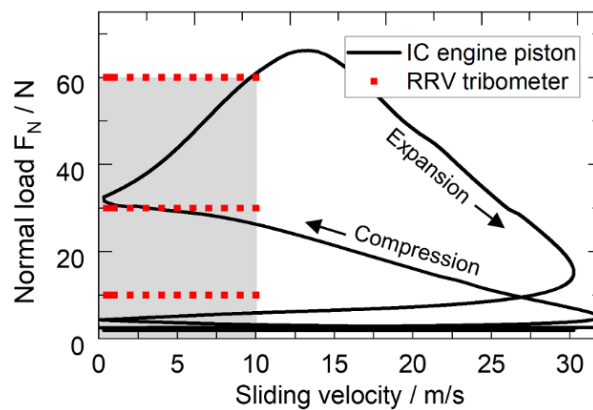


Figure 3.11: Normal-load/sliding-speed trace of a top piston ring in a typical spark-ignition engine from a simulation at 6100 rpm and with a line-contact of 10 mm. The range of operating points in the tribometer is marked with red dots.

3.1.5 Optical system for laser-based oil film thickness measurements

In this chapter, the optical system including the laser as a light source employed in chapters 3 and 4 to visualize the OFT is discussed.

3.1.5.1 LIF measurement system

Laser

Dyes are excited by a frequency-doubled Nd:YAG (Neodymium-doped yttrium aluminum garnet) laser (Litron LPY 742-100) with an excitation wavelength of 532 nm, a maximum repetition rate of 100 Hz and about 10 ns pulse duration. Using an internal trigger, the maximum repetition rate of 100 Hz is used to record standstill images. Otherwise, the relevant repetition rate according to the rotating speed is set by the phase coupling, while using a rotary encoder as an external trigger, as described next.

Phase coupling and synchronization

In order to record images at a fixed position of the liner during its operation and to control its timing, phase coupling was used. A universal synchronizer PTU (programmable timing unit) from the company LaVision generates precise trigger pulses for cameras, lasers and other external devices under the control of the software DaVis 8. Integrated with a rotary encoder, which reads a rotary angle position, the laser and camera are triggered at a given reference angle position at the right time with 10 ns resolution [148], i.e., each single image can be recorded per liner rotation for a tribometer (chapters 3-5) or per engine cycle for a single-cylinder optical engine in chapter 4.3.

Dye and filter

The oil is doped with a single dye of pyr 567 to measure the OFT (chapters 3 and 4), since the fluorescence dependency of the pyr 567 on the temperature is known (see chapter 3.1.5.2) and the temperature is constantly maintained in each chapter. Figure 3.12 shows the spectral features of the absorption and emission of the selected dye, the laser excitation, and the detection with the filter.

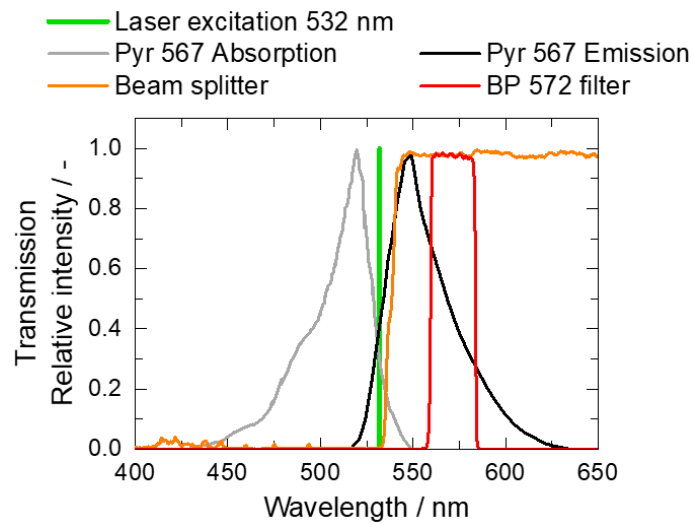


Figure 3.12: Spectral features of excitation, fluorescence, and detection [18] [149] [150].

Pyr 567 absorbs the laser excitation of 532 nm and emits the fluorescence light with the highest peak at about 560 nm. In order to separate the absorption and emission, a dichroic beam splitter (Semrock Inc.) with a single-edge at 532 nm is adopted. The fluorescence is detected through a band pass filter with a transmission wavelength of 572 nm and a FWHM (full width at half maximum) bandwidth of 25 nm providing further suppression of scattered excitation light.

Camera

The fluorescence signal is detected by an Imager sCMOS (CMOS: complementary metal oxide semiconductor) camera from LaVision. The camera in this work allows the resolution of 2560×2160 pixels with a pixel size of $6.5 \mu\text{m} \times 6.5 \mu\text{m}$. The relevant sensor size (active area) amounts to $16.6 \text{ mm} \times 14.0 \text{ mm}$. At the highest resolution, the frame rate of 50 fps (50 frames per second, which is 50 Hz) is available. The exposure time of $15 \mu\text{s} - 100 \text{ ms}$ is given and the detectable spectral range is from 370 nm to 1100 nm. The A/D converter of the CMOS camera operates with the digital output of 16 bit.

3.1.5.2 Preliminary experiments

Before applying LIF in the tribometer, the fluorescence of the film of the oil/dye mixture was examined as a function of some of the parameters that appear in the equations underlying the image quantification, e.g., equation (2.10). The preliminary tests were performed in a temperature-controlled thin-film cuvette shown in Figure 3.13.

3. Oil film thickness imaging on the metal cylinder liner

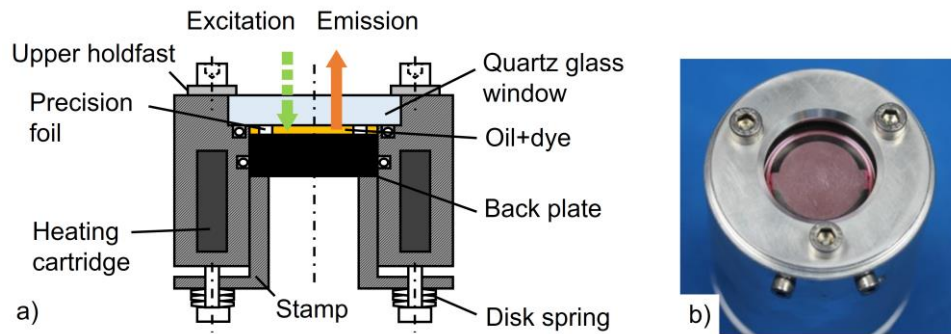


Figure 3.13: a) Schematic representation of a cut section of the thin film cuvette. b) Photo of the thin film cuvette.

The aluminum cylindrical equipment provides a well-defined OFT in a gap between the black painted back plate and the quartz glass window supported by stainless-steel precision foils. In order to avoid a leakage of the oil, the oil-filled space is sealed by O-rings and the stamp is loaded by disk springs to ensure the surface contact of the back plate, precision foils and window. By the help of three heating cartridges with closed-loop control, the temperature of the oil film can be varied. It is placed in the tribometer instead of the PR/CL to maintain the most same optical path as that in the experiment with the PR/CL assembly. The LIF intensity is evaluated by averaging over a region of 7×5 mm.

Photobleaching

Photobleaching is the phenomenon that a dye permanently loses its ability to fluoresce due to the photon-induced chemical damage. The fluorescence signal is gradually decreased during the LIF imaging, when the dye is exposed to the high intensity laser light for a long time. Shown in Figure 3.14, the photobleaching effect of the pyr 567 in a first-fill engine oil is investigated in the thin-film cuvette with different laser fluences. The OFT and the dye concentration are $20 \mu\text{m}$ and 0.1 mmol/L , respectively, and the trigger rate is 100 Hz .

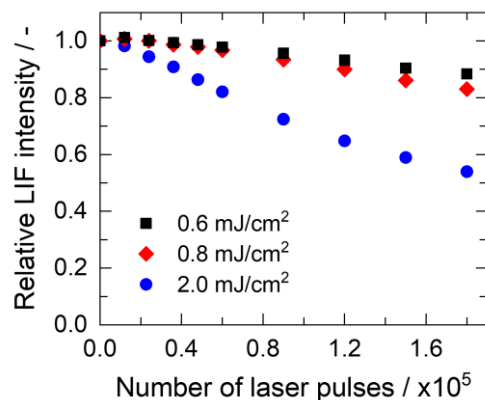


Figure 3.14: Photobleaching of pyromethene 567 with increasing number of laser pulses and different laser fluences. (OFT = $20 \mu\text{m}$, dye concentration = 0.1 mmol/L and trigger rate = 100 Hz)

The relative LIF intensity scaled by the first point decreases overall as increasing the number of laser pulses, i.e., by the time. After 0.12×10^5 laser pulses (2 minutes), each LIF intensity exposed to the laser fluence of 0.6 and 0.8 mJ/cm² respectively does not decline, while the LIF intensity exposed to the laser fluence of 2.0 mJ/cm² declines about 2 %. After 0.60×10^5 laser pulses (10 minutes), the LIF intensity exposed to the 0.6 mJ/cm² fluence decreases 2 %, the one exposed to 0.8 mJ/cm² decreases 3 % and the intensity exposed to 2.0 mJ/cm² is about 18 % lower than the initial fluorescence intensity.

The effect should be taken into account when the same oil/dye mixture is exposed consistently to the high energy of the incident laser light. In this work, the in-situ calibration and the recording of the flat-field image correspond to this case and thus, they are recorded in an initial few seconds. In the case of the image acquisition with a rotating liner against a static PRS, the photobleaching does not prevent the quantification, since the fresh oil/dye mixture is continuously supplied onto the liner surface during its rotation. Furthermore, the trigger rate is much lower during the rotation due to the phase coupled system (max. about 36 Hz with a sliding speed of 10 m/s).

Laser pulse energy

As mentioned in chapter 2.1.3, equation (2.10), the fluorescence intensity has a linear response to the input laser fluence (incident light intensity), when the fluence is small enough. However, high laser fluence can cause a non-linear response (or “saturation”) in which the fluorescence signal increases no longer linearly with increasing laser fluence. This may be due to ground-state depletion, where missing fluorescent dye molecules can no longer absorb additional photons or due to laser-induced effects in the excited state (such as further electronic excitation, ionization, or photofragmentation) [151].

The saturation curve with the high laser fluence is often well fitted by the following phenomenological equation [151] [152] [153] :

$$I_f = AI_{sat} \frac{I_0}{I_0 + I_{sat}} \quad (3.1)$$

where I_f is the fluorescence intensity, I_{sat} is the saturation fluence, I_0 is the initial intensity of the laser source and A is a fitting parameter, which includes the rest fluorescence factors. Figure 3.15a shows the LIF intensity as a function of the laser fluence between 0.05 and 9.0 mJ/cm² with the OFT from 20 to 100 μm. The constant dye concentration of 0.1 mmol/L was here used. Similarly, at a fixed OFT of 20 μm, the dye concentration was varied between 0.05 and 1 mmol/L and the laser fluence between 0.05 and 9.0 mJ/cm² in Figure 3.15b. Both results were fitted by the equation (3.1), using a least-squares fitting. Every measured point represents the result from a 100-shot averaged image. The measurement was carried out in the thin-film cuvette at a room temperature (23 °C) with pyr 567.

3. Oil film thickness imaging on the metal cylinder liner

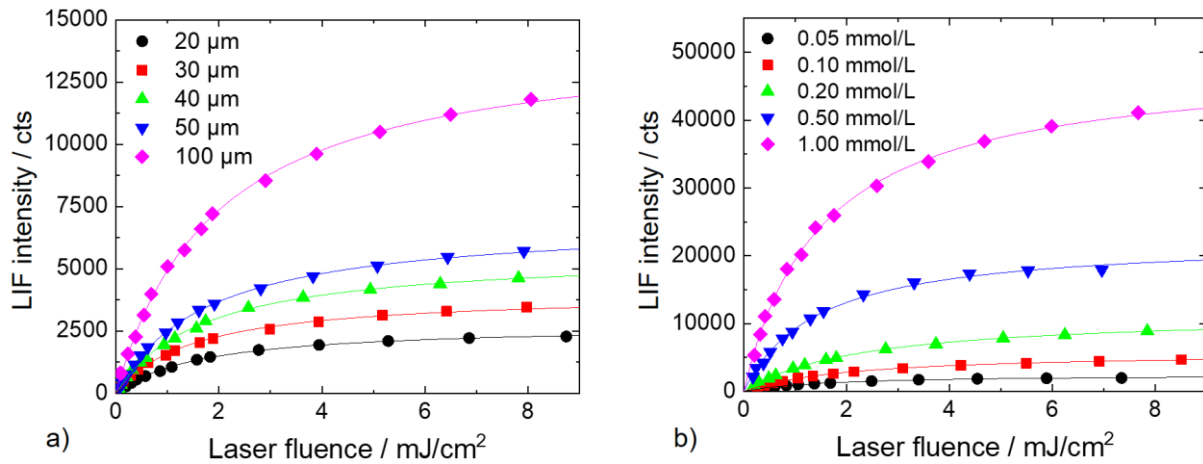


Figure 3.15: LIF intensity as a function of laser fluence a) with varied oil film thickness (with a dye concentration of 0.1 mmol/L), b) with varied dye concentration (at an oil film thickness of 20 μm).

As expected, the LIF intensity increases almost linearly at each OFT as well as each dye concentration, when the laser fluence is sufficiently small. However, it deviates from the linearity in the region of the high laser fluence. The saturation fluences I_{sat} from the equation (3.1) are calculated during the curve-fitting to be about 1.4 – 2.3 mJ/cm².

Nevertheless, the non-linear behavior of the LIF intensity for high laser fluence does not prevent the quantitative calibration of the OFT based on the linear approximation from the equation (2.10). As shown in the next paragraph, the linear approximation from the Beer-Lambert law is valid as long as the laser fluence is constantly maintained during the measurement. Considering the optic system setup and the signal-to-noise ratio, a laser fluence of 2.5 mJ/cm² for chapter 3 and 13 mJ/cm² for chapter 4 were chosen.

Thin-film approximation

Based on the results in Figure 3.15, a thin-film linear approximation suggested by the equation (2.10) is examined. Figure 3.16a presents the correlation between LIF intensity and OFT at a dye concentration of 0.1 mmol/L. As discussed, series of experiments were performed under various laser fluences in Figure 3.15a. For each laser fluence, the LIF intensity for all OFT was scaled by that at 20 μm OFT. Figure 3.16a shows the average with the error bars indicating the standard deviation over the different laser fluences, while Figure 3.16b shows the relationship between the LIF intensity and the dye concentration calculated from Figure 3.15b. Again, the measured LIF intensity at each fluence was normalized by the measurement at 0.05 mmol/L. All experiments were performed at room temperature.

3. Oil film thickness imaging on the metal cylinder liner

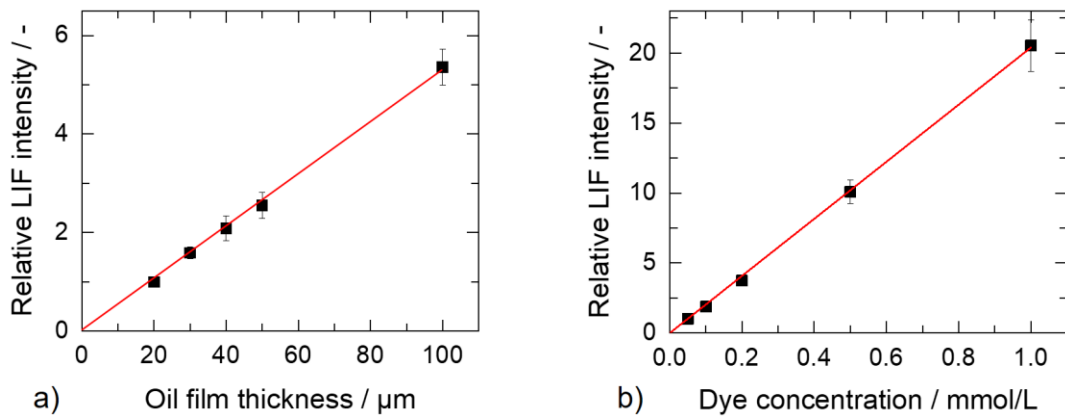


Figure 3.16: Relative LIF intensity as a function of the a) oil film thickness (with a dye concentration of 0.1 mmol/L) and b) dye concentration (at an oil film thickness of 20 μm). Error bars indicate the standard deviation over different laser fluences.

These two series of experiments show that for all fluences examined here the LIF intensity essentially is linear in OFT and dye concentration. Thus, the oil films are optically thin in the sense that the linear approximation of the Beer-Lambert law presented in equation (2.10) is valid in good approximation for to $c \cdot h < 20 \mu\text{m} \cdot \text{mmol/L}$. The vast majority of the measurements in chapters 3-4 uses a dye concentration of 0.1 mmol/L while a few measurements for a flat-field image or total internal reflection method adopt a dye concentration of 1.0 mmol/L .

Temperature dependency

In general, absorption and fluorescence – represented in equations (2.8 – 2.10) by ε and Φ – and thus the fluorescence signal are temperature-dependent. Figure 3.17 shows the LIF intensity from the oil/dye mixture (0.1 mmol/L , 20 μm thickness) measured as a function of temperature normalized with respect to the signal at 22 $^{\circ}\text{C}$.

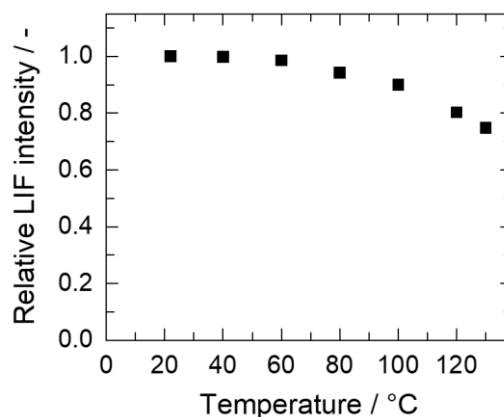


Figure 3.17: Relative LIF signal as a function of temperature (0.1 mmol/L dye concentration, 20 μm film thickness).

With respect to that base temperature, the signal at 80 °C is about 6 % lower and at 130 °C about 25 % lower. This is in a good agreement with the results of Müller [42], who found that the LIF signal of the same oil/dye combination decreased by 8 % when increasing the temperature from 50 to 90 °C, but is inconsistent with the results of Wigger [18], who found slightly increasing signal with increasing temperature with the same oil/dye combination, but with a higher fluence of 30 mJ/cm². This issue needs further investigation. In chapter 3.1.7, we utilize the data represented in Figure 3.17 by multiplying LIF intensity acquired at room temperature (e.g., the LIF intensity at standstill for the calibration in Figure 3.25a) by a factor of 0.94 to account for the deviation in expected signal with respect to the tribometer measurements at nominally 80 °C.

3.1.6 Image acquisition

Figure 3.18 shows the optical path of the experiment. Fluorescence was excited by a frequency-doubled Nd:YAG laser at 532 nm, a maximum repetition rate of 100 Hz and about 10 ns pulse duration. A small fraction of the laser energy was detected by an online energy monitor simultaneously with the acquisition of fluorescence images to correct for shot-to-shot energy fluctuations. The beam was then expanded and formatted by a slit aperture to illuminate the region of interest. Then, the beam was reflected by a dichroic beam splitter for coaxial illumination and detection. The tribometer has a post that is in the way of directly illuminating the optical access. Therefore, a mirror was installed on this post to redirect the light. Through the glass window of the heater sleeve, the laser light was coupled into the periscope-like PRS holder as shown in Figure 3.8 to reach to the oil film on the PR/CL contact. The fluorescence light from the oil film passed through the beam splitter. A band pass filter with a transmission wavelength of 572 nm and with a FWHM (full width at half maximum) bandwidth of 25 nm provided further suppression of scattered excitation light, while fluorescence was detected by a CMOS camera with a Nikon 200 mm macro lens at an aperture of f/4 and a 2x teleconverter.

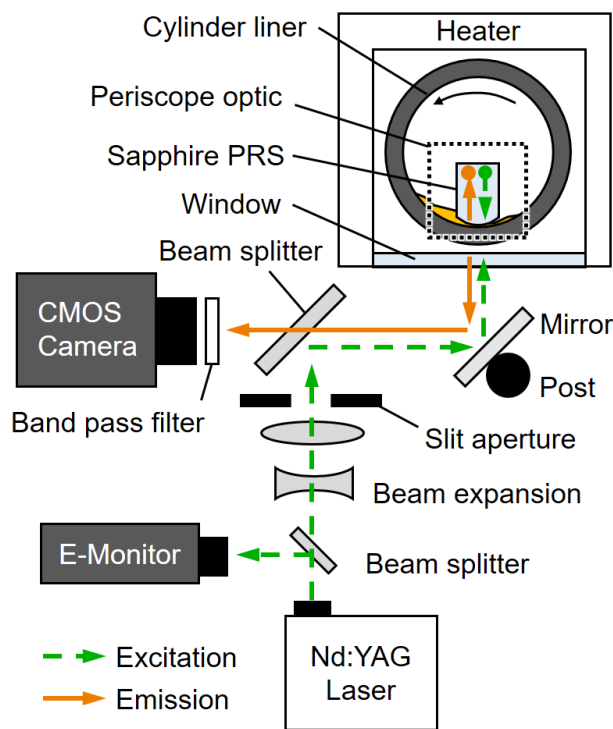


Figure 3.18: Optical path layout including periscope optic.

3. Oil film thickness imaging on the metal cylinder liner

Figure 3.19 is the photos of the experimental setup, which were schematized in Figure 3.18. In order to show the PR/CL assembly better, the heater sleeve was removed here, but still the (disconnected) hot-air heater is shown in the left photo. From the same reason, the metal cylinder liner does not cover the sapphire PRS in the right enlarged photo.

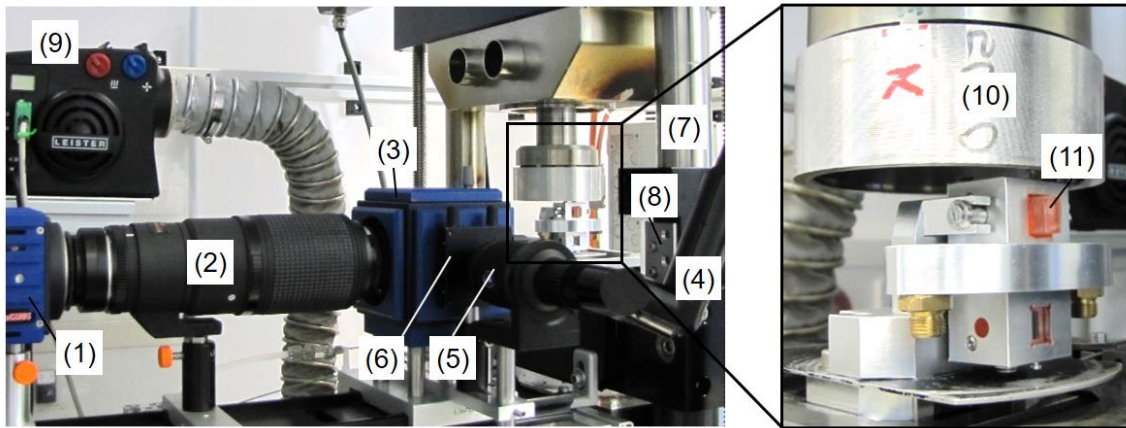


Figure 3.19: Photos of the optic setup for image acquisition. (1) CMOS camera, (2) 200 mm macro lens with a 2x teleconverter, (3) beam splitter, (4) laser guiding arm, (5) laser beam expansion, (6) slit aperture, (7) tribometer post, (8) mirror, (9) hot-air heater, (10) metal cylinder liner and (11) sapphire piston ring segment

RRV-tribometer laboratory shown in Figure 3.20 was equipped with the previous mentioned systems to implement the optic measurement with the laser.

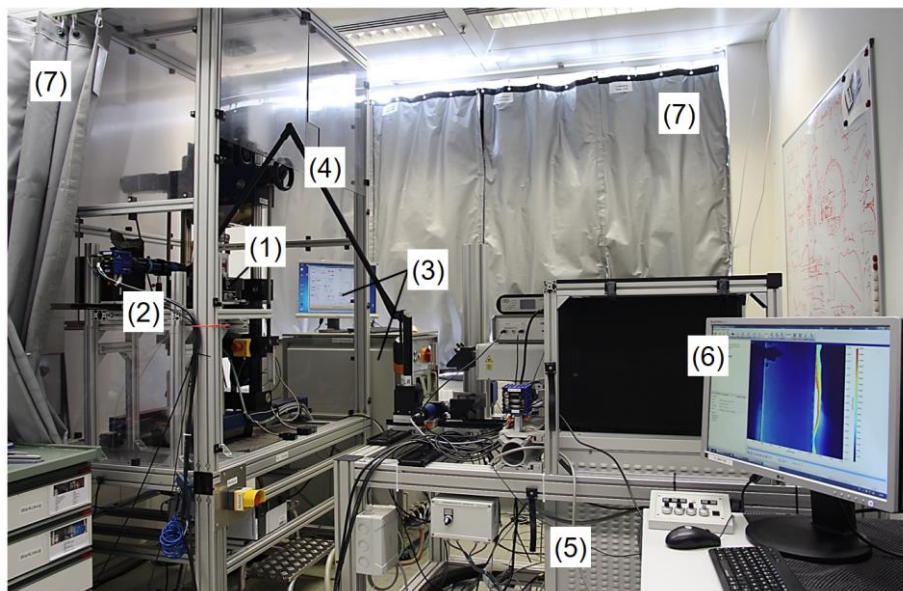


Figure 3.20: Setup in the RRV-tribometer laboratory. (1) RRV-tribometer, (2) camera and detection system, (3) control PC for the tribometer, (4) laser guiding arm, (5) laser system, (6) control PC for the detection system and (7) laser safety curtain.

In an acryl booth, the RRV-tribometer and the detection system are assembled and positioned to protect the laser cart from the possible spattered oil. A laser-guiding arm guards the excited laser from the laser system on the cart to the measurement area in the booth. Behind the booth, a control PC for the tribometer operation is placed. A laser safety curtain prohibits the leakage of the laser light through the window for the safety. Another laser safety curtain separates the area with the control PC for the detection system from the laser running area, although the laser safety glasses are always used to protect the eyes.

Using a 2 mm grid paper as shown in Figure 3.21, the projected pixel size was measured. The grid paper was positioned between the sapphire PRS and the metal cylinder liner and a slight normal load was given to ensure the contact. The distances between two angular points were calculated in pixel, averaged and compared to the metric grid size. The projected pixel size was 5.75 $\mu\text{m}/\text{pixel}$.

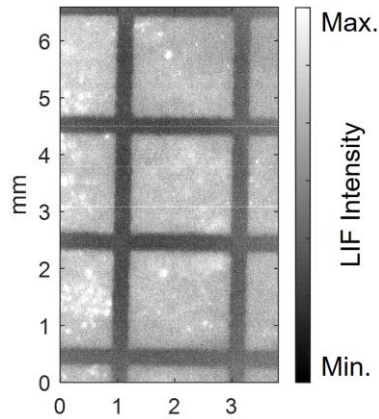


Figure 3.21: Determination of projected pixel size with 2 mm grid paper

3.1.7 Image processing

The raw LIF image I_S recorded by the camera is converted to the quantitative oil film thickness H via equation (3.2). Here, capital letters indicate two-dimensional images and brackets $\langle \rangle$ average over a series of 100 single shots. The terms in equation (3.2) are discussed in the following.

$$H = (I_S - \langle I_{BG} \rangle) \cdot \frac{1}{\langle I_{FF,norm} \rangle} \cdot \frac{e_{ref}}{e_{measured}} \cdot \frac{1}{t_{cal}} \quad (3.2)$$

Background correction

An average background image I_{BG} is recorded without oil and dye but with laser excitation. Subtraction eliminates the dark current of sensor, the A/D-converter-offset, and the possible background or surroundings fluorescence. The recorded, averaged background image is shown in Figure 3.22.

3. Oil film thickness imaging on the metal cylinder liner

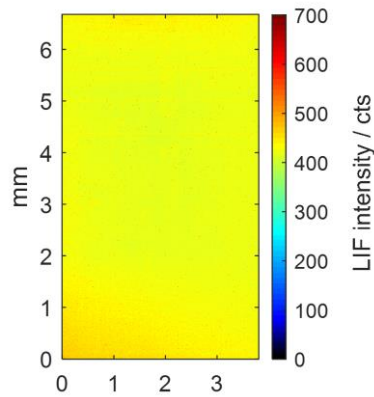


Figure 3.22: Averaged background image with laser but without oil/dye mixture

Flat-field correction

The second step is a flat-field correction I_{FF} that accounts for any inhomogeneity of the instrument throughput across the field of view, which is essentially the product of laser intensity I_0 and detection efficiency $\Omega \eta$. Here, an in-situ flat-field image is acquired.

Equation (2.10) shows that the detected LIF signal is a linear function of $I_0 \Omega \eta$ if the oil film thickness h approaches infinity:

$$\lim_{h \rightarrow \infty} I_f \propto \Phi \cdot I_0 \cdot \Omega \cdot \eta. \quad (3.3)$$

Here, an oil bath with a depth of 25 mm provides a nearly infinite OFT in comparison to that in the PR/CL contact, less than $20 \mu\text{m}$. It was attached to a quartz liner by a heat-resistant silicon adhesive as shown in Figure 3.23a and Figure 3.23b. PAO (poly-alpha-olefin), transparent non-fluorescent base oil, was filled into the gap between the sapphire PRS and the quartz liner as an immersion oil. The recorded flat-field image was normalized with respect to its average intensity (for convenience) and this $I_{FF, norm}$ is shown in Figure 3.23c.

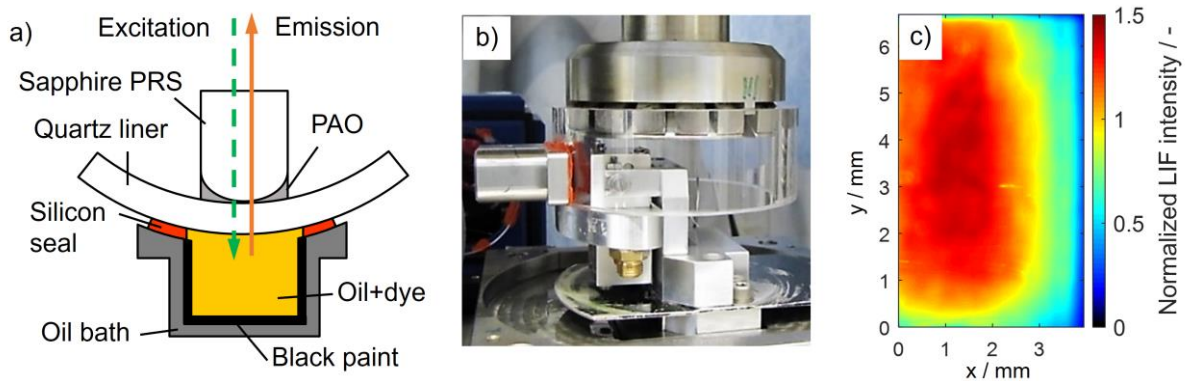


Figure 3.23: a) Schematic sketch and b) photo of the flat-field acquisition. c) Flat-field image normalized with respect to the average intensity.

The images from two individual recordings were divided by each other as shown in Figure 3.24 and the intensity ratio distribution across the field showed a standard deviation of 5.4 %, which may be taken as a rough estimate of the accuracy uncertainty associated with this method.

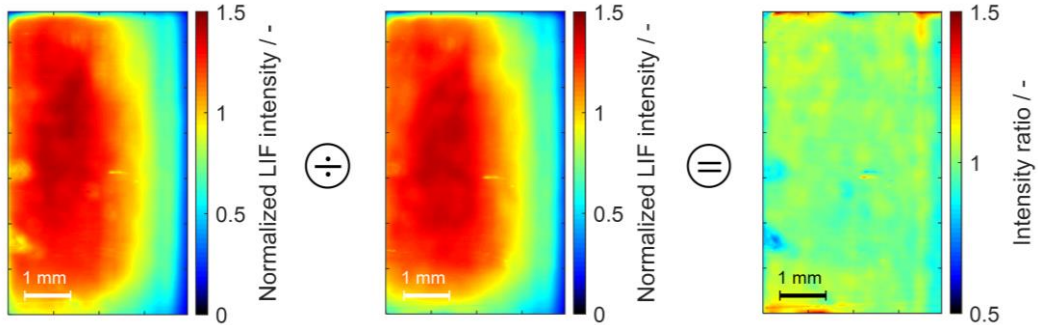


Figure 3.24: Repeatability of the flat-field measurement. Intensity ratio distribution across the field and its standard deviation of 5.4 %

Pulse-to-pulse laser energy fluctuation was accounted for based on the simultaneously-recorded fraction of the pulse energy e . The ratio of $e_{measured}$ to the reference laser energy e_{ref} (the average energy during the whole measurement) was multiplied with the flat-field corrected intensity.

Absolute calibration

The in-situ calibration determining the ratio t_{cal} between the flat-fielded LIF intensity and the OFT followed the technique proposed by Müller [42]. The gap between the sapphire PRS and the (honed metal) liner was filled with oil/dye-mixture and the PRS was loaded at stand still. As shown in Figure 3.25, the calibration exploits the slight curvature of the PRS along the vertical centerline A-B seen in Figure 3.10b.

3. Oil film thickness imaging on the metal cylinder liner

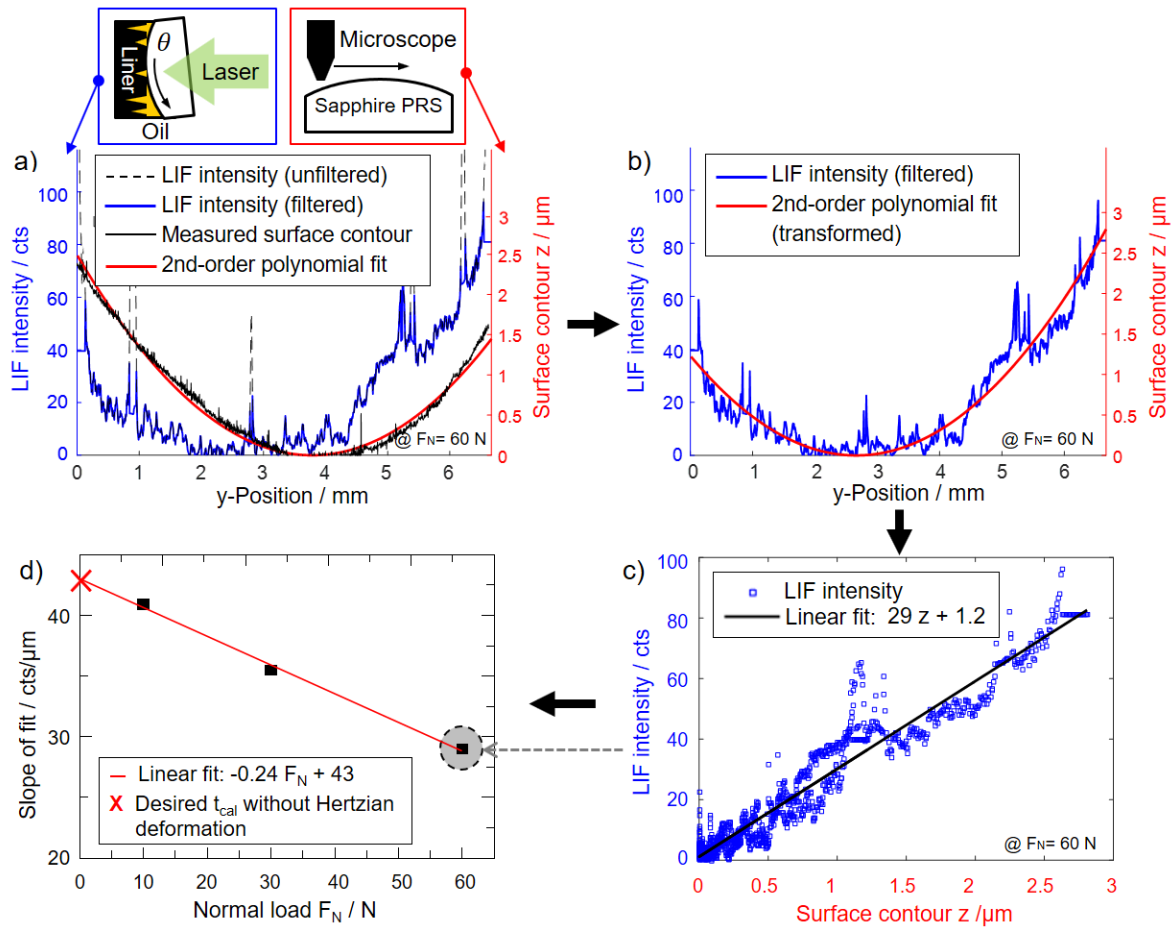


Figure 3.25: Procedure to determine the calibration factor t_{cal} using the slight curvature of the PRS along the vertical axis via an affine transformation, shown here for the LDS liner. a) Measured and filtered LIF intensity in the PR/CL contact, measured and curve-fit surface contour of the PRS, b) PRS surface contour matched to the LIF intensity via the affine transformation, c) correlation between surface contour and LIF intensity, and d) extrapolation of the calibration factor t_{cal} to zero normal load.

The background and flat-field corrected LIF intensity in a vertical section through the contact zone (Figure 3.25a, blue trace) is compared to a second-order polynomial fit (red trace) to the vertical surface contour of the PRS measured by confocal microscopy (Figure 3.25a, black solid trace, also shown in Figure 3.10b.). The blue trace in Figure 3.25a shows the in-situ measured LIF intensity in the case of the LDS liner. For this type of liner, the very high peak intensities from the deep pores (black dashed trace) were partially suppressed by a combination of a median filter and thresholding. The remaining fluctuations in LIF intensity stem from the sum of the honing structure on the LDS liner and the surface roughness of the PRS (see Figure 3.9 and Figure 3.10b). As discussed in section 3.1.2, the PRS holder can pivot to compensate the eccentricity of the liner surface during the liner's rotation. In order to determine the unknown tilt angle θ of the PRS and thus to fit the two measured traces to each other, the affine transformation for a rotation and translation was used.

$$[y_r \ z_r] = ([y \ z] - [l/2 \ r_{pivot}]) \cdot \begin{bmatrix} \cos\theta & \sin\theta \\ -\sin\theta & \cos\theta \end{bmatrix} + [l/2 \ r_{pivot}] \quad (3.4)$$

$$[y_{r,t} \ z_{r,t}] = [y_r \ z_r] - [0 \ \min(z_r)] \quad (3.5)$$

$[y \ z]$ in equation (3.4) is a quadratic polynomial function from a least-square fit (Figure 3.25a, red trace) to the measured surface contour from Figure 3.10b, while l is the total LIF image height in y in Figure 3.25a (6.7 mm, see field of view in Figure 3.31a), and r_{pivot} is the distance from the PR/CL contact point to the pivot point of the PRS holder as shown in Figure 3.8a (14.5 mm). With equation (3.4) the function $[y_r \ z_r]$ is deduced by a rotatory (tilt) motion by an estimated initial angle θ about the pivot point. A possible z -offset after rotation ($\min(z_r)$) is eliminated by the equation (3.5). Physically, this represents the fact that the PRS is pushed against the liner. The transformation with rotation and translation is repeated iteratively to find a least-squares-optimized θ with respect to the measured, filtered LIF intensity. The red trace in Figure 3.25b shows the transformed and optimized $[y_{r,t} \ z_{r,t}]$, which is in a good agreement with the LIF intensity, apart from the small-scale fluctuations of the signal corresponding to the sum of the honing structure and the surface roughness of the PRS. Figure 3.25c presents the correlation between the LIF intensity and the transformed PRS surface elevation. The calibration factor is determined as the slope of a linear fit to the data. However, the LIF measurement is carried out in-situ under a finite normal load, which induces Hertzian deformation, while the surface contour is measured by microscopy ex-situ unloaded. This discrepancy between the loaded in-situ and unloaded ex-situ measurements is demonstrated by Figure 3.25d, showing different slopes of fits from different normal loads. The final desired calibration factor t_{cal} without any deformation is then obtained by extrapolating a least-squares linear fit to zero normal load. t_{cal} for the LDS liner was 43 cts/ μm and 65 cts/ μm for the GG liner. The difference between the values for the two liner surfaces is likely due to their different reflectivity, which strongly influences the detection efficiency $\Omega\eta$ (equation (2.10)) as discussed by Wigger et al. [76]. Dividing the flat-fielded, energy-corrected intensity by the relevant calibration factor yields the oil-film thickness H .

The entire image processing chain to quantify the oil film according to the equation (3.2) is depicted in Figure 3.26 as a flowchart with some example LIF images.

3. Oil film thickness imaging on the metal cylinder liner

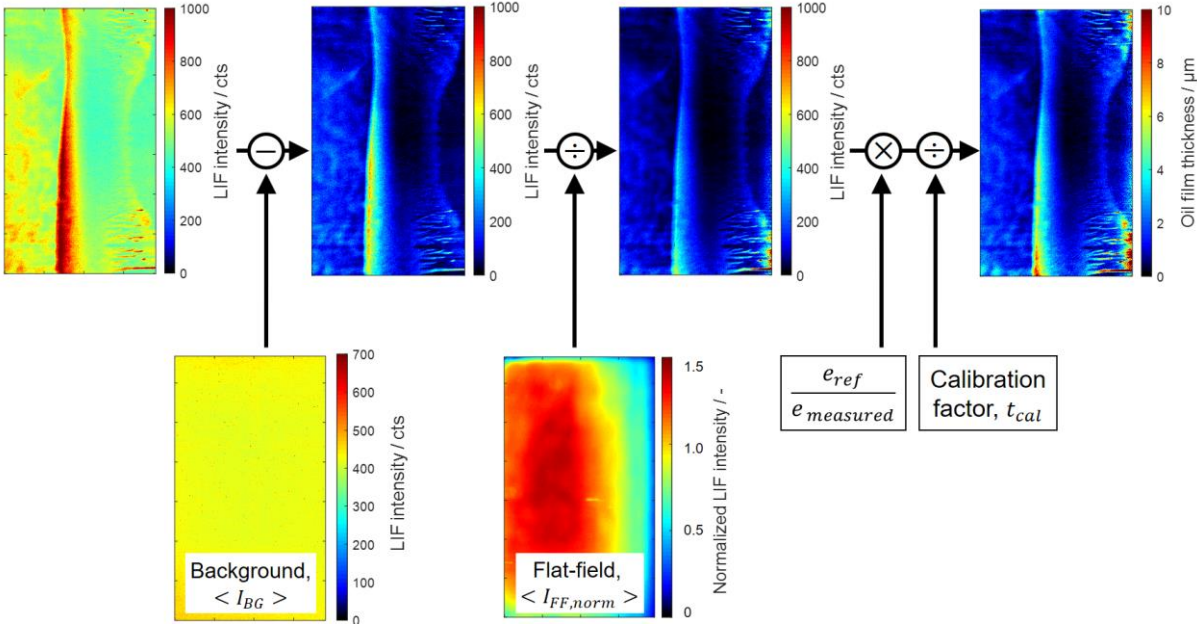


Figure 3.26: Flowchart of the image processing including background-, flat-field, energy corrections and an absolute calibration.

3.1.8 Effect of fluorescence stray light on measured minimum oil film thickness

As studied by Miller [154] and Obert et al. [77] [155], stray fluorescence from the surroundings can falsely contribute to the region where the film thickness is relatively thin. Miller assumed that the stray light occurred only from a far-off back wall and generated a kernel with which images were corrected via direct inverse filtering. Obert first blocked illumination from reaching the center region in the oil-filled PR/CL contact, where the minimum OFT is measured. They determined that the detected intensity in the blocked region, i.e., that solely from stray light, and the total fluorescence intensity in the surroundings have linear relationship. To suppress this stray light, they limited the illuminated area – but thereby also the useful field of view – to a narrow strip. Also in our work, the fairly weak LIF signal in the evaluation area may be affected by the oil-filled surroundings, especially the inlet area. The stray light in the evaluation area in this work could possibly result from the following reasons (Figure 3.27).

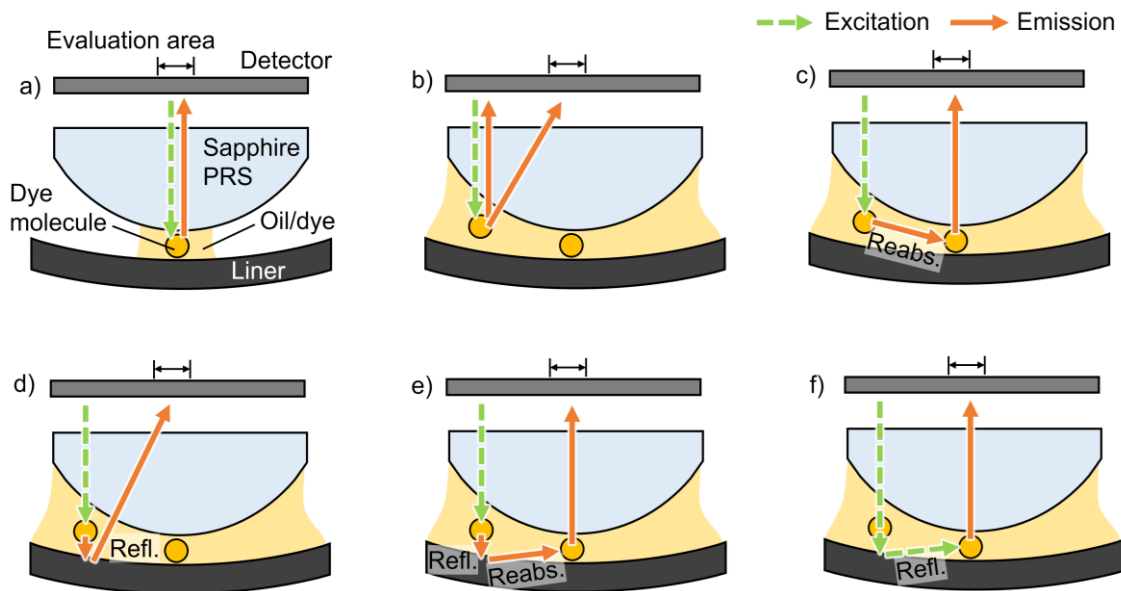


Figure 3.27: a) Preferred LIF signal detection from the minimum OFT in the evaluation area without stray light effect from the surrounding oil. b-f) Possible stray light sources in the evaluation area

First, the fluorescence signal from the surroundings with relatively thick oil film could be falsely detected in the evaluation area as shown in Figure 3.27b, since the fluorescence light is emitted in various direction. This could contribute to the unwanted stray light effect severely, because very weak LIF signal would be detected from the thin oil film in the evaluation area due to the PR/CL gap geometry. Conversely, this false contribution from the surroundings to the evaluation area would not occur, if the oil/dye could only exist within the evaluation area as shown in Figure 3.27a or the evaluation area could be solely illuminated as conducted by Obert [155]. Second, the stray light might be caused, since the absorption and emission spectra of the pyr 567 are partially overlapped at around 530 nm as shown in Figure 3.12. A part of the fluorescence emission from the surroundings could be thus re-absorbed by the dye

3. Oil film thickness imaging on the metal cylinder liner

molecule in the evaluation area (Figure 3.27c) and an additional fluorescence from that could be measured. Third, as Miller suggested, the fluorescence from the surroundings could be specularly and/or diffusely reflected by the back wall, which is the liner's inner surface in this work (Figure 3.27d), and induce a false elevation of the detected signal in the evaluation area. Fourth, if this fluorescence reflection from the surroundings would reach to the dye molecule in the evaluation area like Figure 3.27e, it could be again re-absorbed and yield unwanted fluorescence here. Finally, the incident laser light could be specularly and/or diffusely reflected by the liner surface as in Figure 3.27f and this reflection could additionally excite the dye molecule in the evaluation area. Hence, a method to correct the stray light intensity is necessary for evaluating the minimum OFT in the evaluation area. The procedure applied here has two steps:

1. Empirical calibration: Figure 3.32 and Figure 3.33 in the next chapter show that the leading edge of the oil-filled zone in the inlet comes closer to the contact area with increasing sliding speed. These different oil-filled surroundings can yield different stray light intensities in the evaluation area and it was reproduced by blocking different portions of the laser beam in the inlet region as shown in Figure 3.28 and Figure 3.29a. In the outlet region, the laser beam was totally blocked, because Figure 3.32 and Figure 3.33 showed that the outlet area directly next to the evaluation region was not fully filled and often the oil film was disrupted by the cavitation pattern. We assumed that the stray light originates only from the leading edge of the oil-filled zone in the inlet region. Blocking the incident laser beam was achieved by painting the PRS black using a graphite lacquer. The width of the unblocked region next to the evaluation area is designated as d (see Figure 3.28).

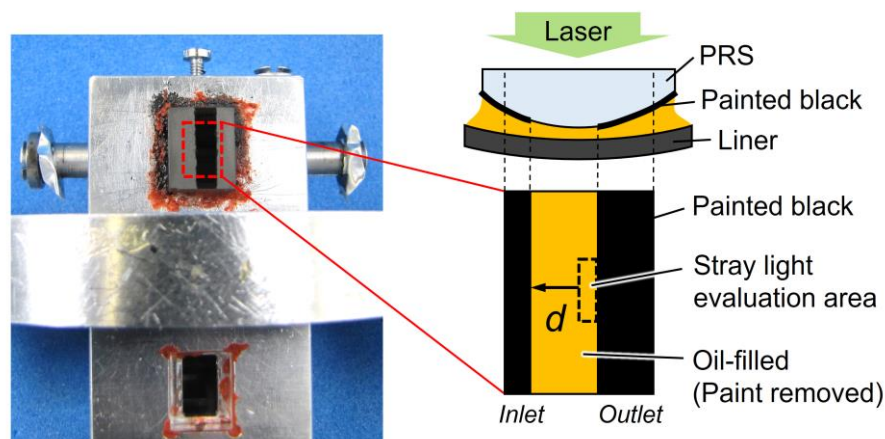


Figure 3.28: Photo of the partially black painted sapphire PRS using a graphite lacquer (left). Enlarged, schematic field of view, which would be detected by camera (right).

For this measurement, the gap between the PR/CL was filled by the oil/dye mixture and loaded to ensure contact between PR/CL in the standstill tribometer. Without the stray light, a similar level of the signal (near zero) is expected in the evaluation area for each case, because the

3. Oil film thickness imaging on the metal cylinder liner

amount of dye in the evaluation area is the same for all cases. However, the data points in Figure 3.29a show increasing signals in the evaluation area, caused by stray light, when expanding the oil-filled surroundings.

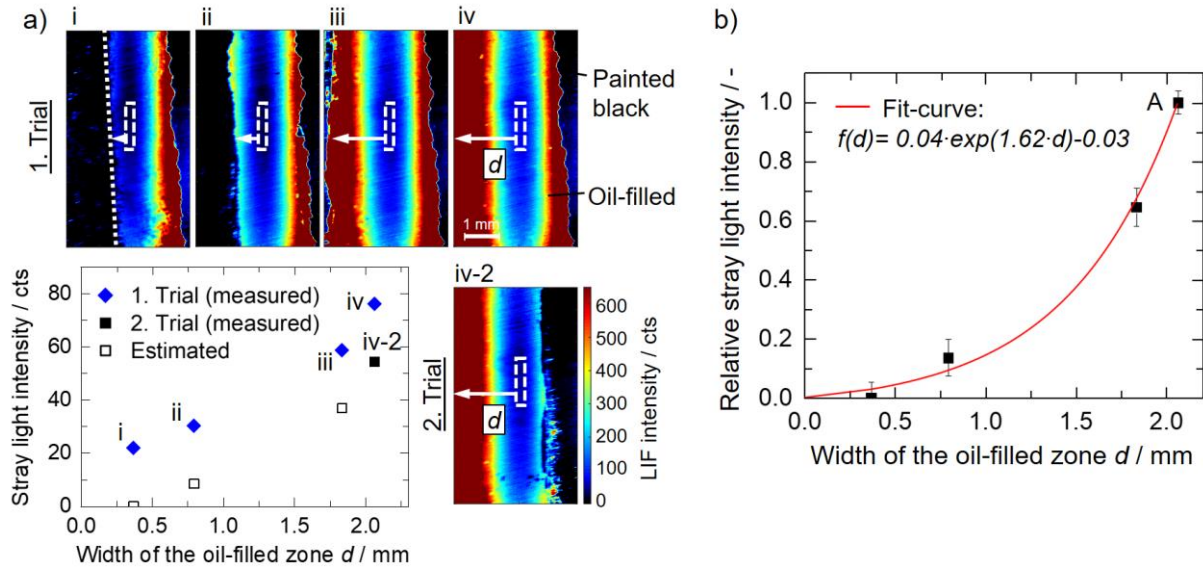


Figure 3.29: Empirical calibration of stray light. a) LIF images as blocking different portions of the laser beam by black paint and the measured stray light intensity in the evaluation area. b) Relative stray light intensity in the evaluation area as a function of d , width of the oil-filled zone next to the evaluation area, in the PR/CL contact. Error bars indicate the standard deviation over four individual measurements.

The operation of manual removal of the painted black using a cotton swab was not trivial; therefore, the two series of the trials were adopted to estimate the stray light intensity. The first trial set (Figure 3.29a-i, ii, iii and iv) shows that the same portion of the laser beam was blocked in the outlet region, while increasing d values were achieved in the inlet region. One defect factor here is that the outlet region was not fully blocked and some stray light from this region was additionally involved in the evaluation area. The second trial (Figure 3.29a-iv-2) shows that the outlet region was almost fully blocked as intended, but we failed to remove the black paint in the inlet region gradually, and only a fully filled inlet could be achieved. Here, the stray light intensity deviation between the point iv and iv-2 in the Figure 3.29a graph is equivalent to the stray light amount from the non-blocked outlet region in the first trial, which was not intended. This deviation was subtracted from each stray light intensity in the first trial and the result is designated as “estimated” points. Overall, the expected LIF signal from residual oil

due to the surface roughness $\sigma = \sqrt{S_{q,ring}^2 + S_{q,liner}^2}$ [156] was estimated as $I_{Roughness} = t_{cat} \cdot \sigma$ and was subtracted such that only the signal due to stray light is shown in the graph in Figure 3.29a. The signals are normalized with respect to the highest stray light signal from the fully filled inlet (point iv-2 in Figure 3.29a or point A in Figure 3.29b). The standard deviation over four individual measurements at each width d was at most 6.4 %. The relationship between

the stray light signal in the evaluation area and the width of the oil-filled zone d was approximated as an exponential function determined by a least-squares fit to the data in Figure 3.29b.

2. Image correction: In each series of measurements, a standstill image with fully filled oil without any blocked area was recorded before starting the tribometer (Figure 3.30a, in the case of GG liner). We assume that at standstill the symmetrical surface geometry of the PRS yields the same stray light signal from both the left and right side as indicated by the black arrows in Figure 3.30a. Therefore, first $I_{Roughness}$ is subtracted from the detected intensity ($I_{det,GG}$) in the evaluation area in Figure 3.30a and then the remaining intensity – presumably solely from stray light – is divided by two: $I_{A,GG} = (I_{det,GG} - I_{Roughness}) \cdot 1/2$ where $I_{A,GG}$ now corresponds to that in point A of the fit-function in Figure 3.29b that was generated with the entire inlet region illuminated. The stray light intensity correction is then given by $I_{corrected} = I_{uncorrected} - I_{A,GG} \cdot f(d)$. Here, d in the recorded images is determined by visual inspection. The same procedure is also applied to images with the LDS liner.

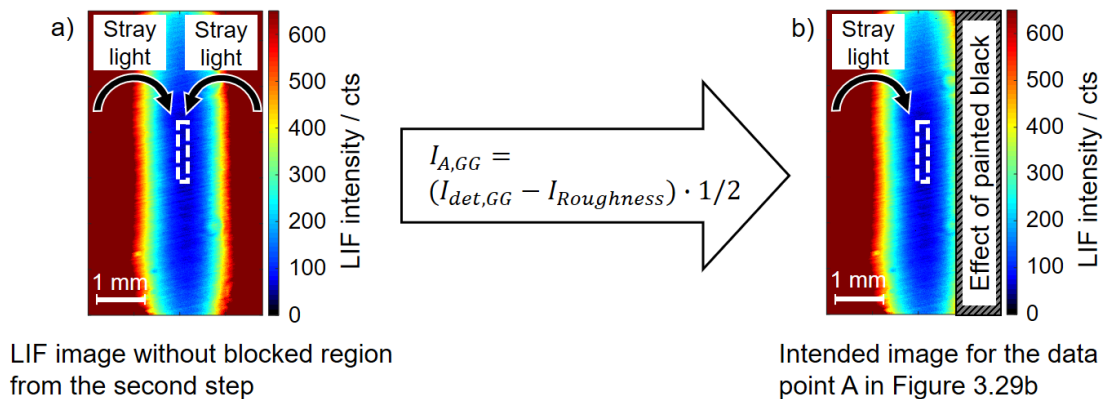


Figure 3.30: a) LIF image without blocked region (e.g., GG liner). b) Intended image for the point A in Figure 3.29b with the effect of painted black in the outlet region.

When the leading edge of the oil-filled zone in Figure 3.32 or Figure 3.33 is not straight, average width d was employed that can cause inaccuracy. Another uncertainty is the residual surrounding signal that is not from between the leading edge of the oil film and the evaluation area, for example, from the recirculating oil adhering to the PRS surface or on the liner as seen in Figure 3.32 and Figure 3.33. We presume that this region has an insignificant effect on the lateral center because the oil is only partially gathered and far away from the evaluation area. Nevertheless, the corrected OFT especially at low sliding speeds should be discussed carefully, because it has a relatively strong stray light correction due to the large d and low LIF signal from its thin film.

3.2 Results

3.2.1 Liner surface structures

With the basic checks from the preliminary experiments on some of the assumptions underlying the measurement completed, the oil film in the moving PR/CL contact was examined for different liner surfaces, loads, and velocities. Figure 3.31 shows the field of view through a sapphire PRS. With about 3.8×6.7 mm (width \times height), it is smaller than the whole area of the PRS due to the space taken up by the mount and the sealing (red dotted box). Example LIF images with oil-filled honing structures as well as surface pores are also shown in Figure 3.31b-d. On the LDS liner in Figure 3.31b, black arrows point to oil-filled pores with diameters of $50\text{-}80\ \mu\text{m}$. White arrows in Figure 3.31d, which is partially enlarged from Figure 3.31c, indicate the honing structures at about 15° angle on the GG liner. The honing structures are mostly less than $0.5\ \mu\text{m}$ deep according to the GG liner's topography shown in Figure 3.9. Hence, the optical system developed in this chapter is sufficient to image the oil-filled surface structures on the conventional liner.

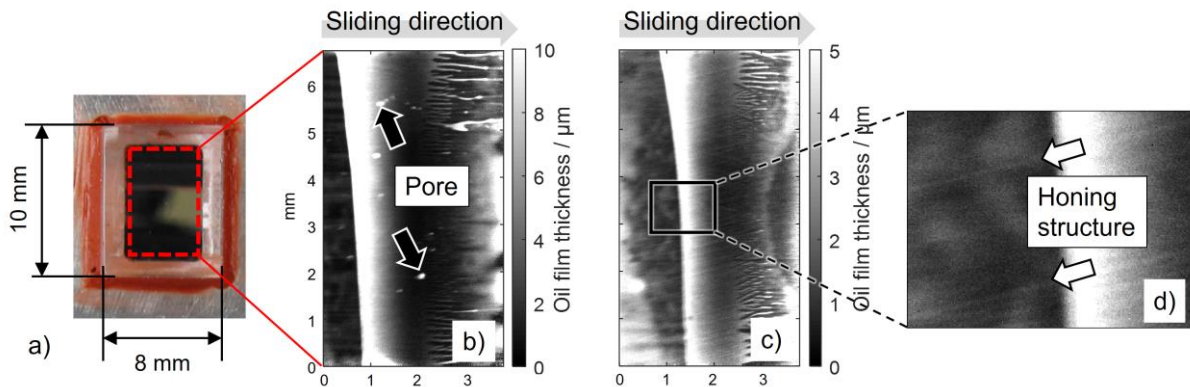


Figure 3.31: a) LIF field of view through a sealed sapphire PRS. b) Example LIF image of the oil film on the LDS liner. Arrows indicate the oil-filled pores. c-d) Example LIF image of the oil film on the GG liner. White arrows point along oil-filled honing structures. $T = 80\ ^\circ\text{C}$, $F_N = 10\ \text{N}$, $v = 0.5\ \text{m/s}$, exposure time = $1\ \text{ms}$, recording rate = $1.9\ \text{Hz}$ in both cases. Note that c) and d) are on a different grayscale than b).

3.2.2 2D-imaging of the oil film behavior

Figure 3.32 and Figure 3.33 present example single-shot LIF images of the oil film on each GG and LDS liner with varied sliding speeds and normal loads. The direction of oil entrainment is from left to the right. As mentioned above, every image was taken at the same position of the cylinder liner by means of a rotary encoder, such that for example the position of the pores in the LDS liner images appears fixed. In Figure 3.32 and Figure 3.33, the area from which the minimum OFT was extracted, as analyzed in next sections, is marked by a white dashed box of 0.17×1.16 mm near the lateral center.

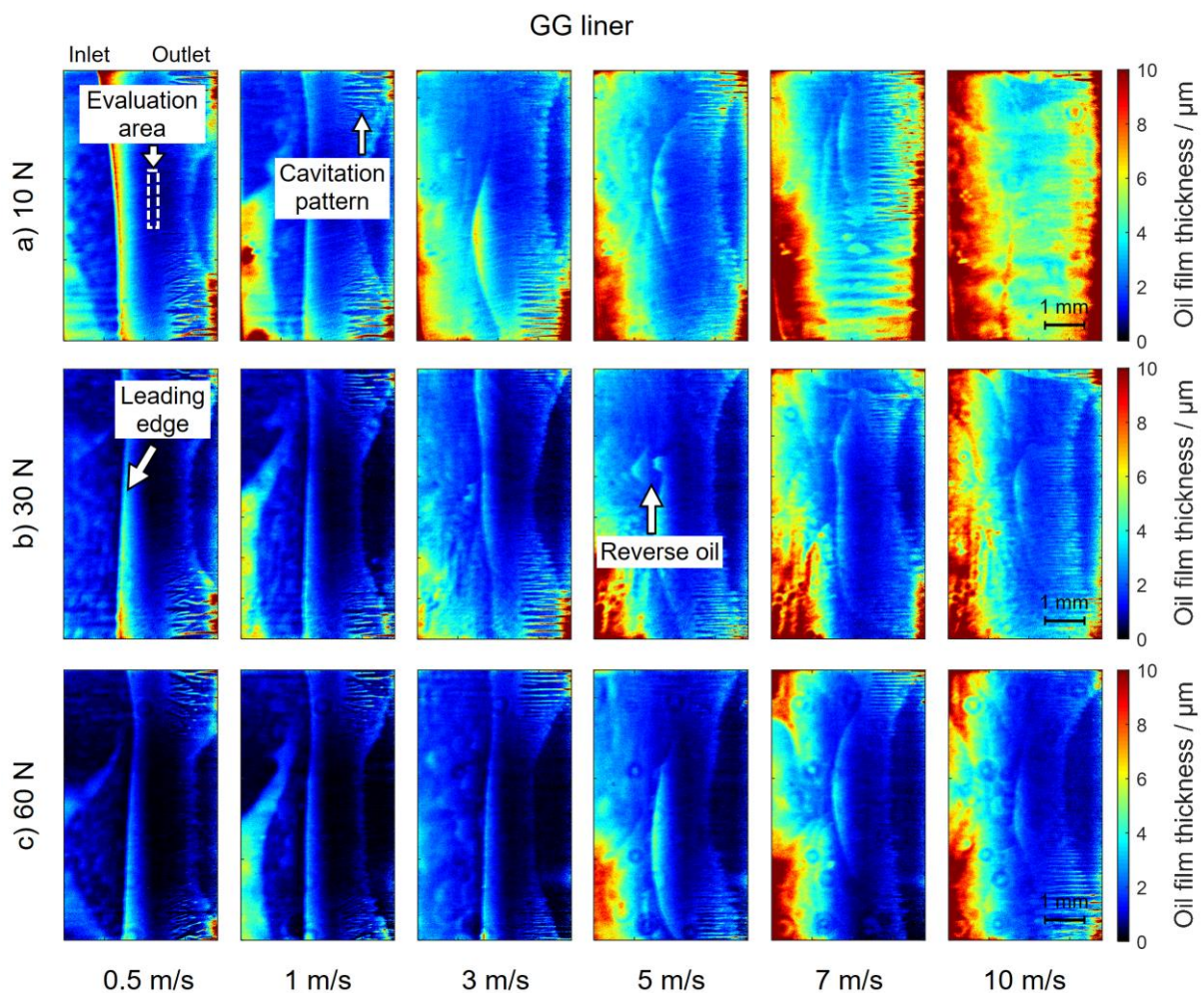


Figure 3.32: Quantitative LIF imaging of the oil film distribution on the GG liner within the PR/CL contact with increasing sliding speed. Normal load F_N was varied from 10 to 60 N.

3. Oil film thickness imaging on the metal cylinder liner

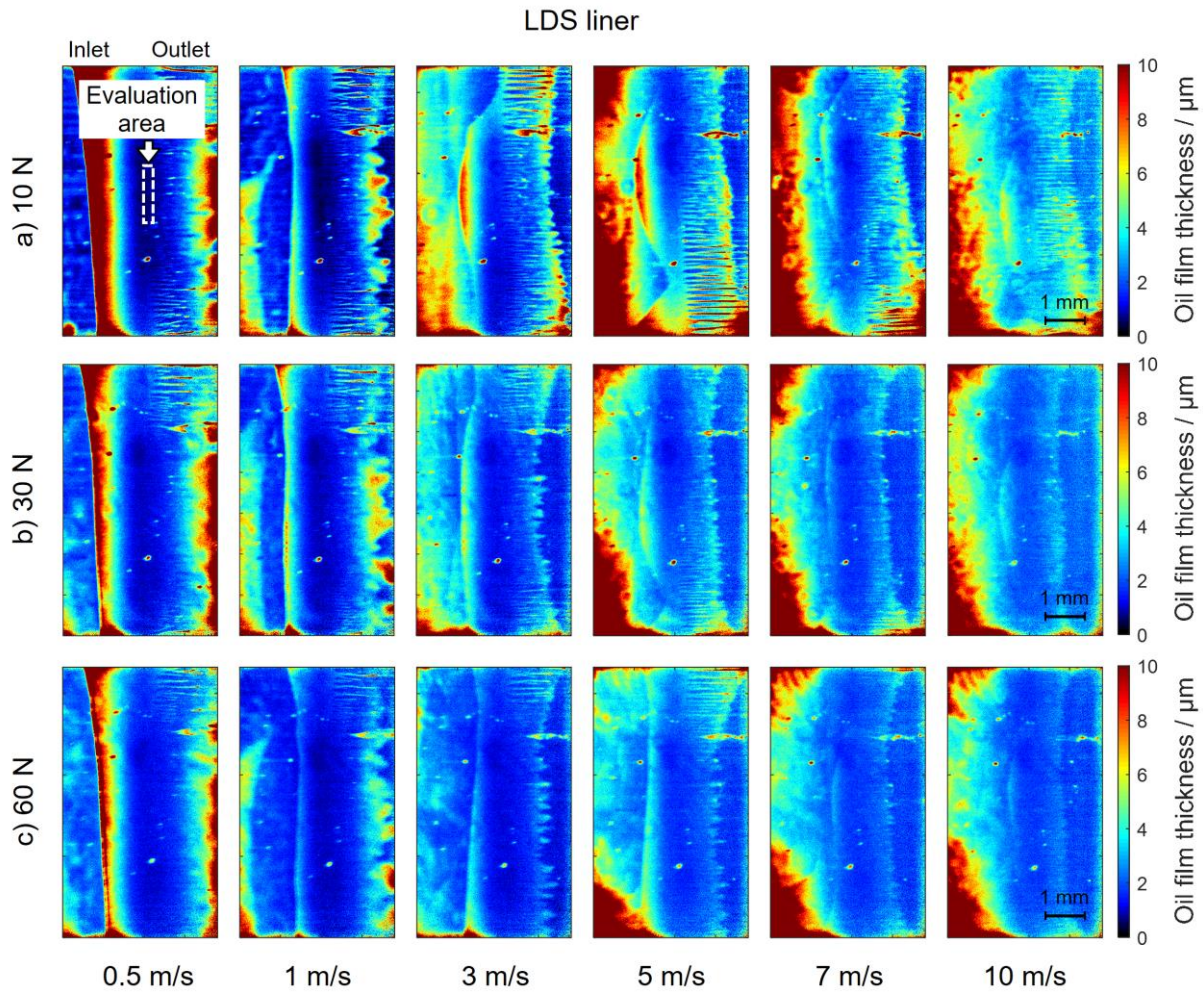


Figure 3.33: Quantitative LIF imaging of the oil film distribution on the LDS liner within the PR/CL contact with increasing sliding speed. Normal load F_N was varied from 10 to 60 N.

Figure 3.32 and Figure 3.33 show that the minimum OFT in the contact area increases on the both GG and LDS liners when increasing the sliding speed. In the inlet area, the leading edge of the oil-filled zone can be seen, most clearly at low speeds. With increasing velocity, the leading edge comes closer to the conjunctural region, that is, the load-carrying zone becomes narrower, which causes an increase in local film pressure.

In Figure 3.32b at 5 m/s, ahead of the leading edge, blobs of oil adhering to the face of the PRS are most clearly observed. The movement of features such as that labeled by the white arrows in the image sequence of Figure 3.34a suggests that this oil flows in the direction opposite to the liner's sliding direction (reverse oil flow). The effect might be explained by the results of Shahmohamadi et al. [28]. They calculated the velocity flow field in the inlet wedge using CFD model and the result showed the recirculating oil flow and stagnation point as depicted in Figure 3.34b. On the other hand, Wigger [18] speculated that the air boundary layer, just above the inlet oil film and in front of the leading edge, cannot pass through the closed oil film in the conjunctural area and thus a reverse airflow would occur. Its aerodynamic

3. Oil film thickness imaging on the metal cylinder liner

drag would pull oil out of the contact zone, and it then adheres to the PRS surface. In previous experiments illuminating only the oil film adhering to the liner (via total internal reflection) [18] and in the chapter 4.2.5, the reverse stream was not observed, which is consistent with the interpretation that this volume of oil is adhering to the PRS and not the liner as in Figure 3.34.

Figure 3.32 and Figure 3.33 show that in the outlet area, film breaks up into horizontal stripes, which is in agreement with previous studies [127] [157] [158] [159]. This is caused by cavitation between the PR/CL in the diverging section where the pressure drops below atmospheric level as depicted in Figure 3.35. According to Nouri et al. [160], the cavity formation and developments shows different stages. First, the cavitation starts separately in several nucleation spots and the initial cavities spread rapidly in fractal-like “fern” shape. After that, they extend over the entire cavitation area, developing “fissure cavities”. Finally, these evolve quickly into more stable “string” type cavities, which were detected everywhere in the outlet region in Figure 3.32 and Figure 3.33.

Each vertical column at the same sliding speed shows the effect of increasing the normal load from 10 N to 60 N. The minimum OFT in the contact area decreases, but much more so on the GG than on the LDS liner. This will be discussed in more detail in section 3.2.3.

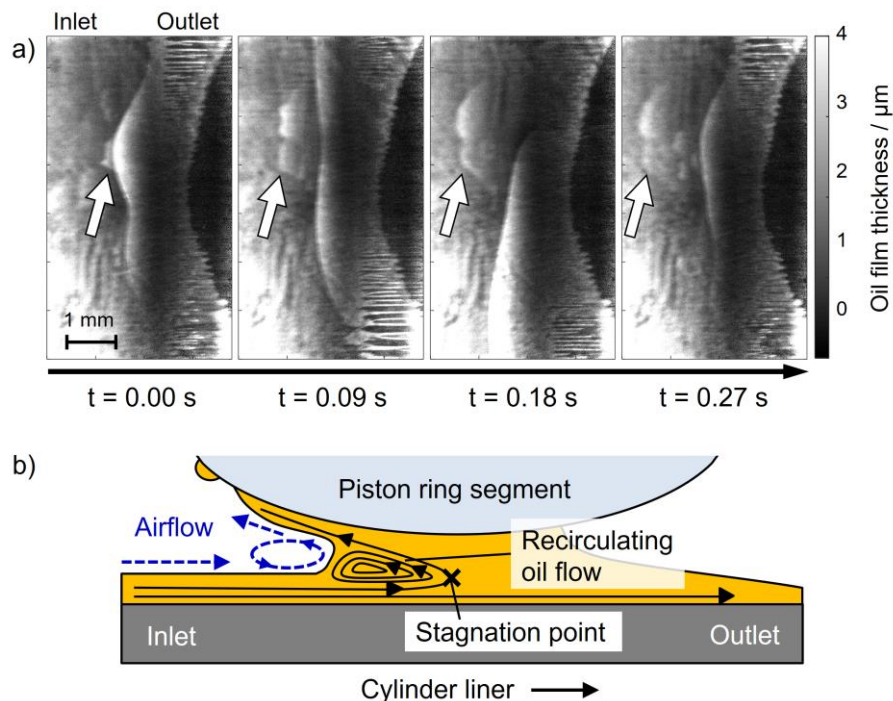


Figure 3.34: a) Snapshots from a sequence of rotations (GG liner, $T = 80$ °C, $F_N = 30$ N, $v = 3$ m/s). The white arrows point to the evolution of a feature discussed in the text. b) Schematic representation of the “reverse oil stream” phenomenon. Schematic recirculating flow in the oil film in the inlet region, a stagnation point according to Shahmohamadi et al. [161], and oil transport against the sliding direction by the reverse airflow according to Wigger [18].

3. Oil film thickness imaging on the metal cylinder liner

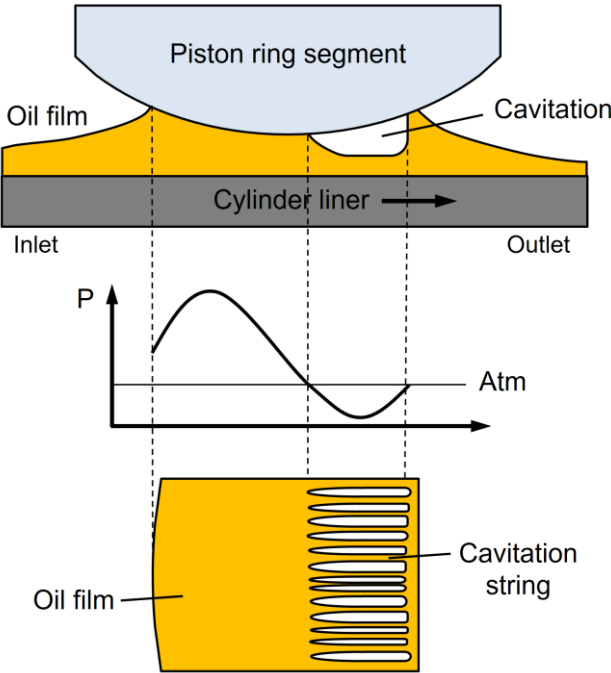


Figure 3.35: Schematic representation of the cavitation string phenomenon in the outlet region and corresponding pressure distribution.

3.2.3 Minimum oil film thickness compared to the Stribeck curve

Figure 3.36 (top row) shows the minimum OFT in the PR/CL contact along the increasing sliding speed and (bottom row) the corresponding Stribeck-type curves. Both uncorrected and stray light corrected OFTs are presented. The two different cylinder liners were compared and the normal load was varied from 10 to 60 N. Each data point in Figure 3.36 (top row) shows the mean value of 20 single images. Error bars indicate the standard deviation over the 20 images. The evaluation area is indicated by the dashed box in Figure 3.32 and Figure 3.33.

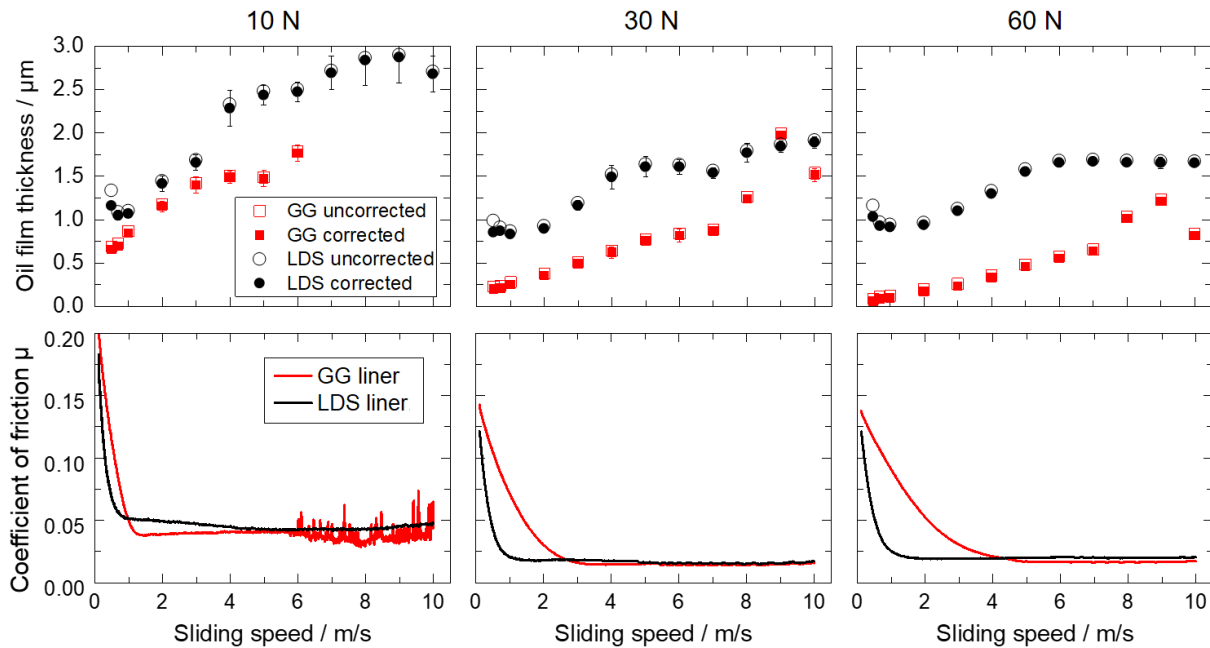


Figure 3.36: Minimum OFT on the two liners in the PR/CL contact area with increasing sliding speed (top) and the corresponding Stribeck-type curves (lubricant dynamic viscosity at 80 °C = 10.02 mPa*s) (bottom).

The OFT has an overall increasing trend with increasing sliding speed up to 10 m/s. This trend is more pronounced at lower loads. For the GG liner, at high sliding speeds (higher than 6 m/s at 10 N, and higher than 7 m/s at 30 and 60 N), the oil film is destabilized and fluctuates. Especially at 10 N this causes implausible OFT and the corresponding values were omitted in the plots. This instability is also observed in the corresponding Stribeck curve at the same sliding speed region after about 6 m/s. The oil film on the LDS liner was unstable as well at 10 N after 3 m/s, showing large fluctuations in the film thickness. A slight liner eccentricity might be responsible for this instability. In the case of the LDS liner, the data at the lowest sliding speeds show slightly thicker films than those at the next higher sliding speeds. This might be due to the inaccuracies of the stray light correction as discussed above. At every normal load, the OFT on the LDS liner is thicker than that on the GG liner (with the only exception at 30 N, 9 m/s due to the high OFT from the unstable film). Also, when increasing the normal load, the minimum OFT decreases and thus the mixed regime becomes more dominant in Stribeck

3. Oil film thickness imaging on the metal cylinder liner

curves. However, the OFT decreases less when increasing the normal load with the LDS liner than with the GG liner. We can now see quantitatively that with increasing load the minimum OFT on the LDS liner is almost constant between 30 and 60 N.

As shown in Figure 3.37 and discussed by Shen [109], the difference in film thickness between the two liners could be caused by the micro-reservoir system that the pores constitute. Relatively little-connected pores on the LDS liner surface can retain the oil inside. This is expected to create an additional hydrodynamic pressure to support the load, like tiny hydrodynamic bearings. Thus, the effect can cause a thicker oil film and less asperity contact. Whereas the rougher honing of the GG liner yields interconnected grooves, and the lubricant oil cannot be locally stored under the pressure of the PRS and may be pushed ahead of it within the grooves. This can lead to contact between the piston ring and liner and therefore, a mixed lubrication regime may become more dominant in the case of the GG liner with its interconnected texture.

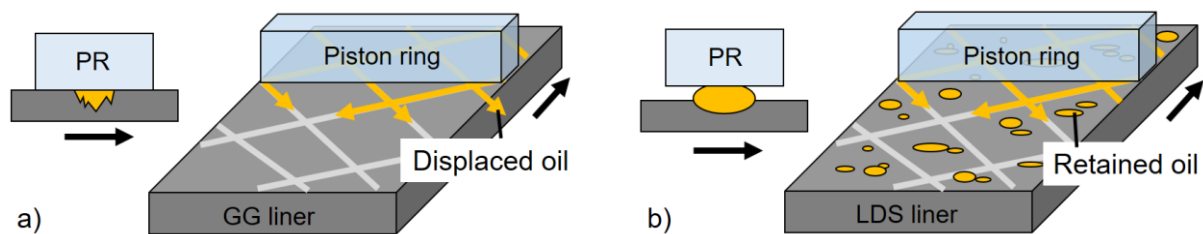


Figure 3.37: Schematic representation of the speculated oil behavior on the a) GG liner with displaced oil in the interconnected, open grooves and b) LDS liner with retained oil in the pores generating additional hydrodynamic pressure to support the load.

A comparison of unconnected and interconnected surface features by zum Gahr et al. [107] also showed larger OFT and an earlier transition to the hydrodynamic regime for the unconnected features. This is also consistent with in the Stribeck curves in Figure 3.36Figure 3.32, bottom row. The pores on the LDS liner surface have a benefit for friction reduction at high loads and low sliding speeds by an earlier transition between the mixed and hydrodynamic regime. On the other hand, the pores do not have an advantage in friction when the oil film on the GG liner is also in the hydrodynamic regime at high sliding speeds. In this regime, the Stribeck curves show similar friction coefficients with both liners, even though the oil film on the LDS liner is thicker than on the GG liner.

3.3 Chapter conclusions

Via LIF through a sapphire piston ring segment and a periscope-like mirror arrangement in a rotational tribometer, the OFT on a production cylinder liner was imaged with high resolution. The influence of load, sliding speed, and liner surface structure on the oil film and its minimum thickness within the contact area was studied. The effect of the stray fluorescence light from the surrounding oil, which can cause a positive bias on the minimum OFT, was investigated as well. Key observations are:

- With increasing sliding speed, the leading edge of the oil-filled zone at the inlet area came closer to the contact area and the minimum OFT generally increased.
- A “reverse oil stream” in the inlet region as well as a cavitation pattern due to the pressure drop in the outlet region was observed.
- With increasing normal load, the minimum OFT decreased, and the mixed regime became more dominant in the Stribeck curves.
- The minimum OFT on the LDS liner was overall thicker than that on the GG liner. The LDS liner showed better friction performance especially at high loads and low sliding speeds. When increasing the load from 30 to 60 N, the OFT on the GG liner decreased severely, but that on the LDS liner was nearly constant. The corresponding Stribeck curves also showed an earlier transition between the mixed and hydrodynamic regime with the LDS liner. Presumably, the unconnected pores on the LDS liner act as micro-reservoir system to generate additional hydrodynamic pressure under the high load.

4 Oil film around a cylindrical micropore visualized by fluorescence microscopy

The chapter presents the oil film near a single surface texture (micropore) in an optically accessible sliding contact reproducing the piston-ring/cylinder-liner contact in an engine. The LIF results show that the pore carries oil to the starved outlet, creating a downstream “oil tail”, whose morphology and volume are analyzed. Specifically, at low speed, the pore has a wider tail containing a higher oil volume than at high speeds.

Some parts of this chapter were published as “Cheong J, Wigger S, Fűßer H-J, Kaiser S. The oil film around a cylindrical micropore in a sliding contact visualized by fluorescence microscopy on a tribometer. *Tribol Int* 2022; 165: 107309”. Additional results are presented in sections 4.2.5 and 4.3. I designed the surface textures, performed the LIF experiments, post-processed, visualized and evaluated the results of the LIF data, wrote the original draft and reviewed it. I redesigned the experimental apparatus supervising the student theses, “Florian Botzenhart, Entwicklung einer Kalibriervorrichtung für ein Rotations-Reibverschleiß-Tribometer, Bachelor’s thesis, 2019” and “Erkan Akbas, Adaption eines hochauflösenden optischen Messsystems an ein Kolbenring-Tribometer, Master’s thesis, 2019”.

4.1 Methods

4.1.1 90° rotated tribometer and redesign

In this chapter, the RRV tribometer is employed as modified for optical access by Wigger [18], where the conventional metal liner in the initial setup (see Figure 3.1) is substituted with a quartz one as shown in Figure 4.1.

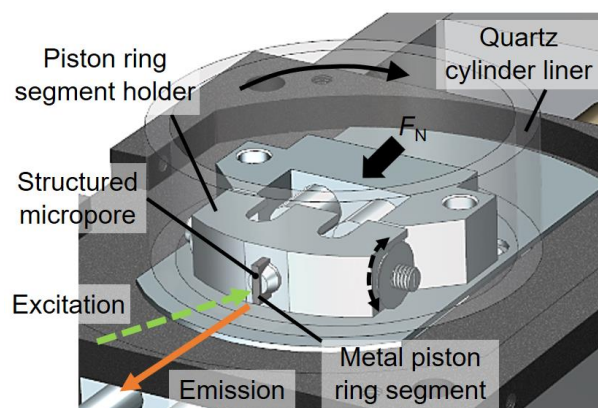


Figure 4.1: Optical RRV tribometer which substitutes the conventional metal liner in the initial setup with a quartz one.

4. Oil film around a cylindrical micropore visualized by fluorescence microscopy

As described in more detail below, single micropores were laser-textured onto the inside of the rotating quartz-glass liner with enough distance, representing a single feature in the porosity on an LDS liner with an arc-wire spray coating.

Figure 4.2a shows the tribometer and optic setup in chapter 3. With this setup, the mirror had to be installed on the post to redirect the light, since the post in the tribometer was in the way of directly illuminating the optical access. It also did not allow a shorter working distance than 410 mm. However, an adoption of a long-distance microscope required a working distance of 97-122 mm for a high magnification. For this purpose, the PRS and its relevant parts were 90 ° rotated as shown in Figure 4.2b. The camera could be then positioned directly opposite the PR/CL contact without the redirection mirror to detect the fluorescence signal. In order to avoid the damage of the microscope lens, the laser light entered the region of interest not coaxially, but at an angle of about 20 ° with respect to the surface normal. The rest of the reflected laser beam was absorbed by the beam dump for safety. With this reconstruction, the working distance of 122 mm could be achieved, which is enough for the required condition of the microscope lens.

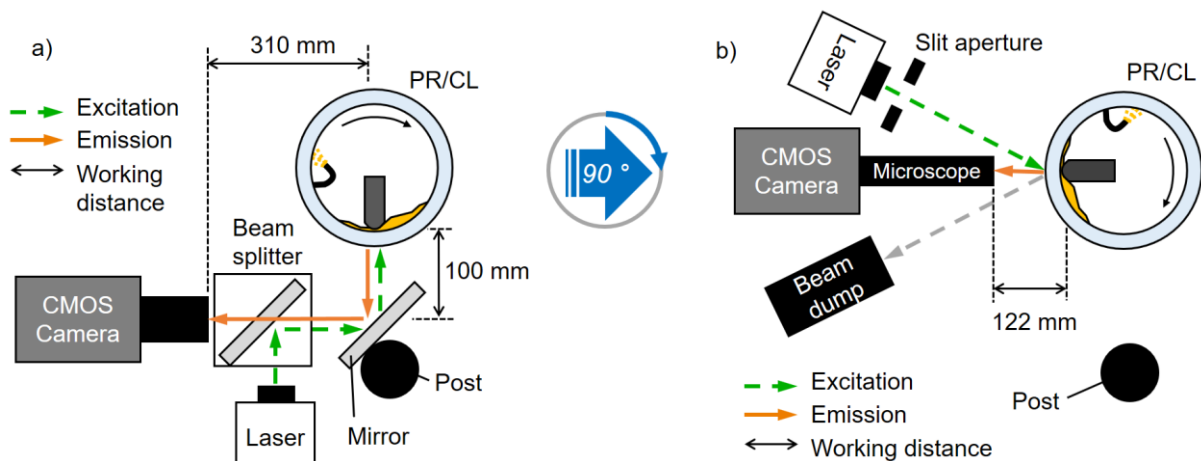


Figure 4.2: a) Schematic design of the RRV tribometer setup in chapter 3 with the redirection mirror on the post and longer working distance. b) Schematic design of the 90 ° rotated RRV tribometer setup without the redirection mirror and shorter working distance.

In Figure 4.3, CAD models of the previous- and 90 ° rotated tribometer are shown. The redesign and the adjustment procedures are described in more details in the appendix A.

4. Oil film around a cylindrical micropore visualized by fluorescence microscopy

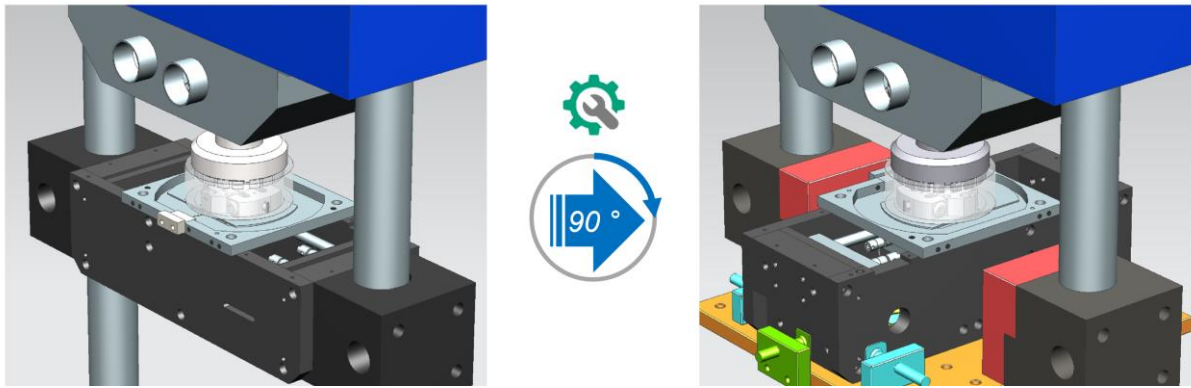


Figure 4.3: CAD model of the previous RRV tribometer setup (left) and 90 ° rotated RRV tribometer setup with newly designed supplemental parts (right).

4.1.2 Contact surfaces

Laser surface texturing was carried out on the polished inside surface of the quartz liner by the Institute of Advanced Materials at the Karlsruhe Institute of Technology. This created micro-size cylindrical pockets (pores) with a controlled topology, that is, with given diameter and depth. On the liner, the pores were spaced at least 90° in rotational angle apart as shown in Figure 4.4.

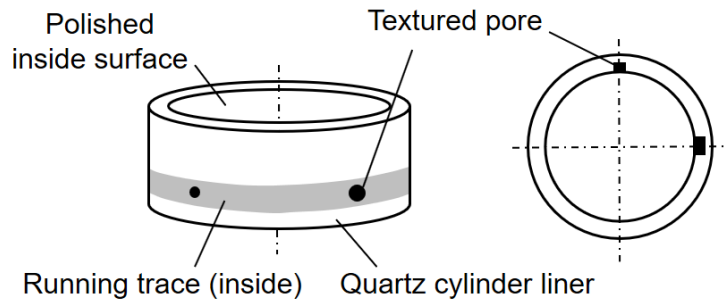


Figure 4.4: Schematic sketch of the pore-textured quartz cylinder liner.

Figure 4.5 shows their topographies measured by confocal microscopy (μ Surf, Nanofocus®). Two pore diameters (D) were examined, 200 and 500 μm , each with a depth (h) of about 40 μm . The smaller pore represents those found on an LDS liner as shown in the previous chapter 3, while the larger one is exaggerated in size and intended to provide a generic comparison. Also, a variation in depth was considered with $h = 2, 20, 40,$ and 80 μm , all with a diameter of 200 μm . The pores in Figure 4.5a and b were on the same liner while those in Figure 4.5c-e were on another liner.

A photograph of a PRS is shown in Figure 4.6 (left). The segment has a radius of 20 mm on the contacting side, a typical top piston ring's width of 2 mm, and a height of 10 mm. The contact surface is coated with diamond-like carbon (DLC), like many conventional top piston rings in an IC engine, and is essentially polished. Figure 4.6 (right) shows a surface topography of the PRS measured by confocal microscopy. The red rectangle indicates the field of view (FOV) in the fluorescence microscopy described next.

4. Oil film around a cylindrical micropore visualized by fluorescence microscopy

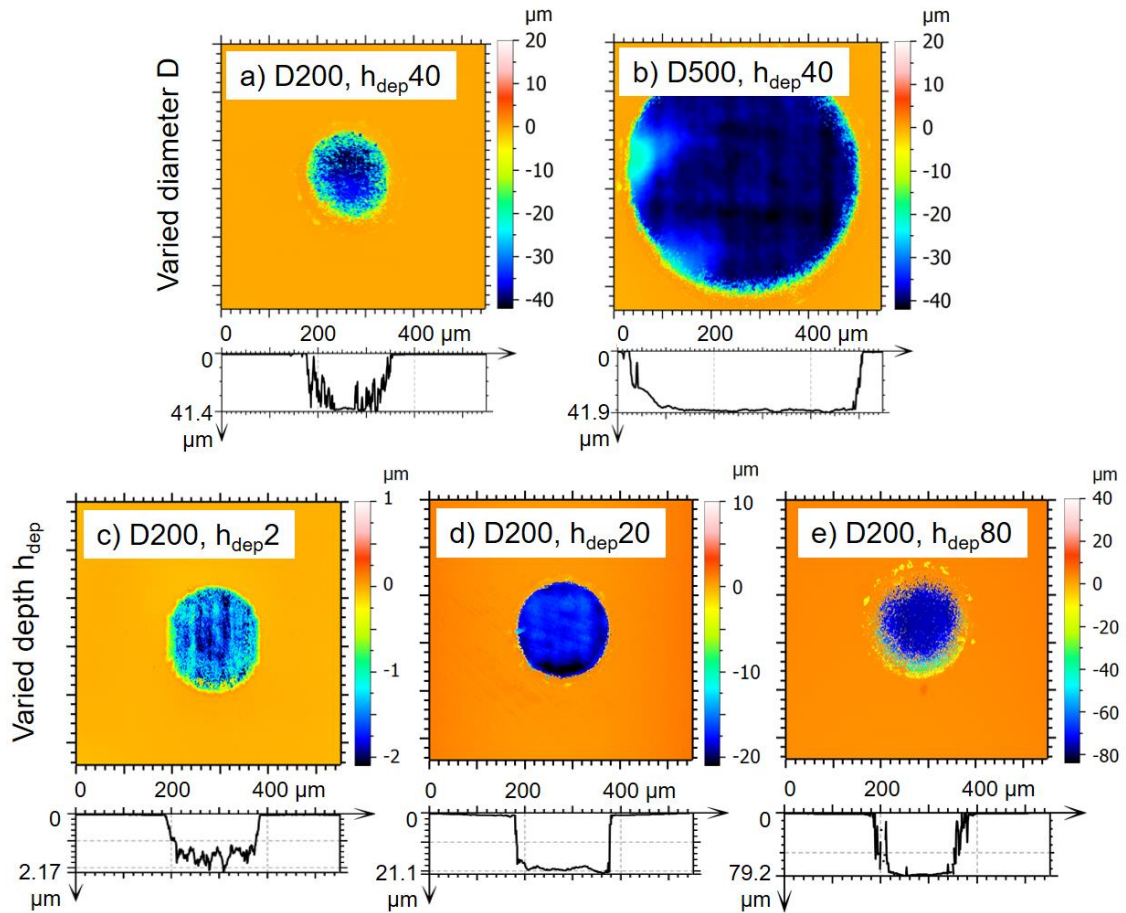


Figure 4.5: Surface topography of the pores measured by confocal microscopy with nominal diameter (D) and depth (h_{dep}) indicated. Each bottom graph shows a horizontal scan intersecting the pore's center. Note that the color scales and the depth scales vary between the sub-figures.

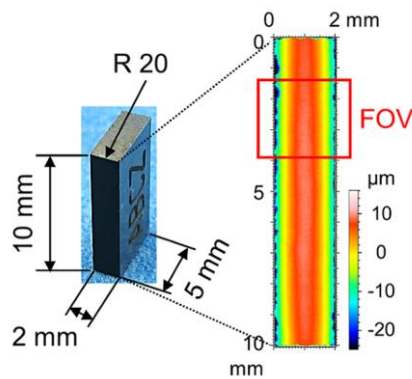


Figure 4.6: Photo of the metal piston ring segment (left) and its DLC-coated surface topography with the field of view (FOV) (right).

4.1.3 Experimental parameters and procedures

Load and speed in the tribometer were set based on the values encountered in a typical passenger-car sized IC engine, as described in chapter 3.1.4. Since this work focuses on the

effect of the porosity near the piston reversal points, the experiments are performed at low sliding speeds, from 0.1 to 4 m/s. Normal loads (F_N) are set to 10 and 30 N. 0W-20 “first fill” engine oil is sprayed onto the inside of the liner with a flow of 0.1 mm^3 per rotation at room temperature ($24 \text{ }^\circ\text{C}$) with a kinematic viscosity of about $73 \text{ mm}^2/\text{s}$. Figure 4.7 shows a Stribeck-type curve measured in the tribometer using these operating parameters. It shows that the mixed regime is up to about 0.3 m/s at 10 N and 0.5 m/s at 30 N.

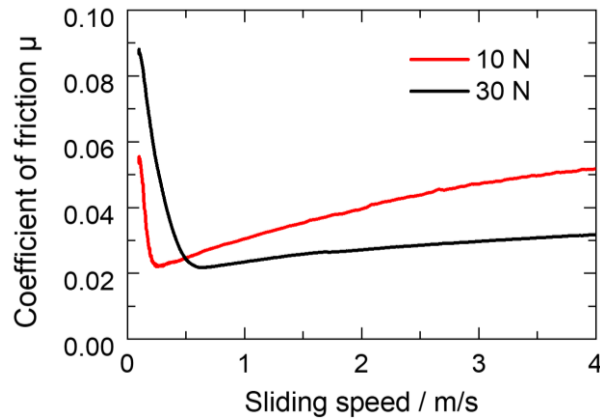


Figure 4.7: Stribeck-type curves with a quartz liner and a metal piston ring segment for two different loads.

4.1.4 Image acquisition

In order to image the micro-size pore with a useful magnification and working distance, a refractive long-distance microscope from Infinity Co. (USA), was used (Figure 4.8).

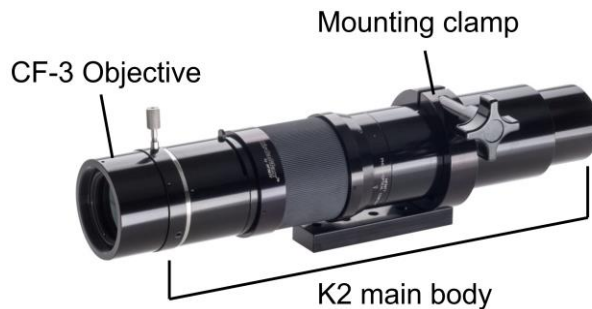


Figure 4.8: Long-distance microscope, model K2 DistaMax from Infinity Co. (USA).

The combination of K2 DistaMax and CF-3 objective (CF: close focus) allows a maximum working distance of 122 mm. In order to achieve a higher magnification while maintaining the working distance, a 2x teleconverter was mounted as well. The overall optic setup including the long-distance microscope is shown in Figure 4.9 and Figure 4.10 .

4. Oil film around a cylindrical micropore visualized by fluorescence microscopy

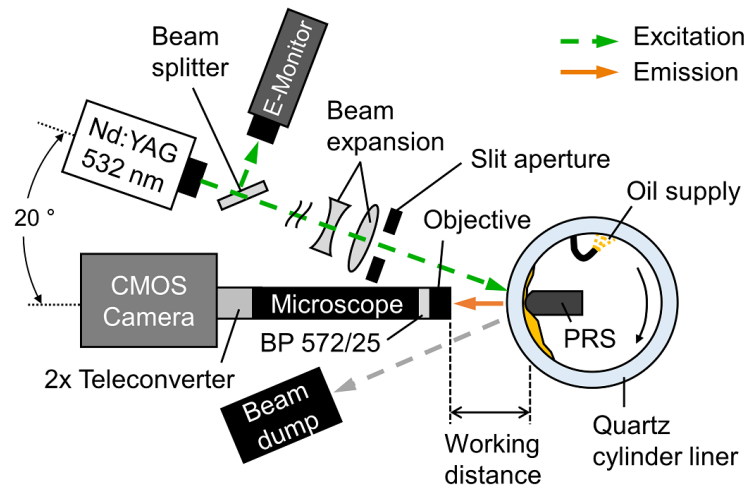


Figure 4.9: Plan view of the optical path layout with RRV tribometer, laser, camera, long-distance fluorescence microscope and working distance.

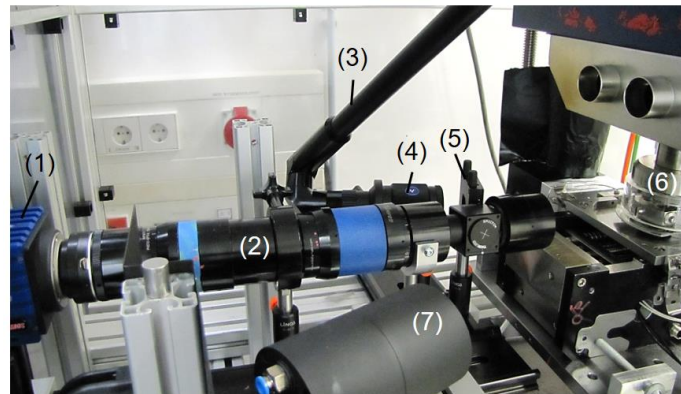


Figure 4.10: Photo of the optic setup. (1) CMOS camera, (2) long-distance microscope, (3) laser guiding arm, (4) laser beam expansion, (5) slit aperture, (6) PR/CL assembly and (7) beam dump.

In this chapter 4, the basic optical system (laser, dye, filter, camera, phase coupling) follows that in chapter 3 as already described in chapter 3.1.5. As shown in Figure 4.9, the excited laser beam at 532 nm with a laser fluence of about 13 mJ/cm^2 and about 10 ns pulse duration is partly reflected to an energy monitor to correct shot-to-shot energy fluctuations, and the remainder is guided to the experiment and formatted to illuminate only the PRS. Light enters the liner at an angle of about 20° with respect to the central axis of the microscope. The dye in the oil absorbs part of the laser light and emits red-shifted fluorescence. The fluorescence passes through the quartz liner and is imaged on a CMOS camera (LaVision Imager sCMOS) by a long-distance microscope (Infinity K2) with the objective lens CF-3 [162]. The working distance from the front face of the lens to the oil film is about 120 mm. A band-pass (BP) filter with a center wavelength of 572 nm and a full width at half-maximum bandwidth of 25 nm suppresses scattered laser light. A rotary encoder synchronizes the optical system with the liner's rotational angle for stroboscopic illumination. At a given angle, series of 20 images are

recorded. Successively incrementing that image acquisition angle allows assembling pseudo-time series of the pore passing through the contact zone. The pixel size is calculated with the same method used for Figure 3.21 and is $1.28 \mu\text{m}/\text{pixel}$. The corresponding image magnification is 5.1 with the 2x teleconverter.

Image resolution test with MTF (modulation transfer function)

In order to analyze the performance of optical systems, the modulation transfer function (MTF) is commonly used. The MTF is a measurement of its ability to transfer contrast at a particular resolution from the object to the image. In other words, MTF is a way to incorporate resolution and contrast into a single specification. Among many different methods to measure the MTF, a slanted-edge method specified in ISO Standard 12233 [163] measures the MTF of a digital image acquisition device by analyzing the image data of a simple knife-edge target captured by the device. The estimated MTF is not multidirectional, that is a function of the horizontal or vertical spatial frequencies [164]. In this work, a high precision stainless-steel foil, which has a sharp edge, is placed between the PRS and the quartz cylinder liner at a standstill. The oil/dye mixture is filled in a wedge-like gap and the slightly tilted PRS is loaded against the liner. This in-situ MTF measurement procedure is basically same as the in-situ absolute calibration method suggested in Figure 4.13a. The only difference is the angle of the slanted and placed precision foil that is larger than 0° . The precision foil is placed in both orthogonal directions as shown in Figure 4.11a and c. Scott et al. [165] and Jones [166] argued that the edge slanting is to obtain phase offsets in different cross-sections of the same edge. These phase offsets are used to calculate an oversampled edge profile, allowing for detection of frequencies near and above Nyquist. Thus, the slant angle is enough when it passes across a minimum number of sampling pixels to obtain the phase offset. In general, a slant angle of about 5° is often used [167]. However, in this work, it was not possible to capture an image with an edge close to 5° , since the inserting and positioning of the small piece of the precision foil on the PRS was challenging. As a result, larger slant angles than the typical ones were adopted as shown in Figure 4.11a and c.

4. Oil film around a cylindrical micropore visualized by fluorescence microscopy

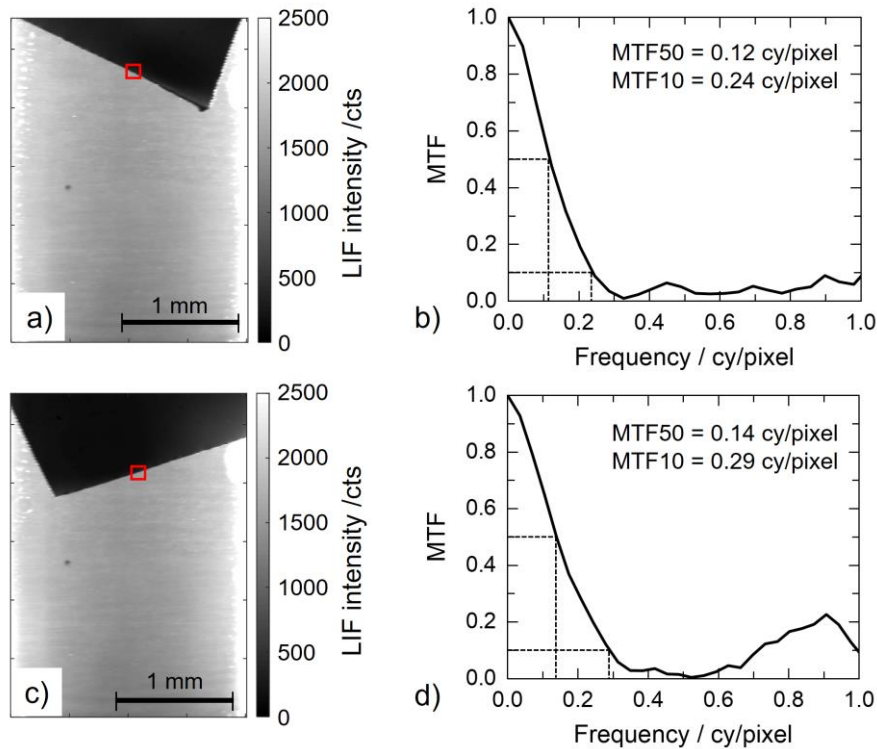


Figure 4.11: In-situ MTF analysis using slanted-edge method in orthogonal directions. a) LIF image with the first direction of the precision foil. b) MTF curve from the red box in a. c) LIF image with the second direction of the precision foil. d) MTF curve from the red box in c.

Each LIF image used for the MTF analysis (Figure 4.11a and c) was the ensemble average of 100 single shots, background- and flat-field corrected. The analysis was performed in an open-source code [168] via Matlab. On the images, a small region (red box), which covers the slanted edge and near the lateral center, was selected for the MTF analysis. The latter condition allowed choosing an area that the oil/dye possibly did not exist between the liner-foil-barrel shaped PRS while being loaded (see Figure 4.13b). The size of the selected region was about 30×25 pixels. The computed MTF results are shown in Figure 4.11b and d; each MTF50 value (the frequency, where MTF is equal to 50 %) was calculated as 0.12 cycle per pixel (cy/pixel) for the first slanted direction and 0.14 cy/pixel for another direction. In addition, the frequency associated with the 10 % MTF response point (MTF10) can be understood as a limiting resolution of an optical system [163]. In this work, we obtained the first direction's MTF10 value of 0.24 cy/pixel that is a spatial resolution limit of $5.3 \mu\text{m}$ to distinguish a pair of white/black lines ($5.3 \mu\text{m}/\text{cy}$), since the pixel size is $1.28 \mu\text{m}/\text{pixel}$ (chapter 4.1.4). The other direction showed the MTF10 of 0.29 cy/pixel, which is equivalent to $4.3 \mu\text{m}$ spatial resolution limit. The region (red box) for the MTF analysis was determined by the visual inspection and the repeatability of the region selection caused about 2.7 % inaccuracy over three individual selections for the MTF 50 value.

4.1.5 Image processing

As discussed in chapter 3.1.7, the OFT is calculated from the recorded raw LIF image I_S via equation (3.2). This section focuses on additional aspects and modifications relevant for the chapter 4: the specific method for obtaining the “flat field”, the absolute OFT calibration, morphological image processing to extract relevant image features, and an assessment of inaccuracies caused by the inevitable strong stray light.

Flat-field correction

The flat-field correction accounts for inhomogeneity of the instrument sensitivity across the image. Figure 4.12 shows the flat-field image acquisition. An oil bath of 20 mm depth is attached to the inner side of the quartz liner with a silicon adhesive (Figure 4.12a and b).

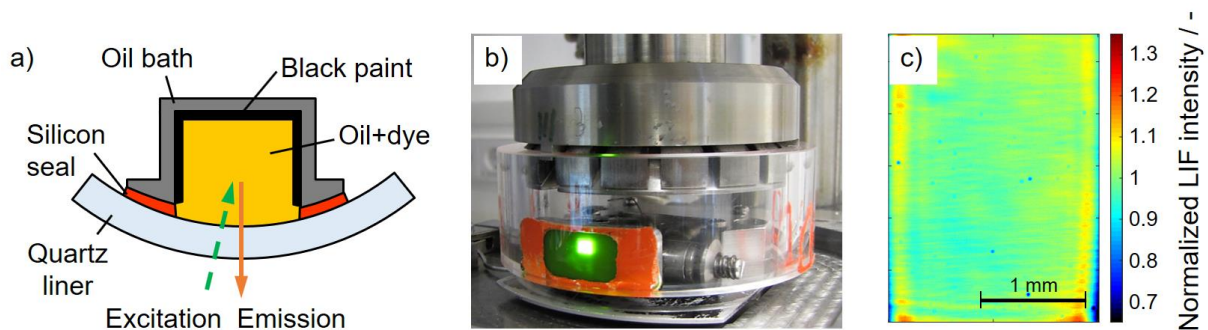


Figure 4.12: a) Schematic sketch and b) photo of the experiment for the flat-field acquisition. c) Flat-field image normalized with respect to its average intensity.

To ensure complete absorption, the dye concentration is here increased to 1.0 mmol/L. The laser energy is decreased to 30 % by an attenuator to keep the camera sensor from saturating, while minimizing the change in the spatial laser energy distribution (less than 3 % with respect to the full-energy one). For convenience, the recorded flat-field image is normalized with respect to its average intensity. This $\langle I_{FF, norm} \rangle$ is shown in Figure 4.12c. To assess the accuracy of the flat-field correction, averaged flat-field images from two individual recordings were divided by each other. This ratio image had a standard deviation of 2 % across the field of view. Fluctuations in the energy of the laser shots are removed based on the ratio of each shot's measured energy $e_{measured}$ to the reference energy e_{ref} . It then remains to calibrate the field-corrected images in absolute OFT.

Absolute calibration

Figure 4.13a shows the method used for that. A small piece of 20 μm thick precision shim foil was inserted near the top end of the PRS, the gap between the PRS and liner was filled with oil/dye mixture, and the PRS is slightly pressed against the liner. Because of the pivot point in the PRS holder (see Figure 4.1), the PRS can tilt and create a wedge-like gap whose background and flat-field corrected LIF image is shown in Figure 4.13b.

4. Oil film around a cylindrical micropore visualized by fluorescence microscopy

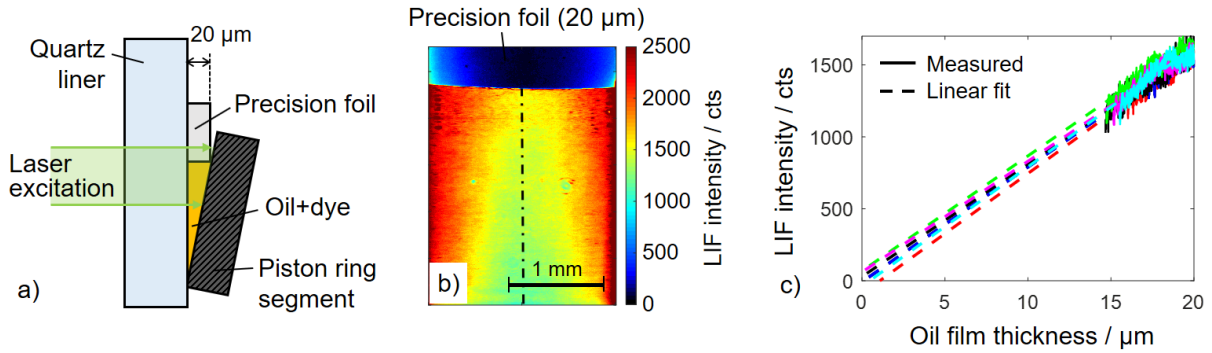


Figure 4.13: a) Schematic sketch of the in-situ absolute calibration. b) LIF image from the absolute calibration experiment. c) Relationship between the measured LIF intensity (solid line) and the theoretical OFT. The slope of the linear fit (dashed line) corresponds to the calibration factor.

The LIF intensity was plotted against the computed gap height (i.e., OFT) along the center line indicated in Figure 4.13b. At the high magnification used here, only the area near the top end of the PRS was imaged. Six individual measurements were carried out. The results are shown in Figure 4.13c and Table 4.1.

Table 4.1: Measured calibration factors (t_{cal}) from the measurements in Figure 4.13c.

Remeasurement	Slope (t_{cal}) / cts/μm	Offset / cts
1	83.5	-89.7
2	79.8	-7.5
3	78.3	28.6
4	80.0	68.0
5	77.0	60.4
6	83.0	-38.4
Average	80.3 cts/μm	3.6 cts
Standard deviation	3.2 %	61.0 cts

In Figure 4.13c, each data series (solid line) was least-squares fitted with a linear function (dashed line), yielding a slope that is the calibration factor t_{cal} . The average is $t_{cal} = 80.3$ cts/μm. The standard deviation over the repeated measurements is 3.2 %. The average offset in LIF intensity is 3.6 cts, which corresponds to 0.04 μm, with a standard deviation of 61.0 cts, or about 0.8 μm.

Oil tail segmentation and net volume calculation

Figure 4.14a shows a typical LIF image of the OFT in the PR/CL contact with a pore. As will be discussed in more detail in chapter 4.2, oil is sucked out of the pore due to the sub-ambient pressure in the diverging outlet region and deposited downstream, a phenomenon we call “oil

tail”. The oil tail means more oil is behind the pore than in the regions above and below it that are not influenced by the pore. To quantify this additional volume of oil – the “net oil tail volume” (nOTV) –, a combination of morphological and photometric image processing was employed. Figure 4.14 presents this post-processing with example images.

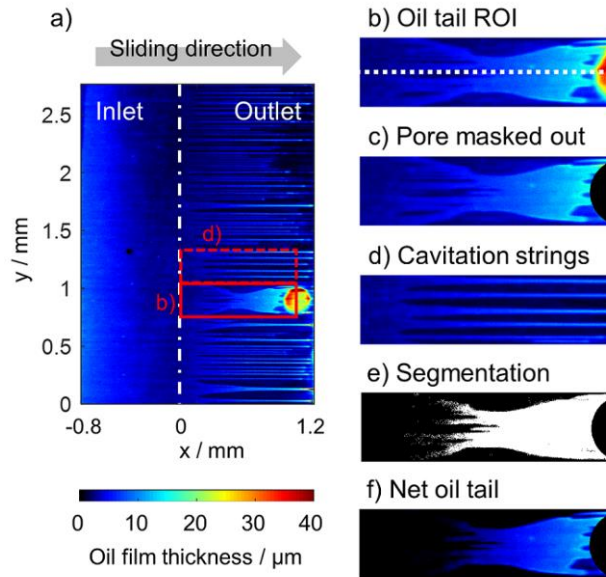


Figure 4.14: Image segmentation of the oil tail. a) Typical LIF image of the OFT in the PR/CL contact with a pore and the extracted oil tail, b) cropped region of interest including the entire oil tail, c) gross oil tail image with the pore masked out, d) example cavitation strings formed without pore, e) segmentation of the oil tail image, f) net oil tail image.

First, a small region of interest (ROI, red solid box in Figure 4.14a and Figure 4.14b) that includes the entire oil tail is selected by visual inspection. Horizontally (in x-direction), the ROI extends from the PR/CL gap minimum (dash-dotted line in Figure 4.14a) to where the oil tail emanates from the pore. Second, the edge of the pore and thereby the pore’s position is determined more accurately from the intensity along the horizontal ROI centerline indicated in Figure 4.14b (white dotted line). With the pore position and the known pore diameter, the image area corresponding to the pore itself can be masked out (Figure 4.14c). Since the bright fluorescence light scattered from oil in the pore causes a bright and falsely bigger pore boundary, the masks were chosen 50 μm larger in diameter than the pores. Third, the average OFT in ROIs directly above (as shown in Figure 4.14d) and below the pore is subtracted from Figure 4.14c. This accounts for the oil that would have been present without the pore. Next, a segmentation of the image isolates the oil tail from the background, as shown in Figure 4.14e. For that, a threshold is found based on clustering the pixel histogram into two Gaussian distributions as proposed by Bo et al. [169]. Figure 4.14f shows the resulting foreground image, from which the nOTV can be calculated by area-integration of the OFT multiplied with the projected pixel size ($1.28 \mu\text{m} \times 1.28 \mu\text{m}$). Similarly, the gross oil tail volume (gOTV) and a

corresponding cavitation string volume can be calculated by multiplying the foreground mask with Figure 4.14c and d, respectively.

4.1.6 Assessment of the stray light effect

Adjacent regions of high fluorescence intensity can falsely add signal to the region of interest [77] [154] [155]. This is termed “stray light effect” here. (Note that this is *fluorescence*. Stray light at the *laser wavelength*, i.e., elastic scattering, is completely blocked by the filter in front of the camera).

The oil gathered on the PRS holder and at both edges of the PRS (Figure 4.15a and Figure 4.16a, features labeled (i) and (ii)) can cause stray light due to its much greater thickness.

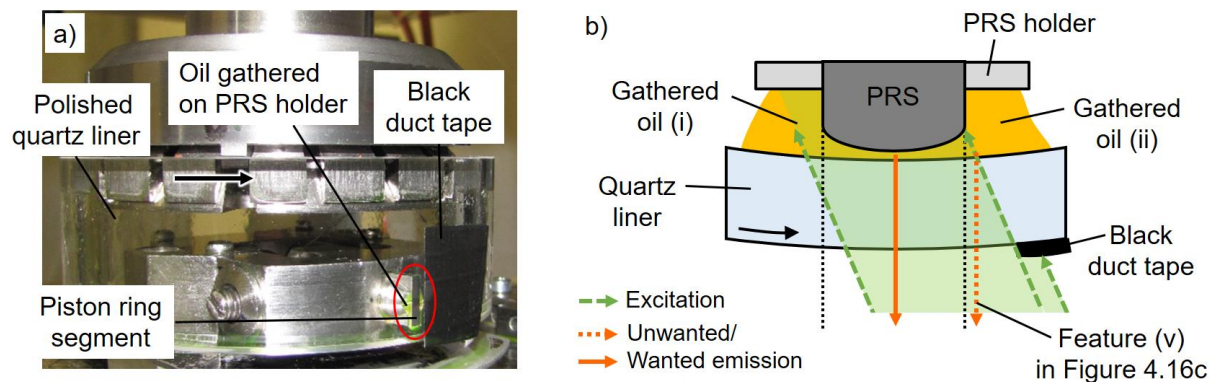


Figure 4.15: a) Photo of the in-situ stray light measurement using a black tape on the liner to block part of the laser beam. b) Schematic sketch of this measurement showing the unwanted residual emission remaining when the laser illuminating the oil gathered at (ii) is blocked.

We assessed the contribution from this stray light by shielding the two sides, i.e., the regions (i) and (ii), with black tape on the quartz liner in two separate experiments. This yields the images in Figure 4.16b and c, where the tape-covered regions are indicated by (iii). Despite the tape cover, some unwanted stray light was still detected, as shown in Figure 4.16b-(iv) and Figure 4.16c-(v). This is due to the non-coaxial illumination, as illustrated schematically in Figure 4.15b for the residual fluorescence feature labeled (v) in Figure 4.16c.

4. Oil film around a cylindrical micropore visualized by fluorescence microscopy

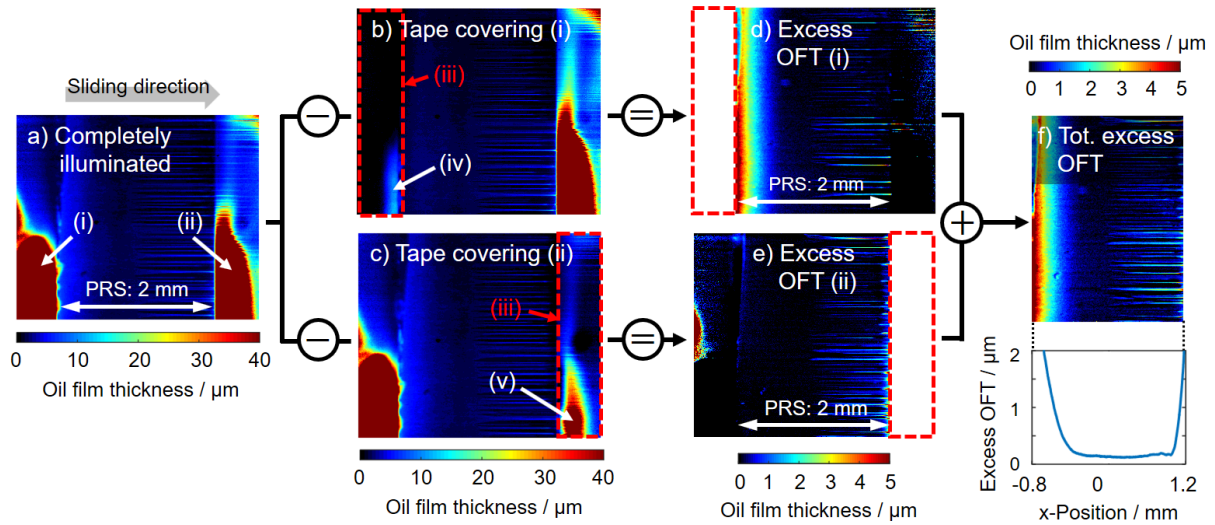


Figure 4.16: In-situ measurement of the stray light effect. a) None of the gathered oil is covered. b-c) The oil gathered at (i) or (ii) is shielded from laser illumination. d-e) OFT differences between a and b or a and c. Note that the color scale is different from that used in a-c. f) Total stray light effect by sum of d and e. Below the image is average profile along the x-axis. Sliding speed is 0.5 m/s and normal load is 10 N.

Nevertheless, this residual light is less than 10 % of that detected in the same region without the tape cover. Figure 4.16d and e show the result of subtracting these images from that with complete illumination. The sum of these, shown in Figure 4.16f, is an estimate of the total excess OFT due to stray light from both outer sides of the PRS. The vertical average of the excess OFT is shown in the line plot below the image in Figure 4.16f. According to that, the left-most 0.50 mm and the right-most 0.15 mm are considerably affected by stray light, while the region inside of these limits, which is of most interest for an analysis of the oil tail in the contact zone, has a systematic error in the OFT of about maximum +0.3 μm . In principle, it would be possible to correct for the stray light based on the results shown in Figure 4.16f, but in practice the oil accumulation upstream and downstream of the PRS varies, and with that the exact value of the bias introduced by the stray light also varies. We thus refrain from such a correction but use the insights from the stray light analysis to guard against possible errors in interpreting the OFT images.

4.2 Results

First, the results from the pores with 40 μm depth and 200 and 500 μm diameter are presented. The image timing, i.e., the position of the pore with respect to the PR/CL gap minimum, the sliding speed, and the load were varied for both pore diameters. In addition to a qualitative comparison of the images within each variation, the main quantitative metric of interest is the oil tail volume. For the variation in pore depth – 2, 20, 40, and 80 μm – at a diameter of 200 μm , only data at a single load and speed are considered.

4.2.1 Spatiotemporal evolution of the oil tail

Figure 4.17 presents the typical oil film behavior in and around a pore with diameters of 200 μm (top row) and 500 μm (bottom row) as it slides through the region under the PRS. Here, the sliding speed is 0.5 m/s and the normal load is 10 N. The liner with the pore moves from the left to the right. p indicates the pore position, i.e., the distance of the pore center from the PR/CL gap minimum.

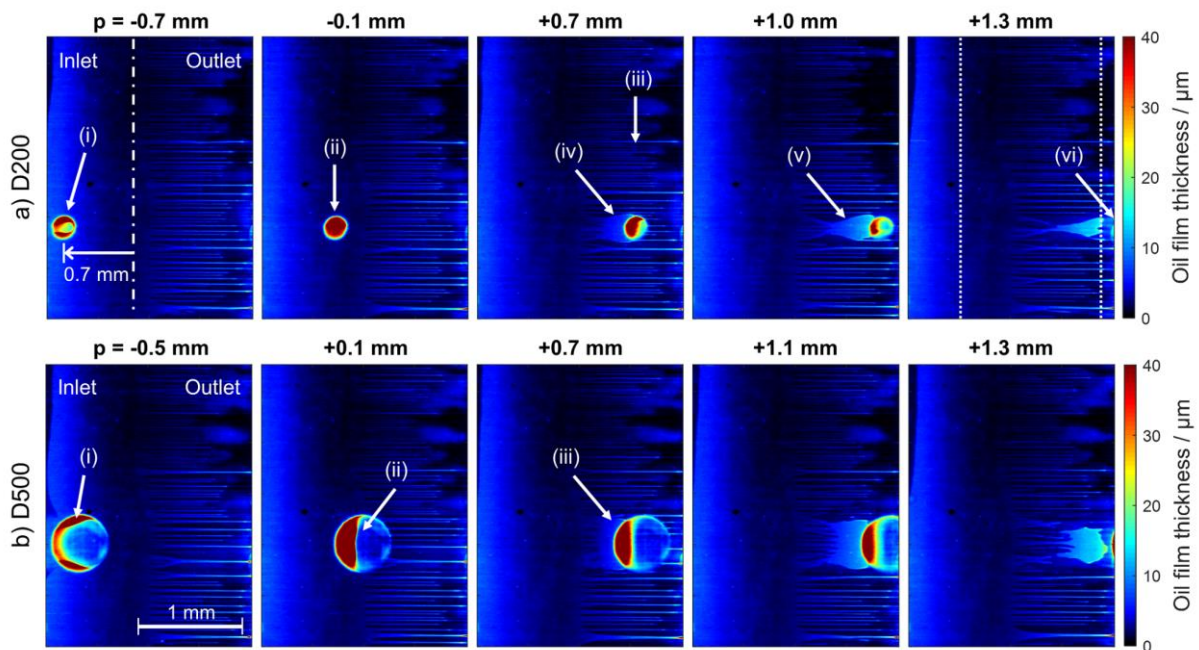


Figure 4.17: Spatiotemporal evolution of the oil tail. p indicates the pore position from the dash-dotted PR/CL gap minimum. The dotted lines in the top row's right-most image exemplarily indicate the regions near the PRS edge where the measurement accuracy is significantly reduced by stray light, as shown in Figure 4.16f. Sliding speed = 0.5 m/s, normal load = 10 N. Pore diameter \times depth = a) 200 \times 40 μm , b) 500 \times 40 μm .

The overall film behavior was discussed in the previous chapter 3. Here, with higher-resolution images available, we focus on the area near the pore. In the top row of Figure 4.17 the pore is 0.7 mm upstream of the PR/CL gap minimum ($p = -0.7$ mm) and just enters the region under the PRS. Oil is being drawn into the pore (i). This corresponds to the “inlet suction” mechanism

[98] [99]. The relative sliding motion of the surfaces yields a sub-ambient pressure in pores that are under the inlet edge, and more oil can be brought into the contact region than would be without the pores. At $p = -0.1$ mm, the pore almost reaches the minimum PR/CL gap (dash-dotted line). The entire pore is now fully filled with oil (ii), since the LIF-measured OFT inside the pore matches its depth (see Figure 4.5a). At $p = +0.7$ mm, the pore has left the contact area and enters the outlet region in the diverging PR/CL gap with its typical cavitation strings (iii). Oil is being extracted from the pore due to the pressure drop and deposited downstream of the pore in the form of an oil tail (iv). In this oil tail, the oil fully fills the space between the PR/CL surfaces. The streamwise pressure distribution in this situation has been simulated by Profito et al. [127]. More noticeable development of the oil tail (v) happens at $p = +1.0$ mm, and the pore is being emptied. We can now see more clearly that the tail tapers downstream and ends in a fan of cavitation strings. The contiguous full-film part of the tail does not reach all the way downstream to the minimum gap location anymore. In final image of this stroboscopic sequence, the pore has just left the region under the PRS (vi) at $p = +1.3$ mm (in the full FOV it is still visible, thus its center position can be precisely assigned). The oil tail is now separated from the pore. The white dotted lines in this image indicate the regions near the PRS edge where due to stray light the measurement is expected to significantly overestimate the OFT, as shown in Figure 4.16f. Conversely, inside these boundaries, the OFT – in particular that in the oil tail – can be quantified accurately. Fortuitously, the detachment of the oil tail from the pore as it leaves the region under the PRS means that very little of the oil tail is in this lower-accuracy region.

The bottom row in Figure 4.17 shows a sequence with a pore with a diameter of 500 μm . At $p = -0.5$ mm, the oil being dragged into the pore is seen collecting along the pore's edge (i). At $p = +0.1$ mm, the pore center is almost under the gap minimum, but apparently due to the pore's larger size it is not fully filled with the oil. The oil is accumulated in the pore in the opposite direction of the liner movement (ii) because of the shear. In the outlet region, the spatiotemporal evolution is qualitatively similar to that for the smaller pore in the top row. The oil tail develops (iii) until the pore leaves the region under the PRS. Compared to the case with 200 μm pore diameter, for 500 μm the absolute width of the oil tail is greater but its width relative to the pore diameter is less. We attribute this to the fact that in the converging zone the larger pore is not completely filled, such that subsequently the oil tail does not emanate from the pore's entire diameter but only from the smaller chord near the trailing edge of the pore.

4.2.2 Influence of sliding speed on the evolution of oil tail volume

Figure 4.18 presents the spatiotemporal evolution of the nOTV as a function of the pore position for a normal load of 10 N, varying the sliding speed and pore diameter. The slightly

4. Oil film around a cylindrical micropore visualized by fluorescence microscopy

different positions of the pore for each data point (determined from the images) stem from temporal jitter in the stroboscopic image acquisition.

For both pore diameters and all sliding speeds, with increasing pore position from the PR/CL gap minimum the nOTV first increases very little, but beyond about $p = +0.3$ mm the increase is much greater until the pore approaches the outlet edge of the PRS at $p = +1.2$ mm. Except for the last 0.1 or 0.2 mm before the PRS edge, the increase in volume for $p > +0.3$ mm is approximately linear in all data series. This corresponds to a constant volume flow out of the pore per sliding distance.

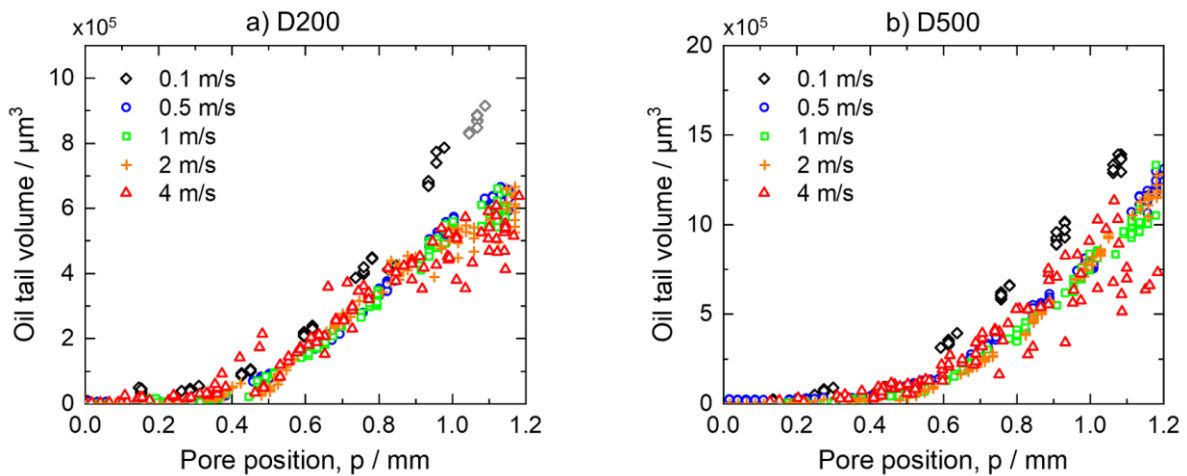


Figure 4.18: Spatiotemporal evolution of the net oil tail volume (nOTV) when the sliding speed is varied from 0.1 to 4 m/s. a) Pore diameter \times depth = $200 \times 40 \mu\text{m}$, b) $500 \times 40 \mu\text{m}$. Normal load = 10 N. Note that the scaling of the ordinate differs between a) and b).

We now consider the results for the two pore diameters in more detail, starting with the $200 \mu\text{m}$ pore (Figure 4.18a). Here, for sliding speeds between 0.5 and 4 m/s, the volume flow is similar with about 8×10^{-13} L/m, but at 0.1 m/s it is 12×10^{-13} L/m. The volume of the $200 \mu\text{m}$ pore is $7.5 \times 10^5 \mu\text{m}^3$ calculated from the topography shown in Figure 4.5a. However, for 0.1 m/s Figure 4.18a shows a group of (grey-colored) data points near $p = +1.1$ mm that are *above* that volume. This is physically implausible, since it implies that more oil came out of the pore than it could have held. In fact, for 0.1 m/s, the oil tail detaches from the pore very late (this can be seen in Figure 4.19), which means that some of it is in the near-edge region where stray light leads to an overestimation of the measured OFT. Nevertheless, the outflow from the pore at 0.1 m/s is significantly greater than at the higher speeds. At a normal load of 10 N, 0.1 m/s is in the mixed lubrication regime (see Figure 4.7). Based on results from numerical modelling, Profito et al. [127] argued that the mixed regime can generate higher hydrodynamic pressure in such a pore than the hydrodynamic regime. Since the pressure difference between the pore and the surrounding outlet region drives the oil extraction [75], this would be consistent with the greater oil tail volume for 0.1 m/s. On the other end of the speed range examined here, the

data for 4 m/s scatter much more than the lower-speed ones. This implies that the oil-tail formation is less stable at this speed.

For the 500 μm pore (Figure 4.18b), the general trends in sliding speed are the same: the nearly linear increase in nOTV is similar for all sliding speeds but significantly greater for 0.1 m/s, and the data scatter much more for 4 m/s than for the lower speeds. However, in the case of the larger pore, even the largest nOTV found in Figure 4.18b, $13 \times 10^5 \mu\text{m}^3$, is still much less than the pore volume of $70 \times 10^5 \mu\text{m}^3$. This is consistent with the images in Figure 4.17 that show that the pore is never fully filled. Finally, Figure 4.18b shows the linear trend in nOTV to continue all the way to $p = +1.2 \text{ mm}$, whereas Figure 4.18a shows a decrease in slope near the PRS edge. However, this is because even when the pore center has left the area under the PRS, for the larger pore, some parts of it are still under the PRS, and in particular in the region that shows positive bias in OFT due to stray light. Thus, the partial flattening of the data series towards the PRS edge seen for in Figure 4.18a is taken to be more accurate than the steeper continuation seen in Figure 4.18b. Finally, we note that the data for a normal load of 30 N (not shown here) are very similar to those for 10 N.

4.2.3 Influence of sliding speed and load

Figure 4.19 shows single-shot images of the oil film around a pore at a fixed pore position for variations in load, speed, and pore diameter. The horizontal width of each image is the entire width of the PRS. A pore position of $p = +1.0 \text{ mm}$ was selected since the oil tail is well-developed at this position, but not yet influenced much by the edge of the PRS.

4. Oil film around a cylindrical micropore visualized by fluorescence microscopy

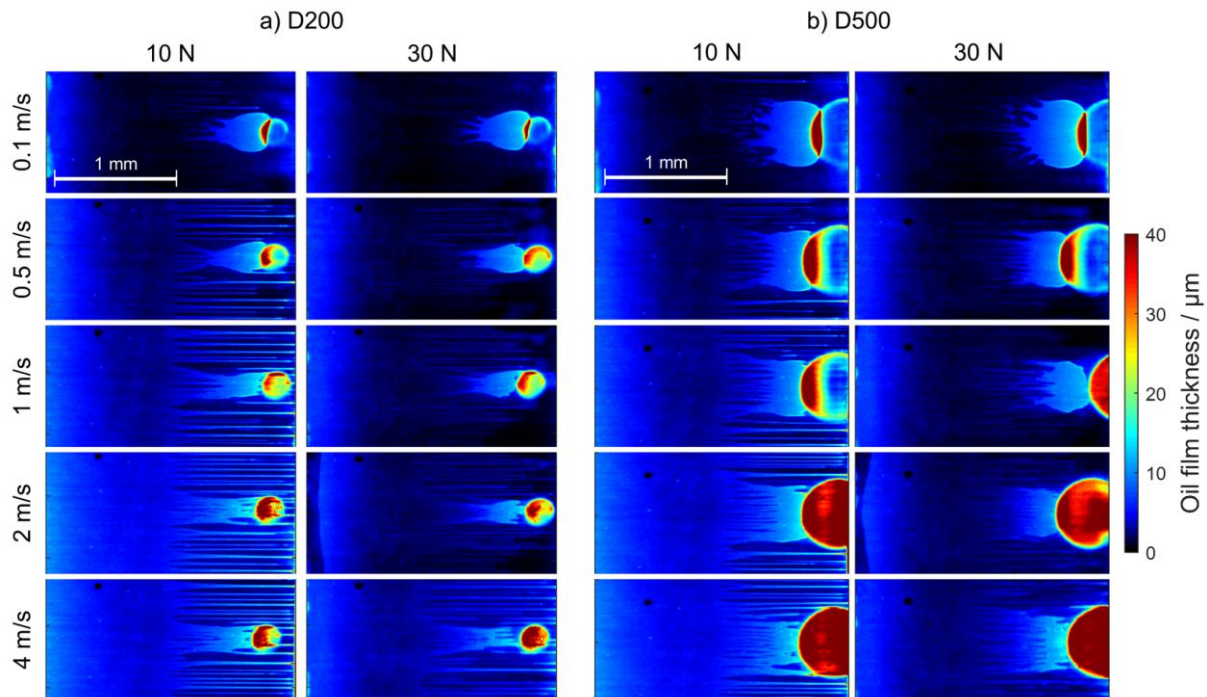


Figure 4.19: Cropped single shot images of the oil tail at about $p = +1.0$ mm with sliding speeds between 0.1 and 4 m/s. Normal load and pore sizes as indicated above each column. Pore depths are 40 μm .

Overall, the trends in the morphology of the oil tail as a function of sliding speed are similar for all combinations of load and speed. The oil tail is wider and less ruptured by cavitation at lower sliding speeds. The amount of oil remaining inside the pore increases with increasing speed. In particular for the lower load, 10 N, it is obvious that the oil film under the PRS is much thinner for 0.1 m/s than for the next faster speed, 0.5 m/s. This makes the oil tail visually stand out much more than at the higher speeds. The oil distribution inside the pore at 0.1 m/s also appears qualitatively different in that very little oil remains, and all of it is found near the trailing edge of the pore. The tail itself is wider than at faster speeds, while the OFT in the tail appears similar, which means that the marked difference in nOTV with sliding speed, quantified in Figure 4.18 and Figure 4.20, is due to the difference in lateral morphology. Concerning the influence of load on the oil tail, the detachment of the tail from the pore seen at higher speeds is slightly more pronounced at the higher load. Aside from that, there are only slight morphological differences between 10 and 30 N that can be discerned in these example single-shot images. However, for 30 N load, the oil film in the outlet region remains very thin up to 1 m/s speed, while at 10 N this is only the case for 0.1 m/s. In other words, the contact is more lubricant-starved at higher load. Thus, we can expect that the relative benefit from the pore distributing oil into the contact zone is greater in the case of 30 N.

Figure 4.20 plots the three oil volumes determined according to the procedure described in Section 4.1.5: gOTV (represented by the bar's total height), the volume in the cavitation strings in an area of the same size but vertically neighboring the oil tail (top section of the bar), and

4. Oil film around a cylindrical micropore visualized by fluorescence microscopy

nOTV (bottom section of the bar). The nOTV is the difference between cavitation-string volume and gOTV and should be equal to the volume extracted from the pore. Error bars indicate the standard deviation in nOTV across 20 single shots.

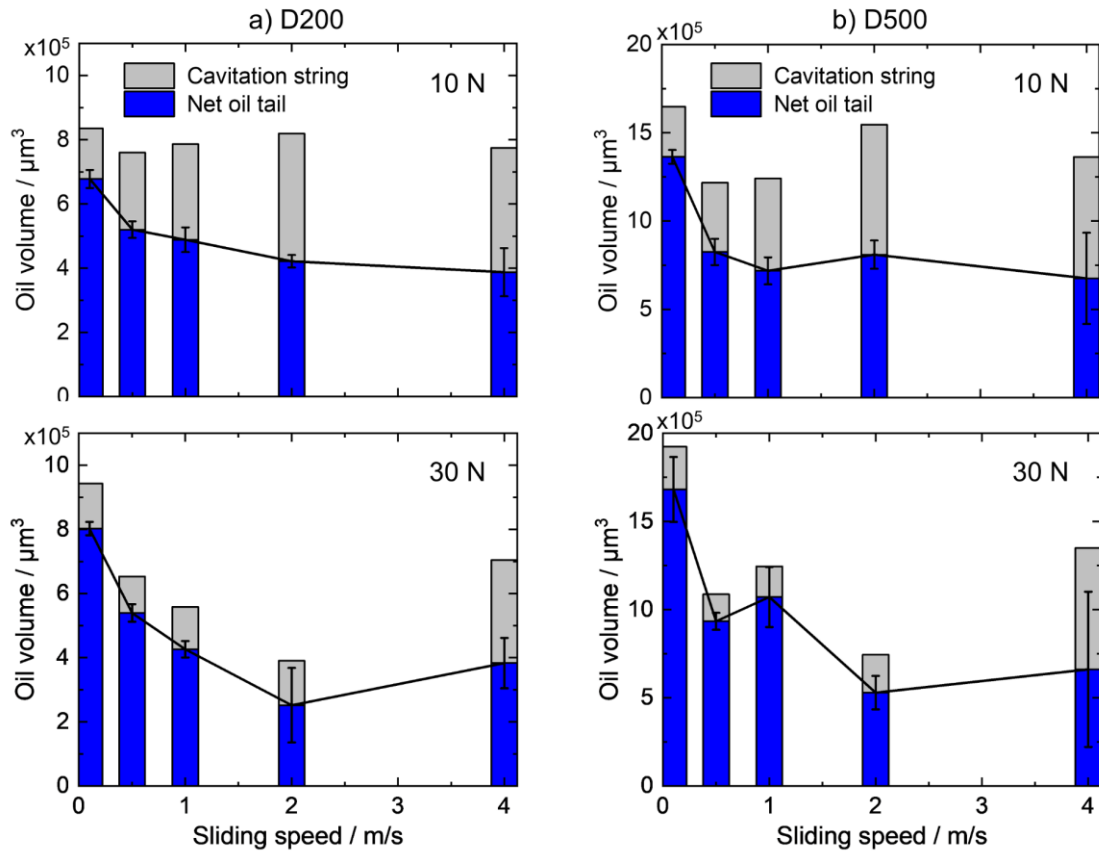


Figure 4.20: Oil volumes at about $p = +1.0$ mm, i.e., the position also shown in Figure 4.19, with different pore sizes and normal loads. The gross oil tail volume corresponds to the entire bar height that is divided into neighboring cavitation string volume (top, gray) and net oil tail volume (bottom, blue). The error bars indicate one standard deviation across the 20 images acquired with the stroboscopic timing set for $p = +1.0$ mm.

With few exceptions, Figure 4.20 shows that the nOTV decreases with increasing sliding speed for both loads, while the gOTV does not show any clear trend. Thus, the net effect of the pore is greatest at the lowest speed, where it increases the local amount of oil by a factor of 5.3 - 7.9 with respect to the cavitation string volume. At 4 m/s the presence of the pore barely doubles the locally available oil volume. These observed results are consistent with the previously reported enhanced tribological performance with textured pockets in the reversal zone in reciprocating contacts and the finding that the friction reduction due to the micro-scale surface texture (pocket) occurs only in the boundary and mixed regimes [74] [170] [171] [172], although through a different mechanism, macro-scale texture can reduce the friction in the hydrodynamic regime [173]. The errors bars, representing the standard deviation across each 20-shot data set, are mostly largest for the highest speed. Part of this is due to the fact that the

spatiotemporal jitter is greatest at the highest speed, since each bar in Figure 4.20 represents the measurements at one particular stroboscopic image timing that actually results in certain spread in the pore position p . Nevertheless, Figure 4.18 shows that the real scatter in at 4 m/s is in fact significantly larger than at all other speeds. Consistent with the qualitative observations in the single shots in Figure 4.19, also the multi-shot means in Figure 4.20 show that the higher load of 30 N does not correspond to a significant difference in the nOTV. Also consistent with the picture that has emerged thus far, Figure 4.20 shows sub-linear scaling of the nOTV with the pore diameter. Averaged over all sliding speeds, the nOTV from the 500 μm pore is only about 1.8 and 2.0 times greater than that from the 200 μm one for 10 and 30 N normal load, respectively.

4.2.4 Influence of pore depth

In Figure 4.21, the influence of the different pore depths from $h = 2 - 80 \mu\text{m}$ on the oil tail is shown at a fixed pore position, as in Figure 4.19, for a speed of 0.5 m/s and a load of 10 N. The 2 μm deep pore has very little effect on the oil film. The single shot presented here shows slightly wider cavitation strings near the contact zone. Apparently, the oil volume in this pore is too small. In contrast, all deeper pores yield a distinct oil tail. For the 20 μm deep pore, the tail is partially detached, while for 40 and 80 μm it is completely attached, even though (due to jitter) in the particular single shots shown for these latter two depths the pore happens to be slightly further from the contact zone than for the 20 μm shot. The tail from the 80 μm pore is the most contiguous, least ruptured one, but the general morphology of the oil tails from the 40 and 80 μm deep pores is very similar. Figure 4.21 also shows that from $h = 20$ to 40 to 80 μm the pore contains an increasing amount of residual oil. The close-up in the bottom-right of Figure 4.21, where the color scale has been adjusted to avoid clipping, shows that also for $h = 80 \mu\text{m}$ this residual oil is in an arc near the downstream edge of the pore. If we assume that the ideal “100% efficient” pore would be fully filled in the converging zone, and exactly fully emptied in the diverging part, the increasing amount of residual oil means decreasing efficiency of the pore with increasing depth. However, the 20 μm deep pore is already empty at $p = +1.0 \text{ mm}$ even though another 0.2 mm remain to the outlet edge. To quantify some of these observations, the ensemble-average oil volumes are shown in Figure 4.22.

4. Oil film around a cylindrical micropore visualized by fluorescence microscopy

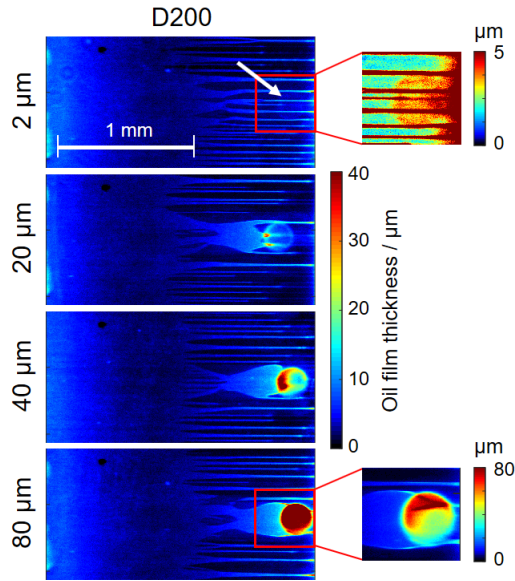


Figure 4.21: Cropped single shot images of the oil tail at about $p = +1.0$ mm with different pore depths as indicated. Sliding speed = 0.5 m/s, normal load = 10 N, pore diameter $D = 200 \mu\text{m}$. The square images on the right each show the region with the pore at higher magnification and adjusted ranges of the color scale.

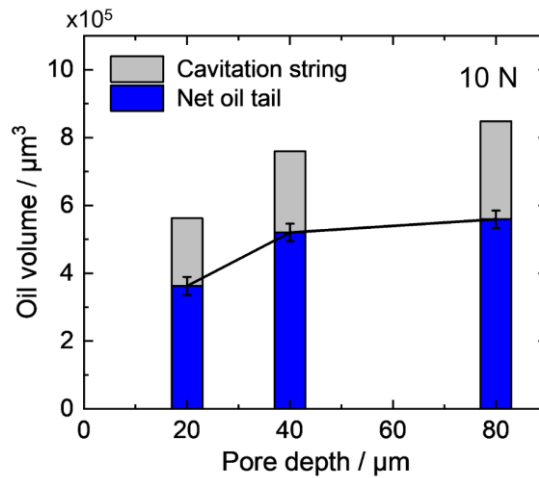


Figure 4.22: Oil volumes at about $p = +1.0$ mm, i.e., the position also shown in Figure 4.21, with different pore depths. The gross oil tail volume corresponds to the entire bar height that is divided into neighboring cavitation string volume (top, gray) and net oil tail volume (bottom, blue). The error bars indicate one standard deviation across the 20 images acquired with the stroboscopic timing set for $p = +1.0$ mm. See text concerning the missing data point at a pore depth of $2 \mu\text{m}$.

Figure 4.22 shows that the nOTV induced by the pore monotonically increases with pore depth, but with decreasing slope. The nOTV from the $2 \mu\text{m}$ deep pore shown in Figure 4.21 was not evaluated here, since the segmentation of the oil tail via thresholding could not be performed in a meaningful and reliable fashion. This is because for the $2 \mu\text{m}$ deep pore at this position, the morphological features of the cavitation strings dominate the oil tail, as Figure 4.21 shows.

4. Oil film around a cylindrical micropore visualized by fluorescence microscopy

Nevertheless, because of this apparent lack of influence of the pore on the oil film, we may qualitatively assign to the 2 μm deep pore a near-zero nOTV and a cavitation string volume similar to that of larger pores. With this qualitative assignment for the shallowest pore in mind, the nOTV shows an asymptotic trend with the most substantial increase from 2 to 20 μm depth, while that from 40 to 80 μm is insignificant. In the literature, there are works that investigated the influence of the depth-over-diameter (DOD) ratio of surface textures as a design parameter for improving lubrication [111] [174]. A DOD ratio of 0.10 - 0.18 was found to maximize the fluid pressure in contact zone. In our case, that would be a depth between 20 and 36 μm . This is consistent with the results shown in Figure 4.22 in that this is in fact the range where on one hand the nOTV is still sensitive to changes in pore depth, and on the other the pore contains enough oil to generate a continuous oil tail throughout almost the entire contact zone.

4.2.5 Comparison to total internal reflection fluorescence (TIRF)

In order to distinguish the oil film on the liner from that adhering to the PRS surface, imaging with total internal reflection fluorescence (TIRF) was additionally performed. This method has been used also by some authors [18] [78] to visualize the oil adhering to the cylinder liner wall.

Figure 4.23a shows the optical path layout using TIRF with a long-distance microscope. To achieve TIR, compared to the layout shown in Figure 4.9, the laser beam direction was changed to an indirect illumination, which resulted in a decreased laser energy illuminating the oil in the PR/CL contact.

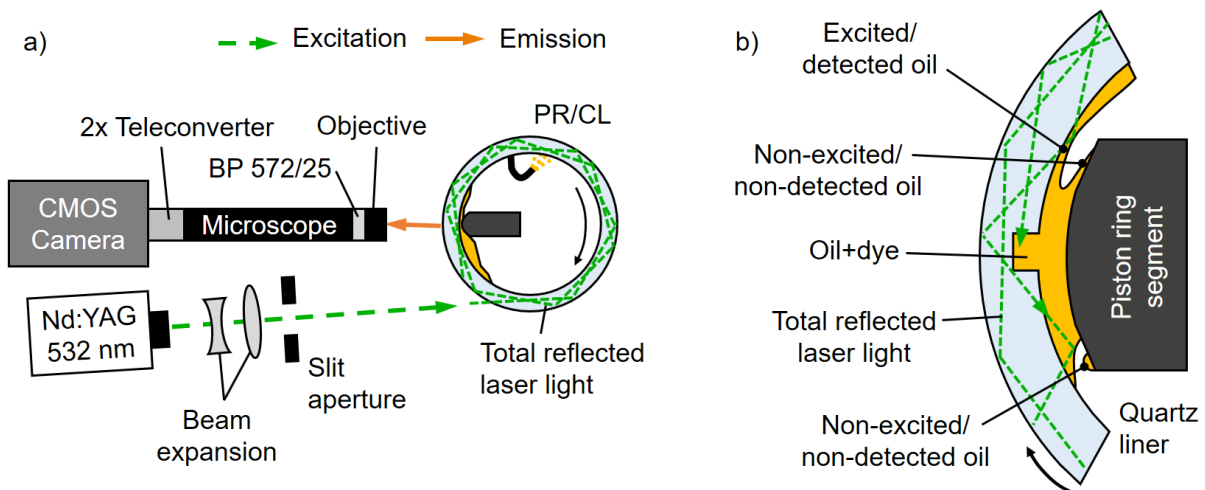


Figure 4.23: Indirect illumination using a total internal reflection method. a) Its optical path layout with a laser, long-distance microscope, camera and RRV tribometer. b) Schematic sketch of the total reflection principle showing an excited/detected- as well as non-excited/non-detected oil.

Thus, a tenfold increased dye concentration of 1.0 mmol/L was used to obtain a sufficient fluorescence intensity. Except for that, the setup and operating conditions are same maintained as shown in Figure 4.9 and Figure 4.10. The laser light enters the quartz liner. The

4. Oil film around a cylindrical micropore visualized by fluorescence microscopy

angle of the incident laser beam is adjusted such that total internal reflection occurs: where the beam encounters a glass/air interface at an incidence angle, θ , greater than the critical angle θ_c , the light is completely reflected within the glass. The critical angle given by Snell's law is $\theta_c = \sin^{-1}(n_1/n_2)$, where, n_1 and n_2 are the refractive indices of quartz glass and air, which are 1.45 [175] and 1.00, respectively. As shown in Figure 4.23b, in some regions the laser light encounters the glass/oil interface. In this case, it can mostly penetrate into the oil, because the refractive indices of quartz glass and oil (1.4 - 1.5 [176]) are very similar. However, the oil film only adhering to the piston ring surface cannot be excited and detected, since the beam is again completely reflected at the oil/air interface.

Figure 4.24 shows LIF images analogous to those in Figure 4.17, but now imaged via TIRF. These images qualitatively evaluated because they are neither background nor flat-field corrected.

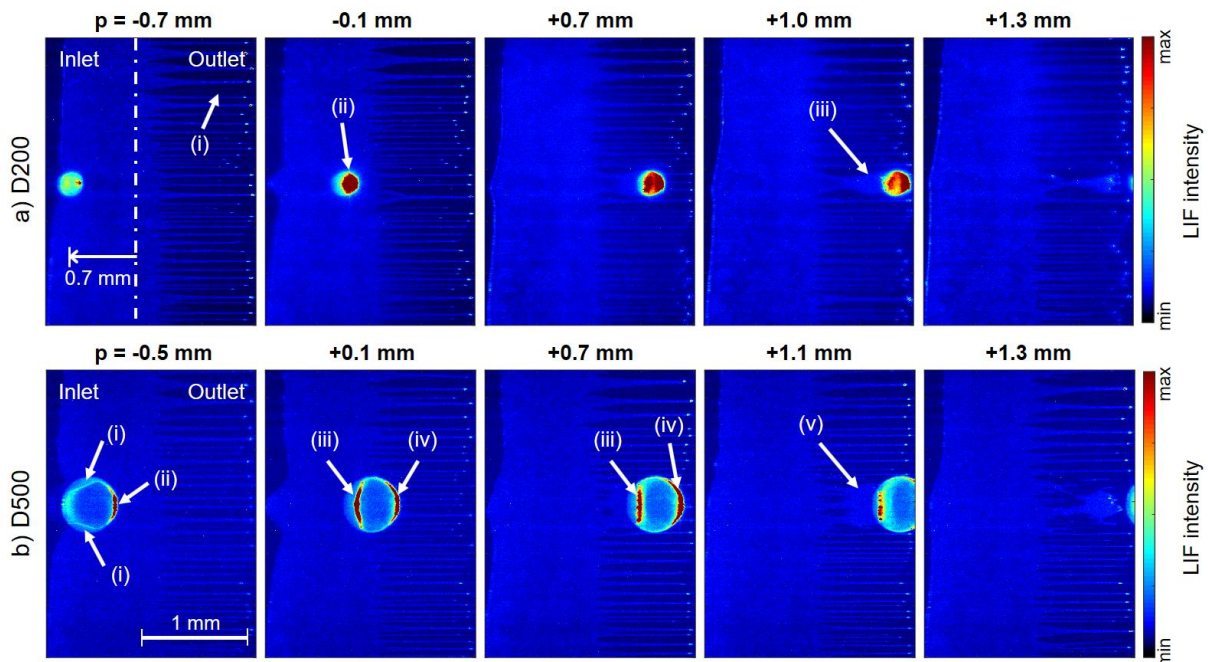


Figure 4.24: Total internal reflection fluorescence (TIRF) images of the oil film behavior and the temporal evolution of the oil tail. Operating conditions are the same as Figure 4.17: sliding speed = 0.5 m/s, normal load = 10 N. Pore diameter x depth = a) 200 x 40 μm , b) 500 x 40 μm .

Overall, the oil film behavior around the pore is comparable to that seen from “standard” LIF. One of the most dissimilar features is the area near the cavitation strings (Figure 4.24a-(i)). The random oil attached and collected on the PRS surface, not on the liner, is not visible, while it is observed in the back of the cavitation strings as a blurred oil film in Figure 4.17 and Figure 4.19. This confirms that TIRF is working as intended. The other dissimilar feature in comparison to Figure 4.17 is the oil inside of the pore. In Figure 4.24a-(ii), it seems like the pore is never fully filled by the oil, which disagrees with Figure 4.17a. For the pore with a bigger

diameter, this disagreement is observed in Figure 4.24b-(i) and (iii) as well. This is not a physical phenomenon but could stem from the direction of the indirect laser beam, its relatively weak energy per area, and the increased dye concentration. As shown in Figure 4.23b, the internally reflected laser beam enters the region under the PRS from the PR/CL diverging side, i.e., outlet. Thus, the oil in the pore absorbs the laser light mostly from the outlet to the inlet. However, the combination of the low laser energy and the high dye concentration can yield nearly complete absorption. The laser light cannot reach the oil that lies more in the inlet direction in the pore. The results with the larger pore are consistent with this. In that case, the laser beam first enters the very thin oil film adhering on the outlet side's inner wall of the pore in Figure 4.24b-(ii) or (iv). It is mostly reflected at the oil/air interface since the pore is not fully filled, as shown in Figure 4.17b. Nevertheless, a small portion of the laser light reaches the oil in Figure 4.24b-(i) and (iii), but it can excite only the oil near the interface and is mostly absorbed due to its weak energy. It is thought that the actual oil distribution in the pore is identical in Figure 4.24b-(i) to (iv) and in Figure 4.17b. Finally, the features of the oil tail are very similarly in Figure 4.24a-(iii) and Figure 4.24b-(v) and in Figure 4.17. This indicates that the oil in the oil tail fully fills the space between the PR/CL surfaces and thus, simple Couette flow with shear occurs here.

4.3 Application in a single-cylinder optical engine

4.3.1 Experimental set-up

The measurement method using the fluorescence long-distance microscope is applied to an optically accessible single cylinder research engine (Figure 4.25). The engine is based on the 2.01 version of the Mercedes-Benz M274 gasoline engine. Relevant engine parameters are listed in Table 4.2.

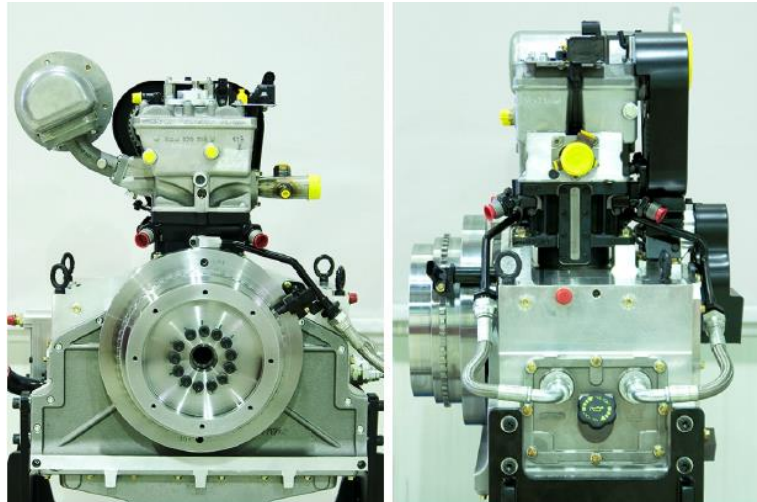


Figure 4.25: Photo of the optically accessible single cylinder research engine [18]. a) Front and b) side view.

Table 4.2 Engine parameters

Displacement [cm ³]	498
Compression ratio	9.8
Bore [mm]	83
Stroke [mm]	92
Fuel injection	Piezo DI
Max. speed [min ⁻¹]	6000
Max. load (IMEP) [bar]	14

For optical access, parts of the cylinder on the thrust and anti-thrust side were replaced with two honed sapphire windows (height: 105 mm, width: 16 mm) as shown in Figure 4.26 and described in more detail in [42]. Previous and concurrent experiments in our group used fluorescence imaging over all or a large portion of these windows to investigate the behavior of oil and fuel and their interaction with the gas phase [90] [91] [177] [178] [179]. Now that we

4. Oil film around a cylindrical micropore visualized by fluorescence microscopy

have established LIF microscopy in the RRV tribometer, it may be interesting to see what oil-film features these previous investigations with lower magnification might have missed.

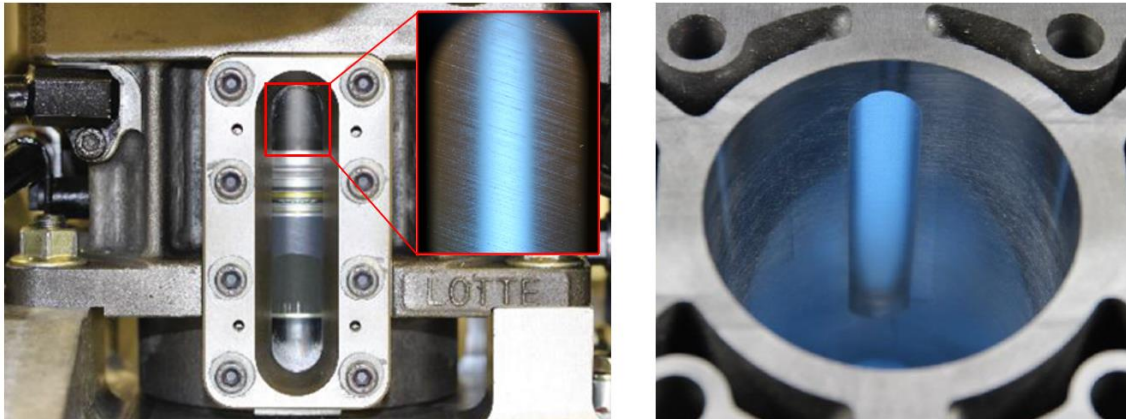


Figure 4.26: Photo of the sapphire window for an optical access on the thrust side and piston rings in a single cylinder optical engine (left). Honing structure on the sapphire window (enlarged). Inside view of its cylinder liner, where a part was replaced with a honed sapphire window, shown without a piston (right). [42]

The honing structure was measured by confocal microscopy and is presented in Figure 4.27. The surface structures are intermittently connected showing a groove-like formation; however also present are some non-connected micropore-like characteristics in like on the honing structure on the conventional GG liner shown in Figure 3.9.

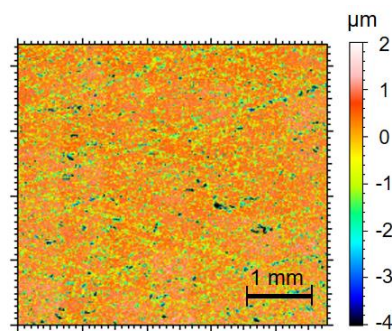


Figure 4.27: Surface topography of the honing structure on the sapphire window in a single cylinder optical engine measured by confocal microscopy, μ Surf (Nanofocus®).

Figure 4.28 shows a side view of the optical path and Figure 4.29 a photo of the experiment setup. The detection method using LIF and the long-distance microscope is the same as discussed in chapter 4.1 and 4.2. Thus, the magnification and pixel size are almost the same, but the result images in chapter 4.3.2 are not cropped, since the ROI is equal to the whole FOV. Here, the laser fluence is changed to about 140 mJ/cm^2 and a dye concentration of about 0.07 mmol/L is used. The lubricant is a non-fluorescent, low-additive poly-alpha-olefin (PAO) with a HTHS viscosity of $3.61 \text{ mPa}\cdot\text{s}$. The temperature of this oil is $50 \text{ }^\circ\text{C}$. One image is

4. Oil film around a cylindrical micropore visualized by fluorescence microscopy

acquired per cycle, with the vertical elevation of the imaging train and the crank angle of the engine determining the position of the 2.7 x 3.2 mm field of view relative to the piston and its rings.

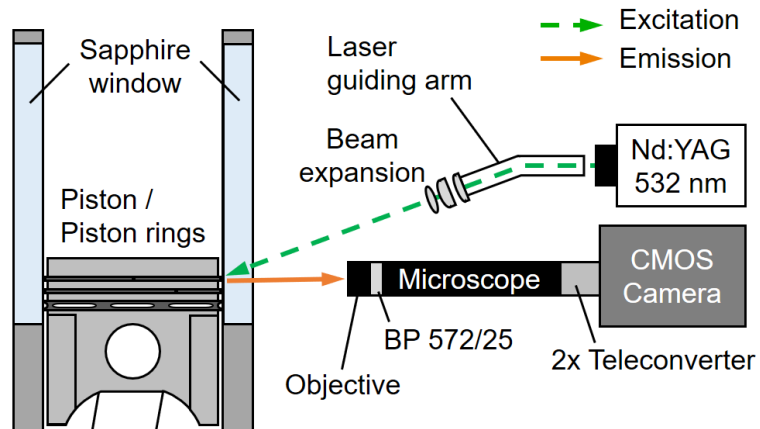


Figure 4.28: Side view of the optical path layout with optical engine, laser, camera and long-distance fluorescence microscope.

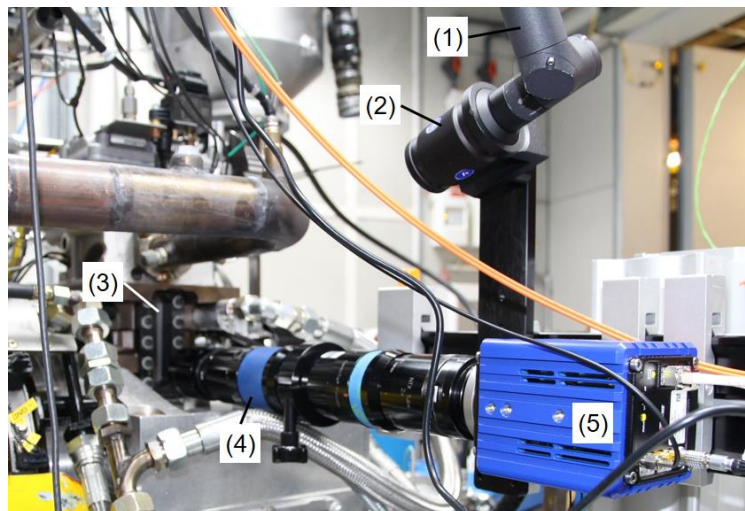


Figure 4.29: Photo of the optical setup with optical engine. (1) Laser guiding arm, (2) laser beam shaping, (3) sapphire window, (4) long-distance microscope, and (5) CMOS camera.

4.3.2 Results

Figure 4.30a shows a typical LIF image from the previous work in our group [42] with a field of view covering the whole window. Figure 4.30b and c are example LIF images recorded in this work with a long-distance microscope at a similar crank angle and with similar engine operating conditions. Figure 4.30b and c each were acquired in separate experiments.

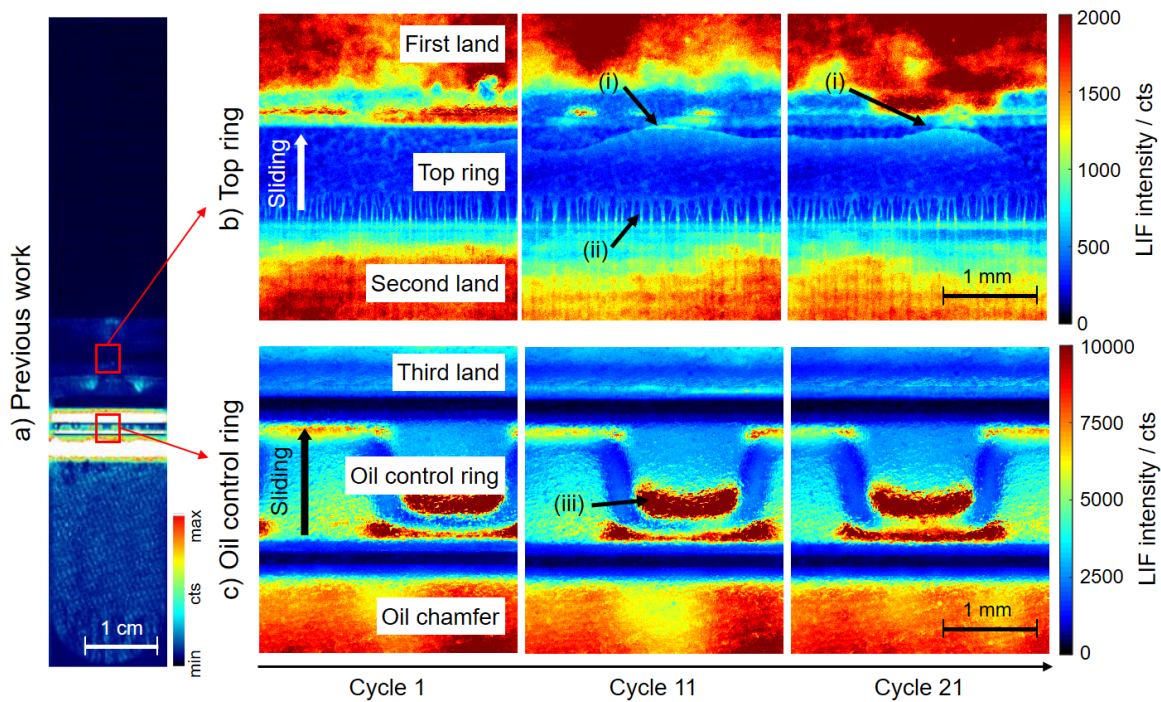


Figure 4.30: LIF images of the oil film in the optical engine. a) Typical image from the previous work [42] showing the entire window length (110 °CA bTDC, 2200 min⁻¹, fired engine operation, anti-thrust side, compression stroke IMEP = 7.2 bar). Oil film measured in this work. b) Near the top ring region (103 °CA bTDC) and c) near the oil control ring region (89 °CA bTDC) with a high magnification (2000 min⁻¹, fired engine operation, thrust side, compression stroke, injection pressure = 250 bar, IMEP = 5 bar).

For Figure 4.30a, the entire length of the sapphire window was detected with low image magnification, which enabled investigating the macroscopic oil film behavior. On the other hand, Figure 4.30b and c resolve details of the oil film behavior near each piston ring. Note that Figure 4.30b and c are on a different color scale (the latter image being actually much brighter), and that a background correction was performed, not a full quantification. In these images from the compressions stroke, the piston is moving upward as indicated by the arrow in sub-figures b and c.

In Figure 4.30b, a sort of “blowby” effect is detected (i), showing the downward oil movement from the first land to the top ring towards the second land as reported in [42]. The cavitation strings in the outlet region are also observed (ii), as detected in the PR/CL contact of the RRV tribometer. Figure 4.30c shows details of the shape of the expander and the two rails of the oil

4. Oil film around a cylindrical micropore visualized by fluorescence microscopy

control ring. Over the course of the experiment, the ring shows a slight rotation, translating features along the piston diameter, here in a leftward direction. The oil scraped off the liner is pushed downwards during the upwards piston motion and thus the accumulated oil in the expander (iii) is also seen.

The LIF image in Figure 4.31 was recorded at lower sliding speed (i.e., slower engine rpms) and higher normal load (caused by higher in-cylinder pressure). Note that the color scale differs from Figure 4.30b. The red dashed lines indicate the directionality of the surface texture on the sapphire window, which is similar to honed, but mostly non-connected (see Figure 4.27). The oil tails' starting points are along these red dashed lines, although they are relatively short due to the structures' shallow depth. Nevertheless, we can see that the oil is carried from inlet to the outlet via the surface textures and extracted in the outlet region, just as observed in the tribometer. The consistency of the results between the different experiments – engine and tribometer – confirms the wide range of applicability of the high-resolution LIF imaging developed here.

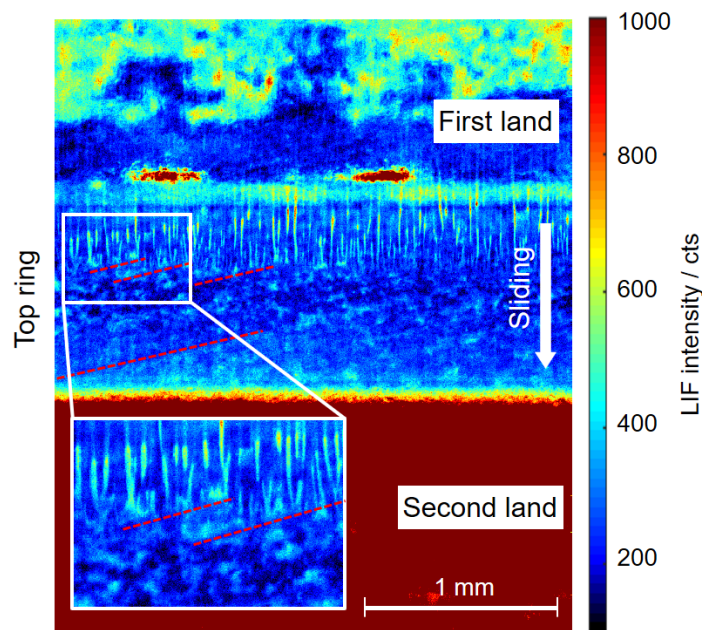


Figure 4.31: LIF image of the oil film near the top ring region in a single cylinder optical engine. (1000 min⁻¹, 119 °CA aTDC, fired engine operation, thrust-side, expansion stroke, IMEP = 10 bar)

4.4 Chapter conclusions

This work presents quantitative fluorescence microscopy imaging of the oil film around a single cylindrical micropore on a quartz liner pressed against a metal piston ring segment in a rotational tribometer. Each laser-made micropore was meant to be a single generic representation of the many irregular surface features on spray-coated cylinder liners. Two different pore diameters were compared, both with a pore depth of 40 μm . 200 μm diameter are more representative of the characteristic dimensions of pores in spray coatings, while 500 μm are larger. For a diameter of 200 μm , the pore depth was varied from 2 to 80 μm .

In the images, an “oil tail”, extracted from the pore and deposited downstream of it in the diverging PR/CL gap, was detected. Its spatiotemporal evolution as well as net volume under varied conditions, such as different pore diameters, sliding speeds, and normal loads, was studied. The measurement bias from fluorescence stray light from oil accumulated at the PRS edges was evaluated. Significant observations can be summarized as follows:

- When the pore enters the region under the PRS, the oil is drawn into the pore, which might represent the ‘inlet suction’ mechanism that can increase the overall load carrying capacity. After the pore passes through the minimum PR/CL gap, the oil is extracted from the pore due to the pressure drop in the diverging gap and the oil tail is developed by the lubricant shear.
- The extracted oil tail volume increases with increasing sliding distance of the pore from the PR/CL gap minimum. The initial increment, when the pore just passes the gap minimum, is very small, but the increment becomes much greater and approximately linear until the pore approaches the outlet edge of the PRS. The lowest speed corresponding to the mixed regime shows the largest oil volume flow per sliding distance.
- Lower sliding speed results in a wider and less ruptured oil tail. Its net volume after the same sliding distance shows the tendency that the lower the speed is, the more the oil is extracted from the pore. This trend is very gradual for sliding speeds of 0.5 m/s and above, but the lowest sliding speed of 0.1 m/s resulted in a marked increase in oil extraction.
- Increasing the load from 10 to 30 N does not yield a significant difference in the morphological features of the oil tail nor its volume. However, since for higher load the mixed lubrication regime visibly persists to higher speeds, the pore may be particularly beneficial over a wider range of conditions.
- For a depth of 40 μm , the pore with a diameter of 200 μm is fully filled by the oil under the minimum PR/CL gap, while with a diameter of 500 μm the pore is not fully filled, and subsequently oil is not extracted from the full width of the pore, but rather from a section of its trailing edge. The oil tail from the bigger pore is wider in absolute width

and has a greater volume than that from the smaller one, but neither increase is proportional to the characteristic dimensions of the pore. In particular, the oil tail volume increases by a factor of 1.8 to 2.0, which is less than the 2.5-fold increase in diameter and much less than the than the 6-fold increase in volume. This sub-linear scaling is attributed to the differences amount and location of oil in the pore. The decreasing trend of the oil tail volume with increasing speed is similar for both pore diameters.

- For pores with a diameter of 200 μm , the oil tail volume increases with increasing depth up to a depth of 40 μm , while an 80 μm deep pore retains much of its oil fill and does not yield any further increase in tail volume.
- For the geometry and among the cases investigated here, a pore with 200 μm diameter and 20 - 40 μm depth is close to ideal at 10 N load and 0.1 m/s sliding speed. However, because of experimental limitations (for example, the spatial resolution of the imaging system and the texturing capabilities), this optimum parameter set is also in part at the limits of the investigated parameter space.
- Given that the 200 μm pore is more representative of the microscopic texture of a spray coated liner, the results suggest that the surface porosity created by such a coating might work best near the piston reversal points (top and bottom dead center in an engine). In fact, this is also where an improvement in lubrication would be most beneficial, since it is here that the reciprocal motion necessarily causes mixed-regime friction.
- The detection system with the fluorescence long-distance microscope was applied to an optical single-cylinder engine. The results were consistent with those in the RRV tribometer. This approach allows imaging the microscopic oil film behavior within the piston assembly group from the top piston ring to the OCR with high magnification and resolution.

5 Temperature imaging in the oil film by a ratiometric two-color, two-dye fluorescence scheme

The chapter presents the initial development of a technique for two-dimensional temperature measurements in oil films by means of a two-color, two-dye fluorescence ratiometric method. The oil doped with two dyes is excited by a blue LED, and the dyes' fluorescence, whose temperature dependencies are different, is detected by a long-distance microscope in two separate spectral bands. The intensity ratio between the two bands is independent of the oil film thickness, while the temperature is indicated by the intensity ratio. An initial demonstration with the heated, thin oil film in the sliding PR/CL contact is presented.

This chapter has not been published previously elsewhere. The dye selection is based on a spectral investigation at the Institute for Energy and Materials Processes (EMPI, formerly IVG) – Reactive Fluids, some of which is reported in the Master's thesis of Heimrath [180].

5.1 Methods

5.1.1 Fluorescence excitation and detection for LED-based temperature measurements

LED

In chapter 5, a RGB-LED (LZ4-00MC00 from LED Engin) is chosen as a light source instead of the 532 nm Nd:YAG laser in chapters 3 and 4. This is because one of the dyes, Lumilux CD 345, cannot be excited by the 532 nm light and also the high energy of the laser can damage the front objective in the long-distance microscope in coaxial illumination (see chapter 5.1.2). Thus, a blue chip in the LED, which shows the highest peak of the spectral power at around 460 nm, is employed. It is operated continuously, i.e., not pulsed, to obtain the maximum light output, with a forward voltage of 3.4 V yielding a current of 0.6 A. A camera exposure time of 100 ms is set.

Dye and filter

Preliminary work [180] suggested that a suitable dye combination for the aforementioned LED is lumilux CD 345 and pyr 597 with a dye concentration of 0.5 mmol/L for each dye.

CD 345 absorbs the blue LED excitation (at around 460 nm) as shown in Figure 5.1a and emits fluorescence, while the absorption spectrum of pyr 597 and the LED excitation overlap only in a narrow spectral region (Figure 5.1b).

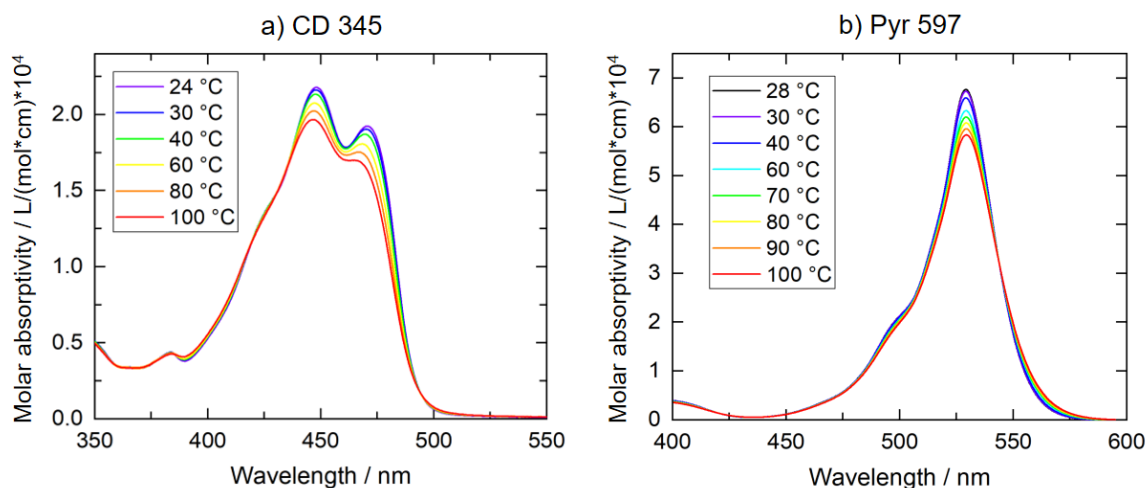


Figure 5.1: Absorption spectra of Lumilux CD 345 and pyromethene 597 at different temperatures measured by EMPI, Duisburg-Essen University with a spectrofluorometer.

Little reabsorption by the pyr 597 occurs in this work, since our experimental results in chapter 5.1.3 show the characteristics of an optically thin system. Nevertheless, the detected emission intensity of the pyr 597 is comparable to that from the CD 345, presumably due to the following reasons: first, the molar absorptivity of the pyr 597 is generally much higher than that of the CD 345. Thus, the absorption of the pyr 597, which occurs only in the small overlap region with the LED, could be substantial and the emission from that would be sufficiently high. Second, as shown in Figure 5.2, the filter for the pyr 597 (red channel) covers much wider spectral region than that for the CD 345 (blue channel) and the sum of the fluorescence intensity of the pyr 597 might be comparable to that of the CD 345. Figure 5.1 also shows that the absorptivity of both dyes decreases slightly with increasing temperature.

The emission spectra of the selected dye combination at different temperatures are shown in Figure 5.2. To separate the temperature-insensitive and temperature-sensitive regions, a band-pass (BP) 520/40 nm and a long-pass (LP) 550 nm filter were employed in the blue and red spectral channel, respectively. In the red channel, the fluorescence intensity at the peak wavelength decreases from 30 to 60 °C by about 35 %, while it is almost constant in the blue channel. A beam splitter at LP 458 nm was chosen, since a blue LED with peak emission at 443 nm was initially to be used. However, a brighter blue LED with a peak emission at 460 nm as shown in Figure 5.2 were finally employed, because the detected LIF signal was insufficient. To avoid a possible scattered light from this LED in the blue channel, a BP 460/60 nm was additionally used on the excitation side.

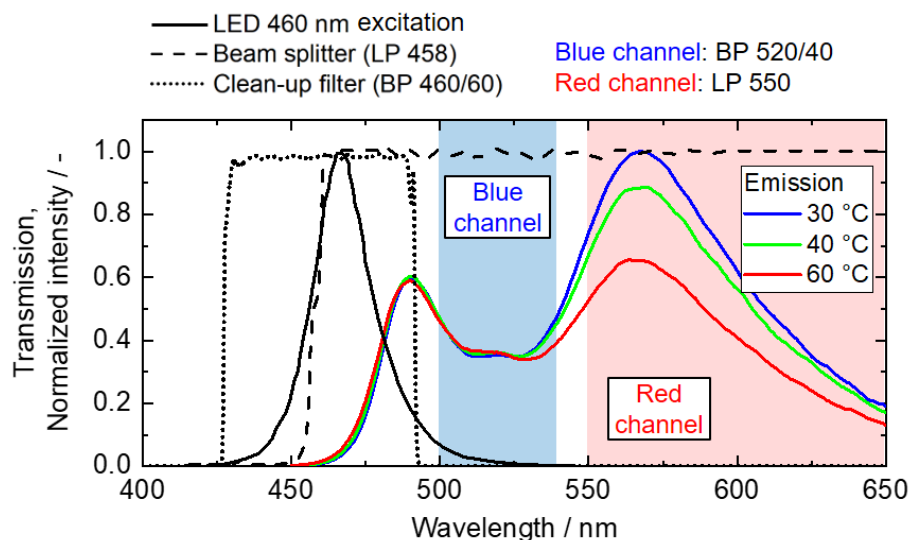


Figure 5.2: Spectral features of excitation, filter, beam splitter, fluorescence emission of the dye mixture with Lumilux CD 345 and pyromethene 597 (dye concentration of 0.5 mmol/L for each dye) at different temperatures and two detection channels.

Photobleaching

As discussed in chapter 3.1.5.2, a dye can permanently lose its fluorescing ability when it is exposed to high-intensity light for a long time. Thus, a photobleaching test was carried out.

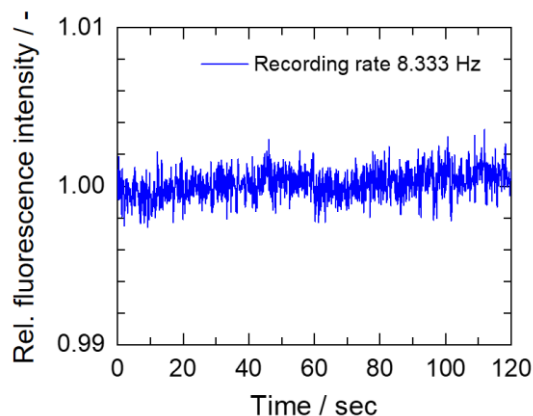


Figure 5.3: Photobleaching test of a dye mixture (pyr 597 and CD 345 with a concentration of 0.5 mmol/L for each) within 120 sec (i.e., recording of 1000 images with 8.333 Hz recording rate) with continuous operating condition of the LED 460 nm.

As depicted in Figure 4.13, a precision foil with a thickness of 20 μm is inserted near the top end of the PRS and the oil between the PR/CL gap at a standstill is illuminated continuously by the LED 460 nm. At 8.333 Hz, 1000 images were recorded in 120 sec. The detected fluorescence intensities in the small area near the top end of the PRS, which has a film thickness about 20 μm , were evaluated and normalized by their initial value. The result is

plotted in Figure 5.3. Degradation or photobleaching did not occur, and Figure 5.3 shows the fluctuation of the LIF intensity is only $\pm 0.2\%$ in time.

5.1.2 Experimental arrangement and parameters

The experiment is conducted in the RRV tribometer as described in chapter 4. The system with its optical path is presented in Figure 5.4, and Figure 5.5 shows a photo of that.

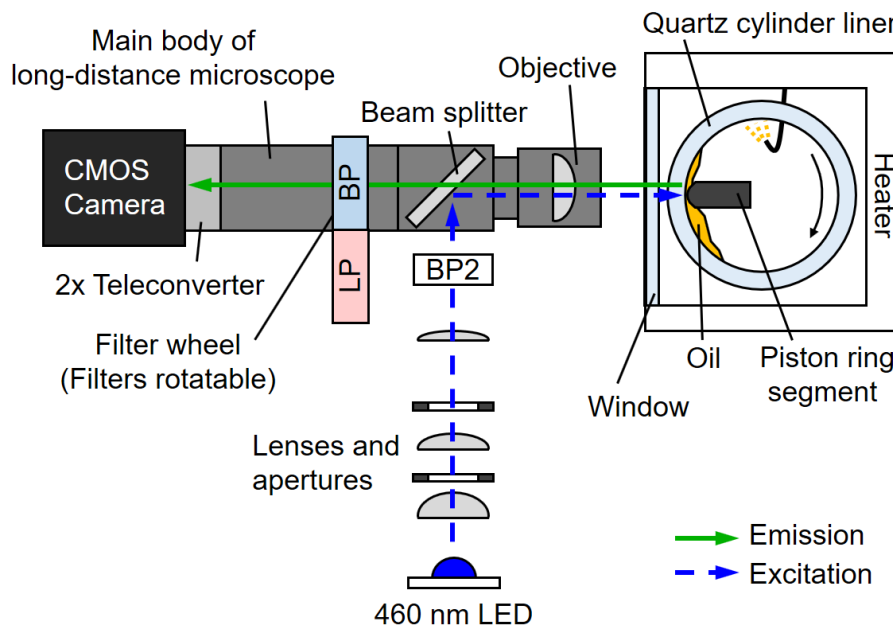


Figure 5.4: Top view of the optical path of the imaging system with LED, tribometer, and long-distance microscope in coaxial illumination.

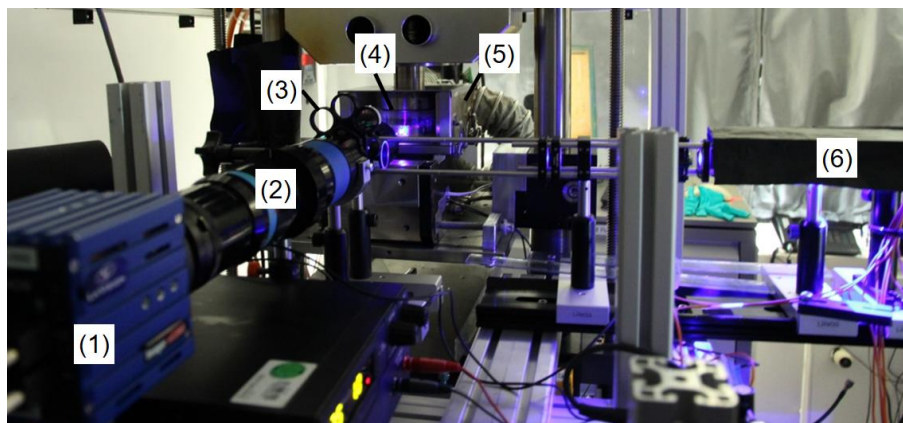


Figure 5.5: Photo of the optic setup. (1) CMOS camera, (2) long-distance microscope, (3) filter wheel, (4) PR/CL assembly, (5) heater, (6) LED, lenses and apertures.

The LED light at about 460 nm is formatted in Köhler-illumination, as typical in low-coherence microscopy. After passing through BP2 (460/60 nm clean-up filter in Figure 5.2), it is reflected towards the oil film by the 45° beam splitter (LP 458 nm, spectral feature in Figure 5.2). It

passes through the front objective (CF-3, Infinity USA), the heater window, and reaches the oil film in the tribometer. This test rig will be discussed below. The fluorescence light from the oil passes through the beam splitter, a filter wheel, the main body of the long-distance microscope (K2, Infinity USA) and a 2x teleconverter and is detected by a CMOS camera (Imager sCMOS, LaVision). The projected pixel size is 1.18 $\mu\text{m}/\text{pixel}$ and only the area near the top end of the PRS (about 2.5 mm height) is imaged due to the high magnification with fluorescence microscopy. A single camera captures two series of fluorescence images sequentially while the BP (blue channel) and LP (red channel) filters are changed in the filter wheel. Each series of images (100 for the calibration and 500 for the results) – one image per liner rotation – is acquired for averaging and further processing. Thus, this system is limited to examine steady-state flows.

The optical RRV tribometer is placed in the heater as shown in Figure 5.4. The configuration of the tribometer is the same as discussed in chapter 4 (Figure 4.1), but only the inner surface of the quartz liner is polished, without pores. The sliding speed is varied from 1 to 2 m/s and the normal load (F_N) is maintained at 5 N. The lubricant oil used in this chapter is PAO, and it is sprayed onto the inside of the liner at 0.1 mm^3 per liner rotation. Hot air is supplied in the heater box and the temperature is controlled with a thermocouple embedded in the PRS near its surface. The temperature is gradually increased from the room temperature (24 °C) to 60 °C.

5.1.3 Image processing including stray light correction and calibration

The image processing carried out prior to the temperature calibration is described by:

$$Ratio = \frac{\left\{ \langle I_{S,R} \rangle - \langle I_{BG,R} \rangle \cdot \frac{1}{\langle I_{FF,R} \rangle} \right\} \cdot (1 - X_{stray,R})}{\left\{ \langle I_{S,B} \rangle - \langle I_{BG,B} \rangle \cdot \frac{1}{\langle I_{FF,B} \rangle} \right\} \cdot (1 - X_{stray,B})} \quad (5.1)$$

where capital letters indicate two-dimensional images and brackets $\langle \rangle$ average over a series of 500 (for I_S) or 100 (for the rest) single shots. The terms in equation (5.1) are discussed in the following.

Background and flat-field correction

I_S indicates the recorded raw LIF image, and the background image I_{BG} recorded without oil and dye but with LED excitation is subtracted from that. As a second step, it is divided by the flat-field image I_{FF} (see chapters 3.1.7 and 4.1.5).

In order to acquire the flat-field image, the same method using an oil bath was employed as in Figure 4.12, but the incident light from the LED illuminated the ROI coaxially (Figure 5.6a). Comparing to Figure 4.12, the dye concentration and the illuminating energy are not

specifically adjusted for the flat-field acquisition and I_{FF} is not normalized. Figure 5.6b and c present the recorded flat-field images in each blue and red channel.

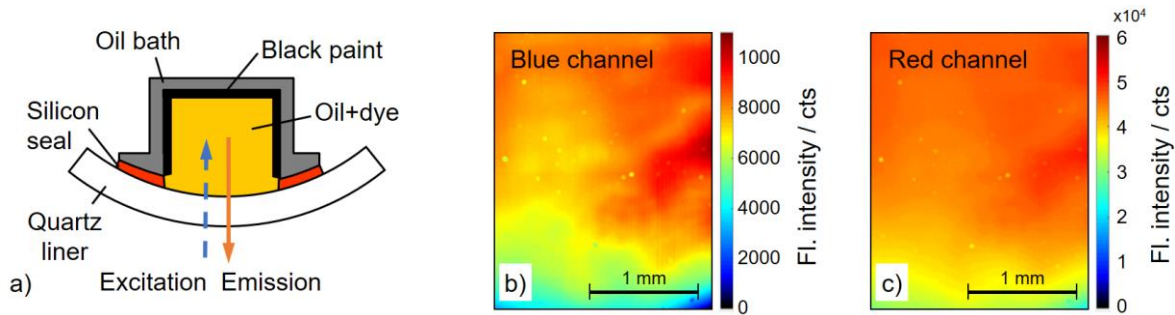


Figure 5.6: Flat-field image acquisition. a) Schematic sketch, b) flat-field image in blue channel and c) in red channel.

Stray light correction

The next step is to correct the stray light from the high fluorescence intensity in adjacent regions to the ROI. The in-situ measurement method of the stray light is very similar to that described in chapter 4.1.6 and will be here only briefly described focusing on the modified parts and results (Figure 5.7).

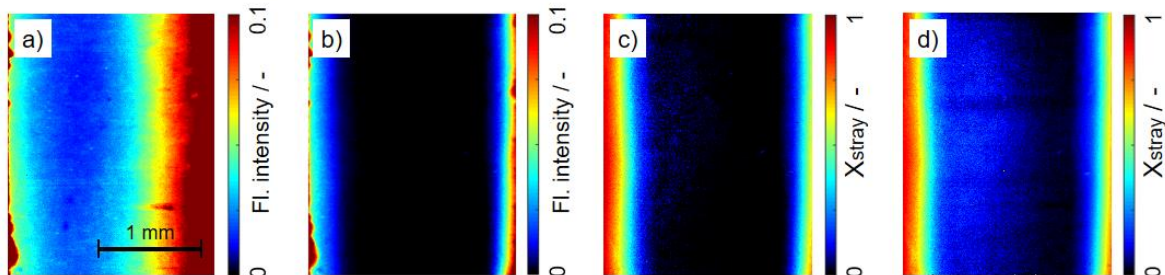


Figure 5.7: Stray light correction at standstill. a) Non-blocked image. b) Measured stray light intensity. c) Proportional stray light effect (b divided by a) in blue channel. d) Proportional stray light effect in red channel.

For Figure 5.7b, a black tape on the liner blocks the gathered oil at both edges of the PRS (like the regions (i),(ii) in Figure 4.16) from the LED illumination. We note that this was performed in current work at standstill, since the maximum exposure time of the camera (100 ms) to collect enough fluorescence intensity is too long to capture the edge of the black tape with a typical sliding speed of the liner of 1 or 2 m/s. The intensity difference in the ROI between the non-blocked (Figure 5.7a) and blocked images can be considered as the stray light (Figure 5.7b). To correct this, a proportion of the stray light across the field, X_{stray} , is calculated in Figure 5.7c (Figure 5.7b divided by Figure 5.7a). By multiplying $1 - X_{stray}$ with each result image as in equation (5.1), the stray light is corrected and the discrepancy of the gathered oil amount between standstill (stray light measurement) and rotation (result image with oil flow) can be

also minimized. Figure 5.7a-c show the examples in the blue channel (B subscript in the equation (5.1)). The same process is also performed in the red channel (R subscript in the equation (5.1)), and its stray-light proportion is shown in Figure 5.7d. Finally, the stray-light corrected image in the red channel is divided pixelwise by that in the blue channel for the *Ratio*. Here, a slight image coordinate discrepancy between the two channels caused by a physical offset between the BP and LP filter setup in the filter wheel is corrected in DaVis 8.4.0 (LaVision) program with a 3rd order polynomial function. In comparison with Figure 5.7c (blue channel), the area near the minimum gap in Figure 5.7d (red channel) shows a stronger stray light effect. This is probably caused by near-region-reabsorption, similar to Figure 3.27c. The unwanted emission from the regions (i) and (ii) in Figure 4.16 (stray light) plays the role of an external excitation light source in addition to the LED. Here, the mixture of the CD 345 and pyr 597 emits the light, and as the emission spectrum of the CD 345 overlaps the absorption spectrum of the pyr 597, only the pyr 597 is excited. The closer the area is to the minimum gap region, the stronger this near-region-reabsorption effect is due to the PR/CL gap geometry, as will be shown in Figure 5.8b.

Temperature calibration

To convert the ratio distribution into the temperature distribution by the equation (2.17), it was first examined whether our system is optically thin or thick according to Figure 2.13, Figure 2.14, and [38] [52], using the vertical and horizontal PR/CL gap geometries at standstill.

In Figure 5.8a, we employ the vertical gap at the lateral center of the PRS. As shown in Figure 4.13, the PRS is tilted by a precision shim foil with 20 μm thickness as well as by a pivot motion of its holder and pressed against the liner. The fluorescence intensity along the lateral centerline from the filled oil is plotted with the computed gap height (theoretical OFT). The measured data and its linear fit curve show linearity, which denotes that our system is optically thin in the sense of the Beer-Lambert law.

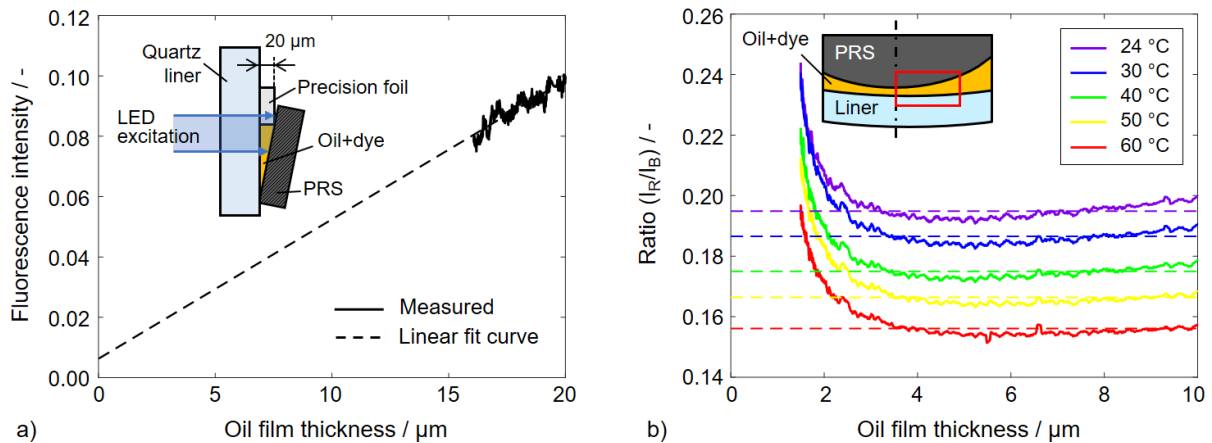


Figure 5.8: Verification of an optically thin system. a) Vertical PR/CL gap with a tilted PRS and the linearity of the fluorescence intensity against OFT in the blue channel. b) Ratio along the horizontal PR/CL gap at different temperatures. Solid lines are measured, and dashed lines are the average ratio in the area over 2.5 μm thickness.

Again, the intensity ratio along the horizontal PR/CL gap (Figure 5.8b) also shows the characteristic of the optically thin system. Here, for the temperature calibration, oil film images are recorded at standstill, with the film uniformly heated for each set point temperature between 24 and 60 $^{\circ}\text{C}$ and the images processed with the equation (5.1). The averaged ratios across the PRS length are filtered and plotted in Figure 5.8b from the minimum gap height (determined by Figure 5.7a) to the gap of 10 μm thickness (calculated by the radius difference of the PR/CL), i.e., within the red box in Figure 5.8b. The intensity ratios mostly show an independence on the OFT in the area over 2.5 μm thickness, while the area where the OFT is less than 2.5 μm presents OFT-dependent and higher ratios than the aforementioned area. This may originate from the following factor: As already shown in Figure 5.7c and d, the *outer* stray light effect on the region where the OFT is extremely thin (near the PR/CL minimum gap) appears more in the red channel than the blue one. We note that the outer stray light is from the gathered oil in the adjacent regions of the ROI (the regions (i) and (ii) in Figure 4.16).

Although we corrected this outer stray light according to the equation (5.1) and Figure 5.7, considering only the area under the PRS, the extremely thin oil film under the minimum gap (less than $2.5\ \mu\text{m}$) is additionally affected by the *inner* stray light and its near-region-reabsorption as in Figure 3.27c. We define here that the inner stray light is from the fully filled oil film near the PRS edge at a standstill. This might result in the falsely higher intensity additionally in the red channel than the blue one and thus the higher intensity ratios (I_R/I_B) around the minimum gap. This is not a physical phenomenon and this area will not be considered for the temperature calibration. In the measurements in chapter 5.2, this effect would be negligible, since the outlet area is not fully filled by the oil due to the cavitation strings and the inner stray light effect would be insignificant. Thus, it can be concluded that the intensity ratio (I_R/I_B) shows in general an independency on the OFT as in the OFT area over $2.5\ \mu\text{m}$ thickness, and it implies that our system is optically thin according to [38].

Figure 5.9 shows the temperature calibration curve. It was calculated from Figure 5.8b in the area where the OFT is over $2.5\ \mu\text{m}$ as discussed.

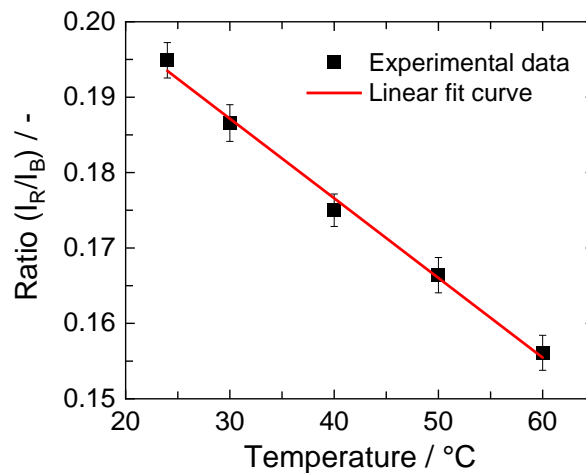


Figure 5.9: Fluorescence intensity ratio (red channel/blue channel) as a function of the temperature and its linear fit curve.

The fluorescence intensity ratio as a function of the temperature follows the expected linear behavior with the equation (2.17) and the temperature dependency (sensitivity) of the ratio is about $0.6\ \%/K$. A linear data fit ($R^2 = 0.99$) results in

$$Ratio = 0.2189 - 0.0011 \cdot T. \quad (5.2)$$

Using an inverse function of the equation (5.2), the temperature distribution can be calculated from the channel ratio. The temperature measurement uncertainty related to the calibration is $\pm 2.2\ ^\circ\text{C}$, which corresponds to the largest standard deviation, i.e., error bar in Figure 5.9. In addition, the thermocouple embedded in the PRS has an uncertainty of $\pm 0.8\ \%$, which is $\pm 0.5\ ^\circ\text{C}$ at the highest temperature of $60\ ^\circ\text{C}$ in this work. The uncertainty in the temperature

control by the hot-air heater contributes ± 0.2 °C. Assuming square-root addition, the total measurement uncertainty is ± 2.3 °C.

Examples from the image processing are shown in Figure 5.10. A pair of images recorded successively in the red and blue channels with an oil flow is shown in Figure 5.10a and b. These are background, flat-field and stray light corrected. Figure 5.10c presents the ratio distribution and from that converted temperature distribution by the equation (5.2) is shown in Figure 5.10d, which went also through the 2-by-2 binning operation for reducing the random noise [134] at the expense of reduced spatial resolution.

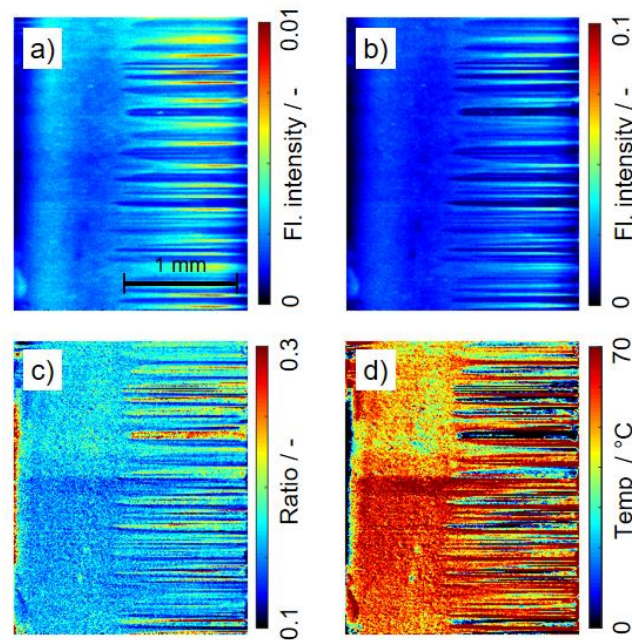


Figure 5.10: Typical intermediate results in image processing. Background, flat-field and stray light corrected image detected in the a) red channel and b) the blue channel. c) Fluorescence intensity ratio distribution (red/blue channel). d) Resulting temperature distribution. Set point temperature 60 °C, sliding speed 1 m/s, normal load 5 N.

5.2 Results

Figure 5.11 shows the temperature distribution of the oil film in the PR/CL contact during the liner's rotation with sliding speeds of 1 m/s (a) and 2 m/s (b). Here, the liner moves from the left to the right. The normal load is 5 N and the set point temperature increases from room temperature (24 °C) to 60 °C.

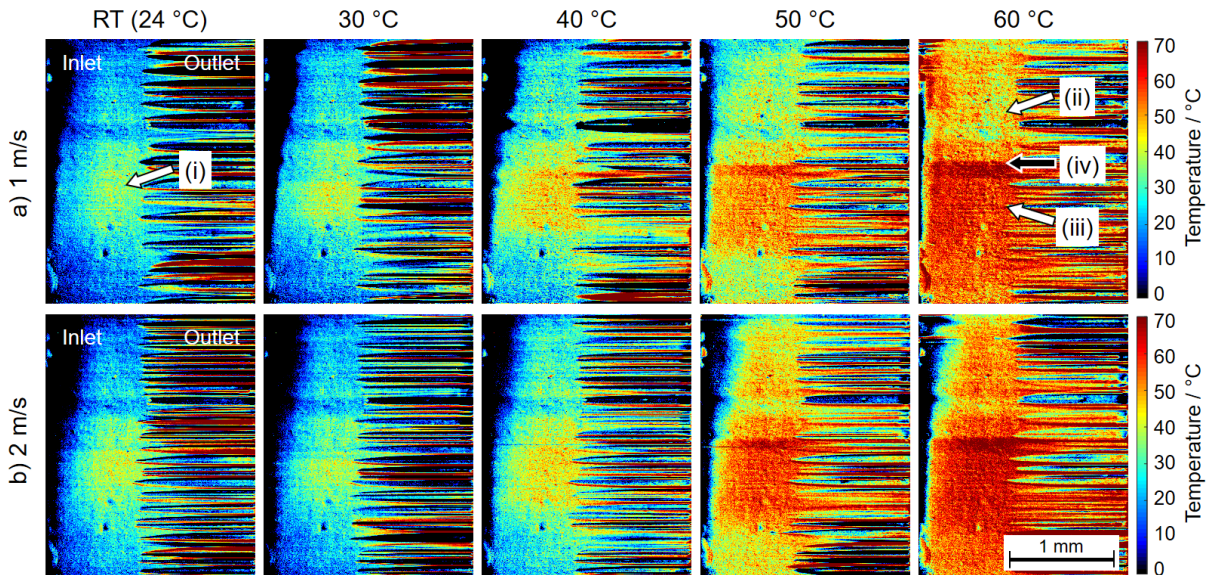


Figure 5.11: Temperature distribution of the oil film in PR/CL contact measured by two-dye fluorescence ratiometric scheme. Sliding speed 1 m/s (a) and 2 m/s (b), normal load 5 N, and the set point temperature is varied from the room temperature (24 °C) to 60 °C.

The overall features of the oil film development are the same as discussed in chapter 4. Here, only the inlet oil film temperature will be discussed, since the stripe pattern in the outlet (cavitation strings) was not steady during the liner rotation, while the inlet oil film was (see chapter 5.1.2). The optically measured temperature is increasing with increasing set point temperature except for the first two temperatures. Between the set points of 24-30 °C, it is hard to distinguish the measured temperature difference due to the precision of the measurable temperature suggested in chapter 5.1.3. The increase in sliding speed from 1 to 2 m/s does not affect much the result, since the expected temperature increase (note that both speeds correspond to the hydrodynamic regime) might be again smaller than the measurement precision. Locally, the temperature around the vertical center (i) is higher than its upper- and lower neighbor fields. The longitudinal surface profile of the PRS (Figure 5.12a, right), which is slightly wavy, may account for that. This was undesired but generated during the finishing process. In the contact, the higher part of the profile coincident to the region (i) could yield a local higher friction force and following frictional heat. At some high temperatures, a horizontal boundary (iv), which divides the lower (ii) and higher temperature region (iii), is observed. We think that the edge of the PRS holder (Figure 5.12b-(iv)) might be physically responsible for

this observation. As shown in Figure 5.12b right, the fresh sprayed oil on the liner (blue) may flow more in the region (ii) and its temperature is relatively low due to the insufficient time to be heated in the heater. While the oil that could not pass the small PR/CL gap and gathered on the PRS holder could be heated enough (red) and flow more in the region (iii). The measured temperature distributions at room temperature (Figure 5.11) are consistent with this interpretation, since the boundary (iv) is here inconspicuous.

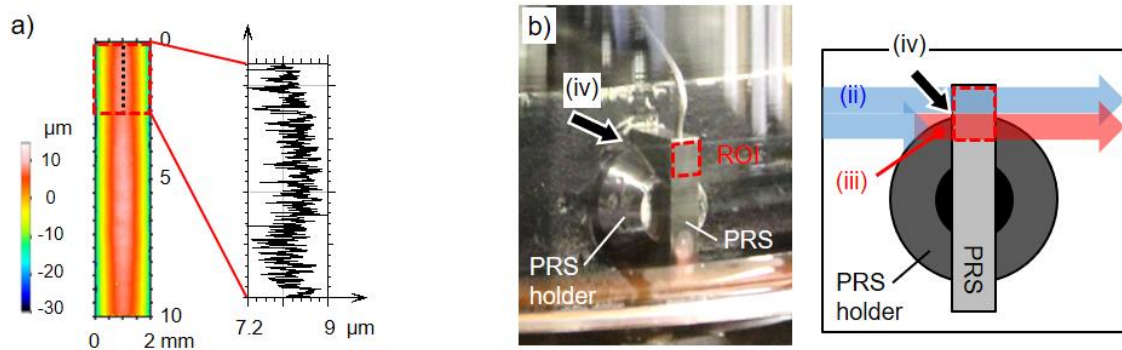


Figure 5.12: a) Contact surface topography of the PRS measured by confocal microscopy (μ Surf, NanoFocus) and the vertical scan along the center line (black dotted line) in the ROI (red dashed box). b) Photo of the PRS and its holder in the optical tribometer during the experiment (left) and its schematic sketch – front view – with different temperatures of oil flows (right).

5.3 Chapter conclusions

In this chapter, proof-of-concept experiments with two-dye fluorescence thermometry using lumilux CD 345/pyrromethene 597 as a dye combination and a blue LED (excitation at around 460 nm) as a light source are discussed. The method is based on the temperature dependency of the intensity ratio detected in the two spectral channels. With the assumption of the optically thin system, this method nullifies the dependence of the intensity ratio on the OFT. In addition, the necessary image processing including the stray light correction was discussed. The temperature sensitivity of the intensity ratio was 0.6 %/K and the estimated measurement uncertainty was ± 2.3 °C.

The experiments on a rotational tribometer, which reproduces the PR/CL sliding contact in an engine, were conducted with a long-distance microscope. The results demonstrate that this method can be employed to visualize the temperature distribution of the oil film in such contact at high magnification even without laser, since the LED has been used as a good alternative light source instead of more expensive and complex lasers, although the emitted light from the LED is incoherent, its output pattern is wider, and its light power is relatively low. Despite some limitations, the result of this chapter has its importance as a proof of the concept, and it offers a possibility of investigating the temperature distribution of a fluid with a relatively uncomplicated experimental setup.

6 Conclusion and future work

This thesis describes quantitative imaging of lubricating oil film thickness and temperature in the sliding contact of the piston-ring/cylinder liner using a laser- (or LED) induced fluorescence technique to better understand the frictional behavior near the top piston ring in a combustion engine. The contact geometry was reproduced in an optical rotational tribometer, in which the oil film was investigated at constant sliding speed while the cylinder liner rotated against a static piston-ring segment. Through a transparent material – either a piston-ring segment or the cylinder liner – the light incident from the light source reached the dyed oil film and its red-shifted fluorescence was detected by a CMOS camera. This LIF image went through a chain of image processing, including flat-field correction, in-situ calibration and stray light estimation, to yield the local oil film thickness. Prior experiments were conducted to characterize each optic system using a laser of 532 nm wavelength with pyromethene 567 dye and a blue LED of about 460 nm with a dye combination of lumilux CD 345/pyromethene 597, the latter combination for temperature imaging.

First, a new optical arrangement was developed, where the metal piston ring segment was replaced with a sapphire one, and this allowed imaging the oil film interacting with the surface texture on conventional cylinder liners, such as microgrooves on a honed gray cast-iron liner and fine pores on a spray-coated liner. Several phenomena in oil lubrication were observed on both liners, for example, the cavitation pattern in the diverging part of the contact gap, and the reverse oil stream adhering only to the piston ring face and flowing in the opposite direction to the liner's sliding direction. From the full-field image of the oil behavior under different operating conditions, i.e., normal load and sliding speed, a smaller contact area for calculating the minimum oil film thickness (OFT) was extracted. The trend showed that the minimum OFT increased with increasing sliding speed. Overall, the OFT on the spray-coated liner was thicker and its decrease with increasing load was less than that with the honed liner. Subsequently measured Stribeck curves also showed an earlier transition between the mixed- and hydrodynamic regime with the spray-coated liner than with the honed one. As other authors have argued [107] [108], this might be because the unconnected pores on the spray-coated liner can retain oil and yield additional hydrodynamic pressure under high load, while the oil in the interconnected, open grooves is more easily displaced.

The second part of this work focused more closely on the effect of fine pores in the liner surface. To figure out the lubrication mechanisms near an individual pore, a quartz liner was laser-textured with a cylindrical pocket representing the pore on the spray-coated liner that rotated against a metal piston ring segment in the tribometer, while a fluorescence microscope allowed imaging the micropore with a high magnification. The results showed the beneficial function of the pore, i.e., it carried oil from the inlet to the starved outlet, creating a downstream “oil tail” whose morphology and volume were analyzed under different sliding speeds and

loads. Specifically, at low speed, the pore produced a wider tail containing a higher oil volume than at high speeds. These results suggest that in a reciprocating piston engine, porosity on the liner can lead to advantageous tribological behavior in particular around the piston-motion reversal points. The effect of different diameters and depths of the pore was studied, which showed that there exists an optimum geometry for the cylindrical pore for the best effectiveness. A subsequent measurement via total internal reflection (TIR) fluorescence supported the results above. The fluorescence microscope was additionally applied to an optical research engine in fired operation. This enabled imaging of the phenomena of the oil film in selected areas from the first land to the piston skirt with high magnification and resolution.

The last part of this thesis work employed an LED as a light source to visualize the temperature in the oil film in the PR/CL contact using a two-color/two-dye ratiometric scheme. The fluorescence intensities from the selected dye combination has different temperature dependencies in two separate spectral bands. The intensity ratio between the spectral bands was linear in temperature with about 0.6 %/K sensitivity and independent from the oil film thickness, since the oil-dye mixture was optically thin. The maximum measurement uncertainty was ± 2.3 °C. The results from the measurement in the heated tribometer showed local differences in the temperature throughout the contact, which were attributed to the interplay of friction heat and cooling by the circulating oil.

With the developed optical measurement method and numerous interesting results in this work, some possibilities arise to extend this research. In the case of the textured micropore on the quartz liner, the optimum geometric parameter set of the pore happened to be at the boundary of the available parameter variations due to the texturing capabilities. More variation beyond this limit would be interesting to investigate the different oil film behaviors over this optimum region and obtain more general insight into how to optimize a surface texture for a given circumstance. Furthermore, the application of the fluorescence microscopy to the optical single-cylinder engine and its initial results with the high spatial resolution suggest a number of uses, such as a not only qualitative, but also quantitative imaging of the microscopic oil film behaviors with various piston rings. For example, for the oil control ring, a detailed view of the oil film in the rail-liner interface for the whole cycle and that in the rail/groove clearance would be helpful for simulation model verification and better understanding of the dynamics of the rails and expander. In addition, for the temperature imaging, a single camera captured two series of fluorescence images sequentially while the BP (blue channel) and LP (red channel) filters are changed in the filter wheel. With the reason, this system was limited to examine steady state flows, however, the employment of two cameras would allow the simultaneous image acquisition in two channels and enable studying transient flows as well.

7 References

- [1] K. Holmberg, P. Andersson und A. Erdemir, „Global energy consumption due to friction in passenger cars,“ *Tribology International*, Bd. 47, pp. 221-234, 2012.
- [2] C. Arcoumanis, M. Duszynski, H. Lindenkamp und H. Preston, „Measurements of the Lubricant Film Thickness in the Cylinder of a Firing Diesel Engine Using LIF,“ *SAE Transactions*, Bd. 107, pp. 898-906, 1998.
- [3] G. Ryk, Y. Kligerman, I. Etsion und A. Shinkarenko, „Experimental Investigation of Partial Laser Surface Texturing for Piston-Ring Friction Reduction,“ *Tribology Transactions*, Bd. 48, Nr. 4, pp. 583-588, 2005.
- [4] H. Rahnejat, S. Balakrishnan, P. King und S. Howell-Smith, „In-Cylinder Friction Reduction Using a Surface Finish Optimization Technique,“ *Proceedings of the Institution of Mechanical Engineers, Part D: Journal of Automobile*, Bd. 220, Nr. 9, pp. 1309-1318, 2006.
- [5] B. Bhushan, *Introduction to Tribology*, 2. Hrsg., Wiley, 2013.
- [6] Gesellschaft für Tribologie (GfT), *GfT Arbeitsblatt 7 - Tribologie Definitionen, Begriffe, Prüfung*, 2002.
- [7] H. Czichos und K.-H. Habig, *Tribologie-Handbuch*, 4 Hrsg., Springer Vieweg, 2015.
- [8] V. L. Popov, *Kontaktmechanik und Reibung*, 2 Hrsg., Springer-Verlag Berlin Heidelberg, 2010.
- [9] L. Deters, „Reibung, Verschleiß und Schmierung,“ in *Konstruktionselemente des Maschinenbaus 2*, Springer, Berlin, Heidelberg, 2008, pp. 1-68.
- [10] T. Yamamoto und D. Buckley, „Wear Mechanism Based on Adhesion,“ *NASA Technical Paper 2037*, 1982.
- [11] R. Stribeck, „Kugellager für beliebige Belastungen (Ball Bearings for any Stress),“ *Zeitschrift des Vereins Deutscher Ingenieure*, Bd. 45, 1901.
- [12] R. Stribeck, „Die wesentlichen Eigenschaften der Gleit- und Rollenlager (Characteristics of Plain and Roller Bearings),“ *Zeitschrift des Vereines Deutscher Ingenieure*, Bd. 46, pp. 1432-1438, 1463-1470, 1902.

- [13] L. Gümbel, „Das Problem der Lagerreibung,“ *Mitteilungsblatt des Berliner Bezirksvereins Deutscher Ingenieure*, pp. 87-104, 109-120, 1914.
- [14] M. Hersey, „The laws of lubrication of horizontal journal bearings,“ *J. Washington Acad. Sci.*, Bd. 4, pp. 542-552, 1914.
- [15] Y. Wakuri, M. Soejima, Y. Ejima, T. Hamatake und T. Kitahara, „Studies on Friction Characteristics of Reciprocating Engines,“ *SAE Technical Paper 952471*, 1995.
- [16] C. Arcoumanis, P. Ostovar und R. Mortier, „Mixed Lubrication Modeling of Newtonian and Shear Thinning Liquids in a Piston-Ring Configuration,“ *SAE Technical Paper 972924*, 1997.
- [17] R. Coy, „Practical applications of lubrication models in engines,“ *Tribology International*, Bd. 31, Nr. 10, pp. 563-571, 1998.
- [18] S. Wigger, *Charakterisierung von Öl- und Kraftstoffschichten in der Kolbengruppe mittels laserinduzierter Fluoreszenz*, PhD Thesis, Fakultät für Ingenieurwissenschaften, Abteilung Maschinenbau und Verfahrenstechnik, Duisburg-Essen University, 2014.
- [19] M. Wattrus, „Fuel property effects on oil dilution in diesel engines,“ *SAE International Journal of Fuels and Lubricants*, Bd. 6, pp. 794-806, 2013.
- [20] Federal-Mogul, *GOETZE Piston Ring Handbook*, Burscheid, 2003.
- [21] V. D'Agostino und A. Senatore, „10 - Fundamentals of lubrication and friction of piston ring contact,“ in *Tribology and Dynamics of Engine and Powertrain*, Woodhead Publishing, 2010, pp. 343-386.
- [22] I. Sherrington, „11 - Measurement techniques for piston-ring tribology,“ in *Tribology and Dynamics of Engine and Powertrain*, Woodhead Publishing, 2010, pp. 387-425.
- [23] F. Welzel, *Tribologische Optimierung von Zylinderlaufflächen in Verbrennungsmotoren aus fertigungstechnischer Sicht*, Fakultät für Maschinenbau, Otto-von-Guericke-Universität Magdeburg, 2014.
- [24] M. Schmidt, H. Spieth, C. Haubach, C. Kühne und N. P. Chain, *100 Pioneers for Efficient Resource Management*, Berlin: Springer, 2019.
- [25] J. König, M. Lahres und O. Methner, „Quality Designed Twin Wire Arc Spraying of Aluminum Bores,“ *International Thermal Spray Conference*, Bd. JTTEE5 24, pp. 63-74, 2014.

- [26] J. Schommers, H. Scheib, M. Hartweg und A. Bosler, „Minimising Friction in Combustion Engines,“ *MTZ Worldwide*, Bd. 74, pp. 28-35, 2013.
- [27] DIN EN 657:2005-06, *Thermal spraying - Terminology, classification*, Beuth, 2005.
- [28] S. Parkash, *Petroleum Fuels Manufacturing Handbook: Including Specialty Products and Sustainable Manufacturing Techniques*, The McGraw-Hill Companies, Inc., 2010.
- [29] K. Dieter, *Lubricants and Related Products: Synthesis, Properties, Applications, International Standards*, Weinheim: Verlag Chemie, 1984.
- [30] M. Sauer, J. Hofkens und J. Enderlein, „Basic Principles of Fluorescence Spectroscopy,“ in *Handbook of Fluorescence Spectroscopy and Imaging: From Single Molecules to Ensembles*, Wiley-VCH Verlag GmbH & Co. KGaA, 2011.
- [31] J. R. Lakowicz, *Principles of Fluorescence Spectroscopy*, 3. Hrsg., Springer, Boston, 2006.
- [32] A. Jablonski, „Efficiency of Anti-Stokes Fluorescence in Dyes,“ *Nature*, Bd. 131, pp. 839-840, 1933.
- [33] Y. Yang, G. Qian, D. Su und M. Wang, „Photostability of pyrromethene 567 doped in ORMOSILs with various additives,“ *Optics Communications*, Bd. 239, pp. 415-420, 2004.
- [34] A. Penzkofer und W. Leupacher, „Fluorescence behaviour of highly concentrated rhodamine 6G solutions,“ *Lumin*, Bd. 37, Nr. 2, pp. 61-72, 1987.
- [35] Y. Zhu und O. C. Mullins, „Temperature dependence of fluorescence of crude oils and related compounds,“ *Energy Fuels*, Bd. 6, Nr. 5, pp. 545-552, 1992.
- [36] P. Baj, P. Bruce und O. Buxton, „On a PLIF quantification methodology in a nonlinear dye response regime,“ *Exp Fluids*, Bd. 57, Nr. 106, 2016.
- [37] B. Thirouard, *Characterization and Modeling of the Fundamental Aspects of Oil Transport in the Piston Ring Pack of Internal Combustion Engines*, PhD Thesis, Massachusetts Institute of Technology, 2001.
- [38] C. H. Hidrovo und D. P. Hart, „2D thickness and temperature mapping of fluids by means of a two-dye laser induced fluorescence ratiometric scheme,“ *Journal of Flow Visualization & Image Processing*, Bd. 9, pp. 171-191, 2002.

- [39] A. Vokac und T. Tian, „An Experimental Study of Oil Transport on the Piston Third Land and the Effects of Piston and Ring Designs,“ *SAE Technical Paper 2004-01-1934*, 2004.
- [40] M. Kato, T. Ishima und T. Obokata, „Measurement techniques of lubricant oil film behavior on the piston surface based on LIF and PIV,“ *15th Int Symp on Applications of Laser Techniques to Fluid Mechanics*, 2010.
- [41] M. Fowell, C. Myant, S. H.A. und A. Kadiric, „A study of lubricant film thickness in compliant contacts of elastomeric seal materials using a laser induced fluorescence technique,“ *Tribology International*, Bd. 80, pp. 76-89, 2014.
- [42] T. Müller, *Simultane Visualisierung von Öl- und Kraftstoffschichten in der Kolbengruppe eines direkteinspritzenden Ottomotors durch laserinduzierte Fluoreszenz*, PhD Thesis, Universität Duisburg-Essen, 2018.
- [43] K. Nambiar, *Lasers: Principles, Types and Applications*, New Age International (P) Limited, 2006.
- [44] H. J. Eichler und J. Eichler, *Laser*, Springer-Verlag Berlin Heidelberg, 2010.
- [45] E. F. Schubert, *Light-Emitting Diodes*, 4th Edition ed., E. Fred Schubert, 2023.
- [46] W. Eagle, L. Malbec und M. Musculus, „Measurements of Liquid Length, Vapor Penetration, Ignition Delay, and Flame Lift-Off Length for the Engine Combustion Network ‘Spray B’ in a 2.34 L Heavy-Duty Optical Diesel Engine,“ *SAE International Journal of Engines*, Bd. 9, Nr. 2, pp. 910-931, 2016.
- [47] P. Kranz, *Imaging of mixing processes in spark-ignition engines via quantitative laser-induced fluorescence*, PhD Thesis, Fakultät für Ingenieurwissenschaften, Abteilung Maschinenbau und Verfahrenstechnik, Duisburg-Essen University, 2020.
- [48] F. Westlye, K. Penney, A. Ivarsson, L. Pickett, J. Manin und S. Skeen, „Diffuse back-illumination setup for high temporally resolved extinction imaging,“ *Applied Optics*, Bd. 56, Nr. 17, pp. 5028-5038, June 2017.
- [49] J. Manin, M. Bardi und L. Pickett, „Evaluation of the liquid length via diffused back-illumination imaging in vaporizing diesel sprays,“ *Proceedings of the 8th International Conference on Modeling and Diagnostics for Advanced Engine Systems, COMODIA*, pp. 665-673, 2012.

- [50] S. Wilson, G. Gustafson, D. Lincoln, K. Murari und C. Johansen, „Performance evaluation of an overdriven LED for high-speed schlieren imaging,“ *Journal of Visualization*, Bd. 18, pp. 35-45, 2015.
- [51] S. Skeen, J. Manin und L. Pickett, „Simultaneous formaldehyde PLIF and high-speed schlieren imaging for ignition visualization in high-pressure spray flames,“ *Proceedings of the Combustion Institute*, Bd. 35, Nr. 3, pp. 3167-3174, 2015.
- [52] C. H. Hidrovo und D. P. Hart, „Emission reabsorption laser induced fluorescence (ERLIF) film thickness measurement,“ *Measurement Science and Technology*, Bd. 12, Nr. 4, pp. 467-477, 2001.
- [53] G. Hamilton und S. Moore, „Measurement of the Oil-Film Thickness between the Piston Rings and Liner of a Small Diesel Engine,“ *Proceedings of the Institution of Mechanical Engineers*, Bd. 188, Nr. 1, pp. 253-261, 1974.
- [54] K. Shin, Y. Tateishi und S. Furuhashi, „Measurement of oil film thickness between piston-ring and cylinder,“ *SAE paper 830068*, 1983.
- [55] S. Brown und G. Hamilton, „The partially lubricated piston-ring,“ *J. Mech. Eng. Sci.*, Bd. 19, Nr. 2, pp. 81-89, 1977.
- [56] S. Moore und G. Hamilton, „The Starved Lubrication of Piston Rings in a Diesel Engine,“ *Journal of Mechanical Engineering Science*, Bd. 20, Nr. 6, pp. 345-352, 1978.
- [57] S. Moore und G. Hamilton, „The Piston Ring at Top Dead Centre,“ *Proc. I. Mech. E.*, Bd. 194, Nr. 1, pp. 373-381, 1980.
- [58] C. Mattsson, „Measurement of the Oil Film Thickness Between the Cylinder Liner and the Piston Rings in a Heavy Duty Directly Injected Diesel Engine,“ *SAE Technical Paper 952469*, 1995.
- [59] R. Wing und O. Saunders, „Oil-film temperature and thickness measurements on the piston-rings of a diesel engine,“ *Proc. I. Mech. E.*, Bd. 186, Nr. 1, pp. 1-9, 1972.
- [60] T. Dow, C. Schiele und R. Stockwell, „Technique for experimental evaluation of piston-ring/cylinder film thickness,“ *J. Lubr. Technol.*, Bd. 105, Nr. 3, pp. 353-360, 1983.
- [61] J. Tamminen, C.-E. Sandström und P. Andersson, „Influence of load on the tribological conditions in piston ring and cylinder liner contacts in a medium-speed diesel engine,“ *Tribology International*, Bd. 39, Nr. 12, pp. 1643-1652, 2006.

- [62] J. Courtney-Pratt und G. Tudor, „An Analysis of the Lubrication between the Piston Rings and Cylinder Wall of a Running Engine,“ *Proc Inst Mech Eng*, Bd. 155, Nr. 1, pp. 293-299, 1946.
- [63] S. Furuhashi und T. Sumi, „A dynamic theory of piston-ring lubrication, 3rd report: measurement of oil-film thickness,“ *Jsmc International Journal Series B-fluids and Thermal Engineering*, Bd. 4, pp. 744-752, 1961.
- [64] P. Saad, L. Kamo, M. Mekari, W. Bryzik, V. Wong, N. Dmitrichenko und R. Mnatsakanov, „Modeling and Measurement of Tribological Parameters Between Piston Rings and Liner in Turbocharged Diesel Engine,“ *SAE Technical Paper 2007-01-1440*, 2007.
- [65] Y. Wakuri, S. Ono, M. Soejima und N. Woguchi, „Oil-Film Behaviour of Reciprocating Slider with Circular Profile : Observation of Oil-Film by Means of Thin-Film Interferometry,“ *Bulletin of JSME*, Bd. 22, Nr. 167, pp. 755-762, 1979.
- [66] Y. Wakuri, S. Ono, M. Soejima und K. Masuda, „Oil-film Behaviour of Reciprocating Slider with Circular Profile : Optical Measurement of Oil-film Separation Boundary,“ *Bulletin of JSME*, Bd. 24, Nr. 194, pp. 1462-1469, 1981.
- [67] J. Luo, S. Wen und P. Huang, „Thin film lubrication. Part I. Study on the transition between EHL and thin film lubrication using a relative optical interference intensity technique,“ *Wear*, Bd. 194, Nr. 1-2, pp. 107-115, 1996.
- [68] I. Krupka und M. Hartl, „The effect of surface texturing on thin EHD lubrication films,“ *Tribology International*, Bd. 40, Nr. 7, pp. 1100-1110, 2007.
- [69] S. Vladescu, S. Medina, A. Olver, I. Pegg und T. Reddyhoff, „Lubricant film thickness and friction force measurements in a laser surface textured reciprocating line contact simulating the piston ring–liner pairing,“ *Tribology International*, Bd. 98, pp. 317-329, 2016.
- [70] G. Poll, A. Gabelli, P. Binnington und J. Qu, „Dynamic Mapping of Rotary Lip Seal Lubricant Films by Fluorescent Image Processing,“ *Fluid Sealing. Fluid Mechanics and its Applications*, Bd. 8, pp. 55-77, 1992.
- [71] J. Dearlove und W. Cheng, „Simultaneous Piston Ring Friction and Oil Film Thickness Measurements in a Reciprocating Test Rig,“ *SAE Technical Paper 952470*, 1995.

- [72] J. Sugimura, M. Hashimoto und Y. Yamamoto, „Study of elastohydrodynamic contacts with fluorescence microscope,“ *Tribology Series*, Bd. 38, pp. 609-617, 2000.
- [73] C. Myant, T. Reddyhoff und H. Spikes, „Laser-induced fluorescence for film thickness mapping in pure sliding lubricated, compliant, contacts,“ *Tribology International*, Bd. 43, pp. 1960-1969, 2010.
- [74] S.-C. Vladescu, A. V. Olver, I. G. Pegg und T. Reddyhoff, „The effects of surface texture in reciprocating contacts – An experimental study,“ *Tribology International*, Bd. 82, pp. 28-42, 2015.
- [75] B. Yin, X. Li, Y. Fu und W. Yun, „Effect of laser textured dimples on the lubrication performance of cylinder liner in diesel engine,“ *Lubrication Science*, Bd. 24, pp. 293-312, 2012.
- [76] S. Wigger, H.-J. Füzser, D. Fuhrmann, C. Schulz und S. A. Kaiser, „Quantitative two-dimensional measurement of oil-film thickness by laser-induced fluorescence in a piston-ring model experiment,“ *Applied Optics*, Bd. 55, pp. 269-279, 2016.
- [77] P. Obert, H.-J. Füzser und D. Bartel, „Oil distribution and oil film thickness within the piston ring-liner contact measured by laser-induced fluorescence in a reciprocating model test under starved lubrication conditions,“ *Tribology International*, Bd. 129, pp. 191-201, 2019.
- [78] A. Greene, „Initial visual studies of piston-cylinder dynamic oil film behaviour,“ *Wear*, Bd. 13, Nr. 4-5, pp. 345-360, 1969.
- [79] L. Ting, „Development of a Laser Fluorescence Technique For Measuring Piston Ring Oil Film Thickness,“ *Journal of Lubrication Technology*, Bd. 102, Nr. 2, pp. 165-170, 1980.
- [80] D. Hoult, J. Lux, V. Wong und S. Billian, „Calibration of Laser Fluorescence Measurements of Lubricant Film Thickness in Engines,“ *SAE Transactions*, Bd. 97, pp. 576-584, 1988.
- [81] D. Richardson und G. Borman, „Using Fiber Optics and Laser Fluorescence for Measuring Thin Oil Films with Application to Engines,“ *SAE Technical Paper 912388*, 1991.
- [82] R. Phen, D. Richardson und G. Borman, „Measurements of Cylinder Liner Oil Film Thickness in a Motored Diesel Engine,“ *SAE Technical Paper 932789*, 1993.

- [83] K. Nakayama, S. Tamaki, H. Miki und M. Takiguchi, „The Effect of Crankshaft Offset on Piston Friction Force in a Gasoline Engine,“ *SAE Technical Paper 2000-01-0922*, 2000.
- [84] H. Inagaki, A. Saito, M. Murakami und T. Konomi, „Development of Two-Dimensional Oil Film Thickness Distribution Measuring System,“ *SAE Technical Paper 952346*, 1995.
- [85] B. Thirouard, T. Tian und D. Hart, „Investigation of Oil Transport Mechanisms in the Piston Ring Pack of a Single Cylinder Diesel Engine, Using Two Dimensional Laser Induced Fluorescence,“ *SAE Technical Paper 982658*, 1998.
- [86] D. Thirouard und D. Hart, „Investigation of Oil Transport Mechanisms on the Piston Second Land of a Single Cylinder Diesel Engine, Using Two-Dimensional-Laser-Induced Fluorescence,“ *Laser Techniques Applied to Fluid Mechanics*, pp. 487-503, 2000.
- [87] B. Thirouard und T. Tian, „Oil Transport in the Piston Ring Pack (Part I): Identification and Characterization of the Main Oil Transport Routes and Mechanisms,“ *SAE Technical Paper 2003-01-1952*, 2003.
- [88] S. Przesmitzki, A. Vokac und T. Tian, „An Experimental Study of Oil Transport between the Piston Ring Pack and Cylinder Liner,“ *SAE Technical Paper 2005-01-3823*, 2005.
- [89] S. Przesmitzki und T. Tian, „Oil Transport Inside the Power Cylinder During Transient Load Changes,“ *SAE Technical Paper 2007-01-1054*, 2007.
- [90] T. Müller, S. Wigger, H.-J. Füller und S. Kaiser, „Development of a LIF-Imaging System for Simultaneous High-Speed Visualization of Liquid Fuel and Oil Films in an Optically Accessible DISI Engine,“ *SAE Technical Paper 2018-01-0634*, 2018.
- [91] J. Schöler, S. Schiefer, S. Wigger, H.-J. Füller, V. Lagemann und S. Kaiser, „Imaging and Simulation of Oil Transport Phenomena in the Upper Piston Skirt Region,“ *SAE Technical Paper 2019-01-2359*, 2019.
- [92] D. Hamilton, J. Walowit und C. Allen, „A Theory of Lubrication by Microirregularities,“ *ASME. J. Basic Eng.*, Bd. 88, Nr. 1, pp. 177-185, March 1966.
- [93] I. Etsion und L. Burstein, „A Model for Mechanical Seals with Regular Microsurface Structure,“ *Tribology Transactions*, Bd. 39, Nr. 3, pp. 677-683, 1996.

- [94] H. Costa und I. Hutchings, „Hydrodynamic lubrication of textured steel surfaces under reciprocating sliding conditions,“ *Tribology International*, Bd. 40, Nr. 8, pp. 1227-1238, 2007.
- [95] I. Etsion, „State of the Art in Laser Surface Texturing,“ *ASME. J. Tribol.*, Bd. 127, Nr. 1, pp. 248-253, 2005.
- [96] I. Etsion, Y. Kligerman und G. Halperin, „Analytical and Experimental Investigation of Laser-Textured Mechanical Seal Faces,“ *Tribology Transactions*, Bd. 42, pp. 511-516, 1999.
- [97] A. Ronen, I. Etsion und Y. Kligerman, „Friction-Reducing Surface-Texturing in Reciprocating Automotive Components,“ *Tribology Transactions*, Bd. 44, Nr. 3, pp. 359-366, 2001.
- [98] A. Olver, M. Fowell, H. Spikes und I. Pegg, ‚Inlet suction‘, a load support mechanism in non-convergent, pocketed, hydrodynamic bearings,“ *Journal of Engineering Tribology*, Bd. 220, Nr. 2, pp. 105-108, 2006.
- [99] M. Fowell, A. Olver, A. Gosman, H. Spikes und I. Pegg, „Entrainment and inlet suction: Two mechanism of hydrodynamic lubrication in textured bearings,“ *Journal of tribology*, Bd. 129, pp. 336-347, 2007.
- [100] P. Lu, R. Wood, M. Gee, L. Wang und W. Pfleging, „A novel surface texture shape for directional friction control,“ *Tribology Letters*, Bd. 66, Nr. 1, 2018.
- [101] P. G. Grützmaier, F. J. Profito und A. Rosenkranz, „Multi-Scale Surface Texturing in Tribology—Current Knowledge and Future Perspectives,“ *Lubricants*, Bd. 7, Nr. 95, 2019.
- [102] A. Borghi, E. Gualtieri, D. Marchetto, L. Moretti und S. Valeri, „Tribological effects of surface texturing on nitriding steel for high-performance engine applications,“ *Wear*, Bd. 265, Nr. 7-8, pp. 1046-1051, 2008.
- [103] M. Varenberg, G. Halperin und I. Etsion, „Different aspects of the role of wear debris in fretting wear,“ *Wear*, Bd. 252, Nr. 11-12, pp. 902-910, 2002.
- [104] H. Yamakiri, S. Sasaki, T. Kurita und N. Kasashima, „Effects of laser surface texturing on friction behavior of silicon nitride under lubrication with water,“ *Tribology International*, Bd. 44, Nr. 5, pp. 579-584, 2011.

- [105] C. Shen und M. M. Khonsari, „Tribological and Sealing Performance of Laser Pocketed Piston Rings in a Diesel Engine,“ *Tribology Letters*, Bd. 64, 2016.
- [106] J. Schneider, D. Braun und C. Greiner, „Laser Textured Surfaces for Mixed Lubrication: Influence of Aspect Ratio, Textured Area and Dimple Arrangement,“ *Lubricants*, Bd. 5, Nr. 32, pp. 1-12, 2017.
- [107] K.-H. Zum Gahr, R. Wahl und K. Wauthier, „Experimental study of the effect of microtexturing on oil lubricated ceramic/steel friction pairs,“ *Wear*, vol. 267, pp. 1241-1251, 2009.
- [108] W. Grabon, W. Koszela, P. Pawlus und S. Ochwat, „Improving tribological behaviour of piston ring–cylinder liner frictional pair by liner surface texturing,“ *Tribology International*, Bd. 61, pp. 102-108, 2013.
- [109] C. Shen und M. Khonsari, „Texture Shape Optimization for Seal-Like Parallel Surfaces: Theory and Experiment,“ *Tribology Transactions*, Bd. 59, Nr. 4, pp. 698-706, 2016.
- [110] Y. Qiu und M. Khonsari, „Experimental investigation of tribological performance of laser textured stainless steel rings,“ *Tribology International*, Bd. 44, Nr. 5, pp. 635-644, 2011.
- [111] C. Ma, J. Sun, Y. Wang, B. Yu, Q. Yu und Q. Tu, „On the optimum dimple depth-over-diameter ratio for textured surfaces,“ *Advances in Mechanical Engineering*, Bd. 9, Nr. 9, pp. 1-8, 2017.
- [112] X. Wang, K. Kato, K. Adachi und K. Aizawa, „The effect of laser texturing of SiC surface on the critical load for the transition of water lubrication mode from hydrodynamic to mixed,“ *Tribology International*, Bd. 34, Nr. 10, pp. 703-711, 2001.
- [113] T. Hu und L. Hu, „The study of tribological properties of laser-textured surface of 2024 aluminium alloy under boundary lubrication,“ *Lubrication Science*, Bd. 24, Nr. 2, pp. 84-93, 2012.
- [114] D. Segu, S. Choi, J. Choi und S. Kim, „The effect of multi-scale laser textured surface on lubrication regime,“ *Applied Surface Science*, Bd. 270, pp. 58-63, 2013.
- [115] S. Hill, T. Kantola, J. Brown und J. Hamelink, „An Experimental Study of the Effect of Cylinder Bore Finish on Engine Oil Consumption,“ *SAE Technical Paper 950938*, 1995.
- [116] S. Hill, „Cylinder Bore Finishes and Their Effect on Oil Consumption,“ *SAE Transactions*, Bd. 110, pp. 1862-1881, 2001.

- [117] O. Sato, M. Takiguchi, T. Aihara, Y. Seki, K. Fujimura und Y. Tateishi, „Improvement of Piston Lubrication in a Diesel Engine By Means of Cylinder Surface Roughness,“ *SAE Paper 2004-01-0604*, 2004.
- [118] D. Srivastava, A. Agarwal und J. Kumar, „Effect of liner surface properties on wear and friction in a non-firing engine simulator,“ *Materials & Design*, Bd. 28, Nr. 5, pp. 1632-1640, 2007.
- [119] S. Johansson, P. Nilsson, R. Ohlsson, C. Anderberg und B. Rosen, „New cylinder liner surfaces for low oil consumption,“ *Tribology International*, Bd. 41, Nr. 9-10, pp. 854-859, 2008.
- [120] M. Yousfi, S. Mezghani, I. Demirci and M. El Mansori, "Smoothness and plateauness contributions to the running-in friction and wear of stratified helical slide and plateau honed cylinder liners," *Wear*, Vols. 332-333, pp. 1238-1247, 2015.
- [121] S. Michail und G. Barber, „The Effects of Roughness on Piston Ring Lubrication—Part II: The Relationship between Cylinder Wall Surface Topography and Oil Film Thickness,“ *Tribology Transactions*, Bd. 38, Nr. 1, pp. 173-177, 1995.
- [122] J. Jocsak, Y. Li, T. Tian und V. Wong, „Modeling and Optimizing Honing Texture for Reduced Friction in Internal Combustion Engines,“ *SAE Technical Paper 2006-01-0647*, 2006.
- [123] N. Bolander und F. Sadeghi, „Deterministic Modeling of Honed Cylinder Liner Friction,“ *Tribology Transactions*, Bd. 50, pp. 248-256, 2007.
- [124] A. Spencer, A. Almqvist und R. Larsson, „A numerical model to investigate the effect of honing angle on the hydrodynamic lubrication between a combustion engine piston ring and cylinder liner,“ *Proceedings of the Institution of Mechanical Engineers, Part J: Journal of Engineering Tribology*, Bd. 225, Nr. 7, pp. 683-689, 2011.
- [125] W. Grabon, P. Pawlus, S. Wos, W. Koszela und M. Wieczorowski, „Effects of honed cylinder liner surface texture on tribological properties of piston ring-liner assembly in short time tests,“ *Tribology International*, Bd. 113, pp. 137-148, 2017.
- [126] S.-C. Vladescu, A. Ciniero, K. Tufail, A. Gangopadhyay und T. Reddyhoff, „Looking into a laser textured piston ring-liner contact,“ *Tribology International*, Bd. 115, pp. 140-153, 2017.

- [127] F. J. Profito, S.-C. Vladescu, T. Reddyhoff und D. Dini, „Transient experimental and modelling studies of laser-textured microgrooved surfaces with a focus on piston-ring cylinder liner contacts,“ *Tribology International*, vol. 113, pp. 125-136, 2017.
- [128] H. Checo, R. Ausas, M. Jai, J. Cadalen, F. Choukroun und G. Buscaglia, „Moving textures: Simulation of a ring sliding on a textured liner,“ *Tribology International*, Bd. 72, pp. 131-142, 2014.
- [129] W. Koszela, P. Pawlus, R. Reizer und T. Liskiewicz, „The combined effect of surface texturing and DLC coating on the functional properties of internal combustion engines,“ *Tribology International*, Bd. 127, pp. 470-477, 2018.
- [130] T. Nakajima, M. Utsunomiya und Y. Ikada, „Simultaneous Measurement of Velocity and Temperature of Water Using LDV and Fluorescence Technique,“ *Applications of Laser Techniques to Fluid Mechanics*, pp. 34-53, 1991.
- [131] J. Sakakibara, K. Hishida und M. Maeda, „Measurements of thermally stratified pipe flow using image-processing techniques,“ *Experiments in Fluids*, Bd. 16, pp. 82-96, 1993.
- [132] F. Lemoine, Y. Antoine, M. Wolff und M. Lebouche, „Simultaneous temperature and 2D velocity measurements in a turbulent heated jet using combined laser-induced fluorescence and LDA,“ *Experiments in Fluids*, Bd. 26, pp. 315-323, 1999.
- [133] O. Auban, F. Lemoine, P. Vallette und J. Fontaine, „Simulation by solutal convection of a thermal plume in a confined stratified environment: application to displacement ventilation,“ *International Journal of Heat and Mass Transfer*, Bd. 44, Nr. 24, pp. 4679-4691, 2001.
- [134] W. Chaze, O. Caballina, G. Castanet und F. Lemoine, „The saturation of the fluorescence and its consequences for laser-induced fluorescence thermometry in liquid flows,“ *Experiments in Fluids*, Bd. 57, Nr. 58, 2016.
- [135] P. Lavieille, F. Lemoine, G. Lavergne und M. Lebouche, „Evaporating and combusting droplet temperature measurements using two-color laser-induced fluorescence,“ *Experiments in Fluids*, Bd. 31, pp. 45-55, 2001.
- [136] M. M. Prenting, M. I. Dzulfida, T. Dreier und C. Schulz, „Characterization of tracers for two-color laser-induced fluorescence liquid-phase temperature imaging in sprays,“ *Experiments in Fluids*, Bd. 61, p. 77, 2020.

- [137] P. Lavieille, F. Lemoine und M. Lebouche, „Investigation on temperature of evaporating droplets in linear stream using two-color laser-induced fluorescence,“ *Combustion Science and Technology*, Bd. 174, Nr. 4, pp. 117-142, 2002.
- [138] G. Castanet, P. Lavieille, F. Lemoine und M. Lebouche, „Measurement of the temperature distribution within monodisperse combusting droplets in linear streams using two-color laser-induced fluorescence,“ *Experiments in Fluids*, Bd. 35, pp. 563-571, 2003.
- [139] M. Bruchhausen, F. Guillard und F. Lemoine, „Instantaneous measurement of two-dimensional temperature distributions by means of two-color planar laser induced fluorescence (PLIF),“ *Experiments in Fluids*, Bd. 38, pp. 123-131, 2005.
- [140] J. Sutton, B. Fisher und J. Fleming, „A laser-induced fluorescence measurement for aqueous fluid flows with improved temperature sensitivity,“ *Experiments in Fluids*, Bd. 45, pp. 869-881, 2008.
- [141] J. Sakakibara und R. Adrian, „Whole field measurement of temperature in water using two-color laser induced fluorescence,“ *Experiments in Fluids*, Bd. 26, pp. 7-15, 1999.
- [142] H. Kim, K. Kihm und J. Allen, „Examination of ratiometric laser induced fluorescence thermometry for microscale spatial measurement resolution,“ *International Journal of Heat and Mass Transfer*, Bd. 46, Nr. 21, pp. 3967-3974, 2003.
- [143] T. Kan, H. Aoki, N. Binh-Khiem, K. Matsumoto und I. Shimoyama, „Ratiometric Optical Temperature Sensor Using Two Fluorescent Dyes Dissolved in an Ionic Liquid Encapsulated by Parylene Film,“ *Sensors*, Bd. 13, Nr. 4, pp. 4138-4145, 2013.
- [144] W. Chaze, O. Caballina, G. Castanet und F. Lemoine, „Spatially and temporally resolved measurements of the temperature inside droplets impinging on a hot solid surface,“ *Experiments in Fluids*, Bd. 58, p. 96, 2017.
- [145] A. J. Fenner, *Two-Color/Two-Dye Planar Laser-Induced Fluorescence Thermography for Temperature Measurements at an Evaporating Meniscus*, Darmstadt: Technische Universität Darmstadt, 2017.
- [146] J. An, *Bestimmung der Schmierungs- und Reibungsverhältnisse im Kontakt Kolbenring gegen Zylinderlaufbahn von Verbrennungsmotoren in einem Modelltribometer*, Fakultät für Maschinenbau der Ruhr-Universität Bochum, 2014.

- [147] International Organisation for Standardisation (ISO), *ISO 25178: Geometric Product Specifications (GPS) – Surface texture: Areal*, 2012.
- [148] LaVision GmbH, *1004072_PTU9_D72 (Product-Manual)*, Göttingen: LaVision GmbH, 2007.
- [149] Semrock, „532 nm laser BrightLine single-edge laser dichroic beamsplitter,“ Semrock, [Online]. Available: <https://www.semrock.com/filters.aspx?id=505,537&page=3&so=0&recs=10>. [Zugriff am August 2019].
- [150] Semrock, „572/15 nm BrightLine® single-band bandpass filter transmission spectra,“ [Online]. Available: <https://www.semrock.com/filterdetails.aspx?id=ff01-572/15-25>. [Zugriff am May 2019].
- [151] D. Fuhrmann, T. Benzler, S. Fernando, T. Endres, T. Dreier, S. Kaiser und C. Schulz, „Self-quenching in toluene LIF,“ *Proceedings of the Combustion Institute*, Bd. 36, Nr. 3, pp. 4505-4514, 2017.
- [152] A. Eckbreth, „Laser Diagnostics for Combustion Temperature and Species,“ in *Unsteady Combustion*, Springer, Dordrecht, 1996, pp. 393-410.
- [153] J. Kiefer, Z. Li, T. Seeger, A. Leipertz und M. Alden, „Planar laser-induced fluorescence of HCO for instantaneous flame front imaging in hydrocarbon flames,“ *Proceedings of the Combustion Institute*, Bd. 32, Nr. 1, pp. 921-928, 2009.
- [154] V. A. Miller, „Quantifying and correcting for contamination of PLIF images due to background signals,“ *Exp Fluids*, Bd. 54, pp. 1-12, 2013.
- [155] P. Obert, *Fressverhalten der reibpaarung Kolbenring gegen zylinderlaufbahn*, Magdeburg: Otto-von-Guericke-University, 2018.
- [156] D. Bartel, *Simulation von Tribosystemen - Grundlagen und Anwendungen vol.1*, Wiesbaden: Vieweg + Teubner Verlag, 2010.
- [157] A. Dhunput, *Oil Transport in Piston Ring Assemblies*, London: Department of Mechanical Engineering and Aeronautics, University of London, 2009.
- [158] A. Cameron, *Basic lubrication theory*, Longman, 1971.

- [159] M. Priest, D. Dowson und C. Taylor, „Theoretical modelling of cavitation in piston ring lubrication,“ *Journal of Mechanical Engineering Science*, vol. 214, pp. 435-447, March 2000.
- [160] J. M. Nouri, I. Vasilakos, Y. Yan und C.-C. Reyes-Aldasoro, „Effect of viscosity and speed on oil cavitation development in a single piston-ring lubricant assembly,“ *Lubricants*, Bd. 7(10), Nr. 88, pp. 1-19, October 2019.
- [161] H. Shahmohamadi, M. Mohammadpour, R. Rahmani, H. Rahnejat, C. Garner und S. Howell-Smith, „On the boundary conditions in multi-phase flow through the piston ring-cylinder liner conjunction,“ *Tribology International* vol. 90, pp. 164-174, 2015.
- [162] Infinity USA, *Model K2 Distamax Long-Distance Microscope System*, Infinity USA, 2017.
- [163] ISO Standard 12233, *Photography–Electronic Still Picture Cameras–Resolution Measurements*, 2000.
- [164] K. Masaoka, T. Yamashita, Y. Nishida und M. Sugawara, „Modified slanted-edge method and multidirectional modulation transfer function estimation,“ *Optical Society of America*, Bd. 22, Nr. 5, pp. 6040-6046, 2014.
- [165] F. Scott, R. M. Scott und R. V. Shack, „The use of edge gradients in determining modulation-transfer functions,“ *Photography Science and Engineering*, Nr. 7, pp. 64-68, 1963.
- [166] R. A. Jones, „An automated technique for deriving mtf's from edge traces,“ *Photography Science and Engineering*, Nr. 11, pp. 102-106, 1967.
- [167] J. K. Roland, *A Study of Slanted-Edge MTF Stability and Repeatability*, Imatest LLC, 2995 Wilderness Place Suite 103, Boulder, CO, USA.
- [168] B. Peter, *sfrmat 2.0 (open source Matlab code, download: <http://losburns.com/imaging/software/SFRedge/sfr2.zip>)*, 2003.
- [169] C. Bo, Z. Liu und J. Wang, „A new model of image segmentation with multi-threshold,“ *Journal of Chemical and Pharmaceutical Research*, pp. 836-853, 2014.
- [170] S. Howell-Smith, H. Rahnejat, P. D. King und D. Dowson, „Reducing in-cylinder parasitic losses through surface modification and coating,“ *Proceedings of the Institution of Mechanical Engineers Part D Journal of Automobile Engineering*, Bd. 228, Nr. 4, pp. 391-402, 2014.

- [171] S.-C. Vladescu, A. Ciniero, K. Tufail, A. Gangopadhyay und T. Reddyhoff, „Optimization of Pocket Geometry for Friction Reduction in Piston–Liner Contacts,“ *Tribology Transactions*, Bd. 61, Nr. 3, pp. 522-531, 2018.
- [172] P. Mishra und P. Ramkumar, „Effect of Micro Texture on Tribological Performance of Piston Ring-Cylinder Liner System under Different Lubrication Regimes,“ *SAE Technical Paper 2018-28-0052*, 2018.
- [173] M. Zimmer, S.-C. Vladescu, L. Mattsson, M. Fowell und T. Reddyhoff, „Shear-area variation: a mechanism that reduces hydrodynamic friction in macro-textured piston ring liner contacts,“ *Tribology International 107067*, Bd. 161, 2021.
- [174] A. Ronen, E. Izhak und Y. Kligerman, „Friction-Reducing Surface-Texturing in Reciprocating Automotive Components,“ *Tribology Transactions*, Bd. 44, Nr. 3, pp. 359-366, July 2001.
- [175] I. H. Malitson, „Interspecimen comparison of the refractive index of fused silica,“ *Journal of the Optical Society of America*, Bd. 55, Nr. 10, pp. 1205-1209, 1965.
- [176] A. M. Abdul-Munaim, M. Reuter, M. Koch und D. G. Watson, „Distinguishing Gasoline Engine Oils of Different Viscosities Using Terahertz Time- Domain Spectroscopy,“ *Journal of Infrared, Millimeter, and Terahertz Waves*, Bd. 36, Nr. 7, pp. 687-696, 2015.
- [177] S. Wigger, T. Müller und H.-J. Füsler, „Tribologieanalyse der Kolbengruppe mittels optisch zugänglichem Forschungsmotor,“ *MTZ - Motortechnische Zeitschrift*, Bd. 78, pp. 46-51, 2017.
- [178] T. Müller, S. Wigger, H.-J. Füsler und S. A. Kaiser, „Optische Untersuchung der Schmierungsverhältnisse im Reibkontakt Kolbenhemd/Zylinderlaufbahn mittels laserinduzierter Fluoreszenz an einem optisch zugänglichen Einzylindermotor,“ *Tribologie und Schmierungstechnik*, Bd. 6, Nr. 64, pp. 35-42, 12 2017.
- [179] J. Schöler, S. Wigger und S. A. Kaiser, „Quantitative fluorescence-based imaging of in-cylinder fuel film thickness at kHz frame rates in a production-type direct-injection spark-ignition engine,“ *International Journal of Engine Research*, Bd. 24, Nr. 6, pp. 2489-2504, 2023.
- [180] J. F. Heimrath, *Bildgebende Temperaturmessung in dünnen Ölfilmen durch Fluoreszenzspektroskopie*, Fakultät für Ingenieurwissenschaften, Abteilung Maschinenbau und Verfahrenstechnik Universität Duisburg-Essen, 2020.

- [181] ©FARO Technologies Inc., *FARO Gage Manual*, 2011.
- [182] Physikalisch Technische Bundesanstalt, *Kalibrierung von Kraftmessgeräten : Richtlinie DKD-R 3-3*, Braunschweig, 2018.
- [183] Physikalisch Technische Bundesanstalt, *Kontinuierliche Kalibrierung von Kraftaufnehmern nach dem Vergleichsverfahren: Richtlinie DKD-R 3-9*, Braunschweig, 2018.

8 Appendix

8.1 Redesign, adjustment, and calibration of the 90°-rotated tribometer

In chapter 4.1.1, Figure 4.3, CAD models of the previous- and 90° rotated tribometer are shown. The PRS and its relevant parts (mainly the bottom parts) were rotated, but the cylinder liner and its spindle adapter remained as a reference axis. In order to fasten and to adjust the bottom housing precisely after redesign, some supplemental parts were designed. As shown in Figure 4.3b and Figure 8.1, a steel precision plate with the flatness in a tolerance range of $\pm 10 \mu\text{m}$ was placed under the bottom housing to support the rotated system. The mounting brackets link the precision plate to the remaining posts. For an accurate adjustment of the housing and the piston ring segment's position in a few μm region, lateral and back-and-forth adjustment adapters were used. Each adapter's main plate was fixed to the steel precision plate and the fine adjustment screw pushed the housing. Here, a screw's rotation of 360° corresponded to the 1 mm movement. After a rough fix of the housing, the FaroArm®, which is described below, measured the precise position of the PRS on the housing and then the housing's position was modified by the adjustment adapter. This procedure could be repeated if necessary and is discussed in more detail below.

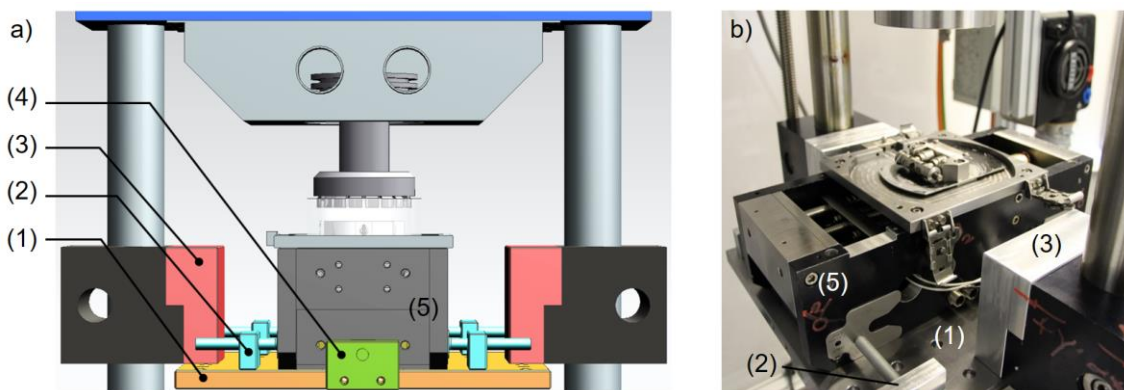


Figure 8.1: a) CAD model (side view) and b) photo of the 90° rotated tribometer. (1) Steel precision plate, (2) Lateral adjustment adapter, (3) Mounting bracket, (4) Back-and-forth adjustment adapter, (5) Bottom housing.

Precise adjustment with FaroArm®

FaroArm® (Gage plus, ©FARO Technologies Inc.), shown in Figure 8.2, is a portable 3D-coordinate measuring system with a spherical working distance of 1.2 m and with an accuracy of 0.018 mm [181].

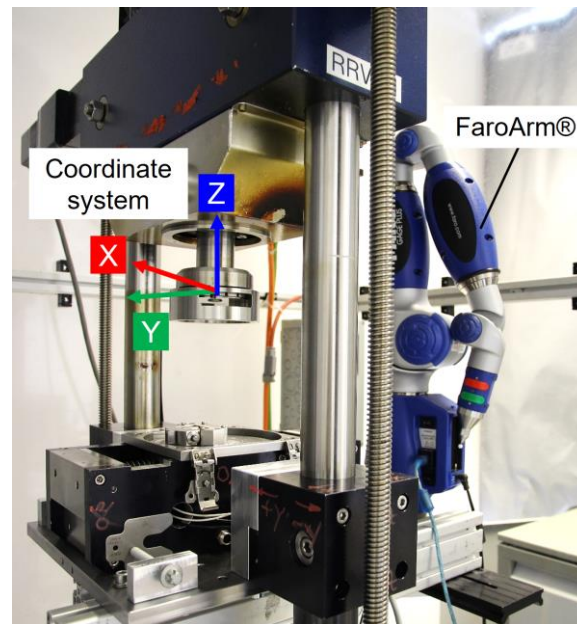


Figure 8.2: FaroArm® setup nearby the RRV tribometer and the virtual coordinate system.

At the end of the gage, a probe takes measurement points on command and there is a rotary encoder at each joint. The user clicks a button to record a point, the encoders compute the exact position of the probe in three-dimensional space and this point is recorded in the software. Faro's software, CAM2GAGE, measures basic geometry and building dimensions. It allows measuring geometric features on the part and setting the user-defined, virtual 3D-coordinate based on the measured features.

With this FaroArm®, the rotated and reconstructed parts of the tribometer were precisely adjusted in a few micrometer range to achieve a line contact between the PR/CL and to ensure the lateral centrality of the contact line on the piston ring segment's surface. We note that the spindle adapter holding the cylinder liner was not rebuilt; therefore, it is able to act as a standard coordinate. Figure 8.3 shows the process of the adjustment.

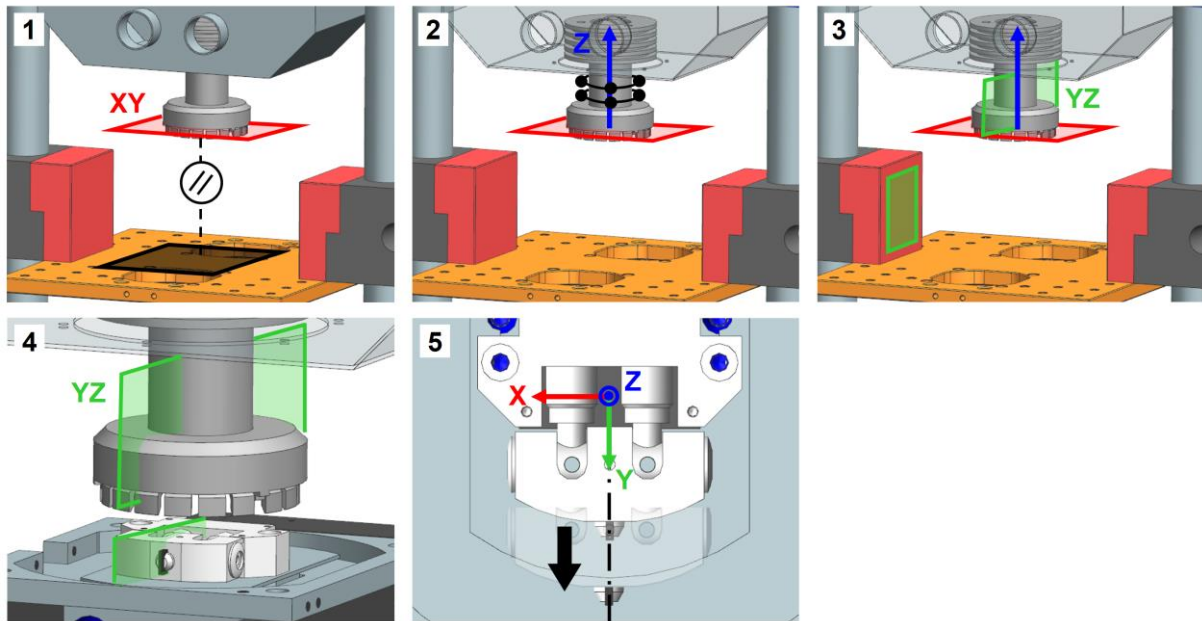


Figure 8.3: Mechanical adjustment process with FaroArm®, setting a virtual coordinate system on the tribometer.

Step 1: As shown in Figure 8.3, first image, three points on the bottom surface of the spindle adapter were measured to create a virtual XY-plane as a datum plane. After that, another virtual plane on the steel precision plate was measured with three points on it to control the parallelism of the two surfaces. The precision plate was then adjusted by the mounting screws so that the control surface (precision plate) lied within the acceptable tolerance zone. The measured tolerance was $18\ \mu\text{m}$, which corresponds to the accuracy of the FaroArm® Gage itself.

Step 2: In order to create a Z-axis, the cylinder form of the spindle adapter was measured with 6 points as shown in the second image in Figure 8.3. The Z-axis was then given as the centerline of this cylinder and is perpendicular to the XY-plane.

Step 3: Next step is to create an YZ-plane. In order to set the Y-axis in the direction of the piston ring segment's movement, the outer surface plane (green) of the red mounting bracket in the third image in Figure 8.3 was measured with three points on it. Based on this plane, a parallel virtual YZ-plane was determined, which included the Z-axis and was naturally perpendicular to the XY-plane. Consequently, the complete standard coordinate system was placed at the bottom surface and at the centerline of the spindle adapter.

Step 4: In this step, the standard coordinate system on the spindle adapter was selected as a reference. Based on that, the piston ring segment's position was corrected using the lateral adjustment adapters and the bottom mounting screws, which fix the bottom housing to the precision plate. For this, the PRS within its holder was pulled back to its start-position (unloaded) with the tribometer control system, which means that there exists no contact

between the PR/CL, if the liner were mounted. After that, the distance between the YZ-plane and a point on one of the sides of the PRS was repeatedly measured, while adjusting to ensure that the central plane of the PRS lay on the YZ-plane. Ideally, the distance ought to be 1.000 mm. As a result, the PRS was centered with a tolerance of 16 μm by the repeated measurements.

Step 5: Finally, the PRS and its holder moved forward in y-direction and at different positions, the same measuring process in the step 4 was repeated. The accuracy of the PRS's lateral centrality in this step was within the tolerance range of 8 μm .

Calibration of the sensors

After the mechanical adjustment, it is also necessary to calibrate the normal- and friction force sensors to avoid a possible improper zero reference or a shift in sensor's range during the reconstruction of the tribometer. For that, a sensor calibration device was newly designed for the RRV tribometer, which will be discussed more in detail below.

The calibration is conducted as following: first, an external force is given by the system (by the tribometer in the case of normal force, and by a linear actuator in the case of friction force) to the external calibration sensor and the internal sensors equipped in the tribometer simultaneously. The force signal from the external sensor is recorded and compared to that from the internal sensor. These characteristic curves of the signals are evaluated and the optimized correction values from the deviations are determined in a Matlab script. The offset-values are corrected via various potentiometers in the measurement amplifier. Here, the goal is to adapt the force signal from the internal sensors equipped in the tribometer to the target force signal from the external calibration sensors. Finally, the same procedure with the new calibrated values is repeatedly performed to check the minimal deviations. If necessary, it can be repeated multiple times. The procedure is similarly described in DKD-R 3-3 [182] and DKD-R 3-9 [183] guideline.

Figure 8.4 and Figure 8.5 show the newly designed set of the sensor calibration device. In Figure 8.4a, a motor mount was constructed to hold the linear actuator shown in Figure 8.5. The linear actuator gives a friction force through the rocker arm and this can be detected simultaneously by the external friction force sensor mounted on the rocker arm and by the internal friction force sensors inside of the tribometer through the calibration segment shown in Figure 8.4b. On the other hand, the normal force (load) is given by the tribometer control system as moving the calibration segment forward and this is simultaneously detected by the internal normal force sensors, which lie inside of the tribometer and by the external normal force sensor mounted on the fastened part in Figure 8.4a.

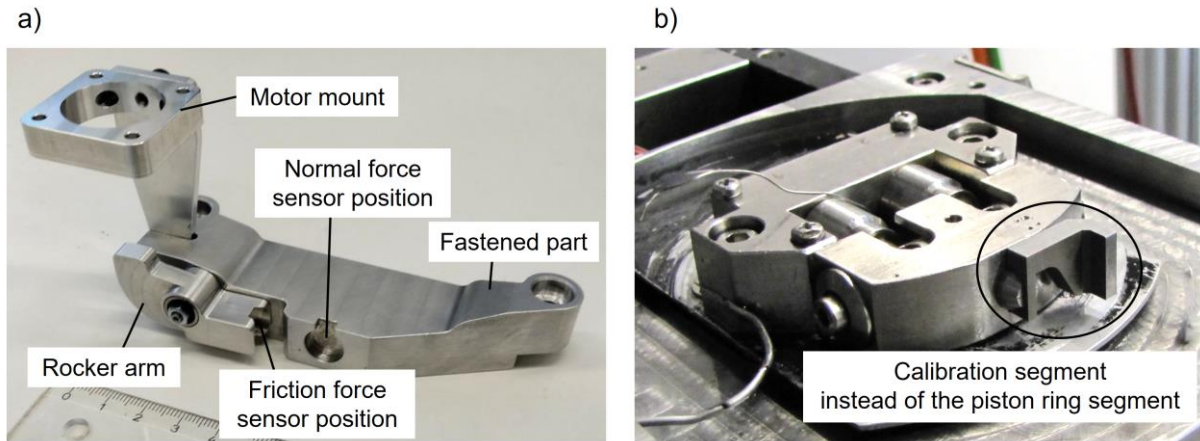


Figure 8.4: a) Newly designed sensor calibration devices. b) Newly designed calibration segment in the position of the piston ring segment.

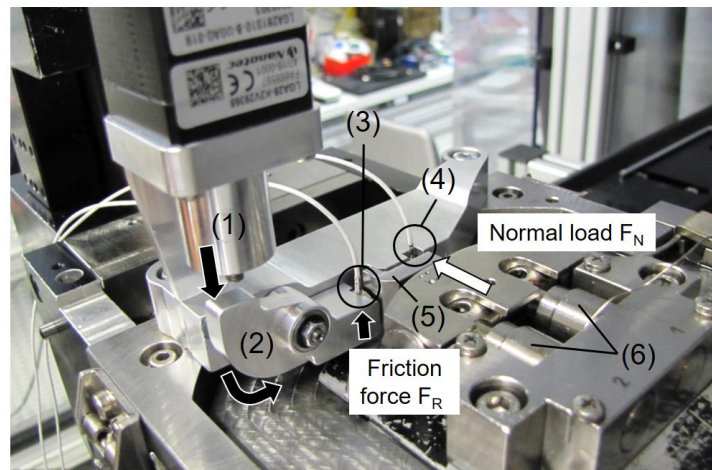


Figure 8.5: Assembled sensor calibration devices on the tribometer. (1) Linear actuator, (2) rocker arm, (3) external friction force sensor, (4) external normal force sensor, (5) calibration segment and (6) internal friction force sensors

The comparison procedure of the internal/external detected force signals is described in Figure 8.6a with the characteristic curves after some adjustments. The varied normal forces were given gradually in i), the internal detected force signal was described in ii) and each detected voltage from the two internal normal force sensors was compared in iii). As mentioned, the normal force is internally measured by two individual sensors (see Figure 3.4), expected to be split evenly (the internal friction force is the same). Overall, not only the internal- and external normal force signals, but also each voltage signal detected by the two internal normal force sensors was in close agreement with each other. Additionally, Figure 8.6b shows a best-fit of the internal/external measured normal forces and the blue dashed target line with the calculated correction points. It shows that the deviation between the internal force signal and the target signal is negligible. The calibration of the friction force sensors was carried out through the same process.

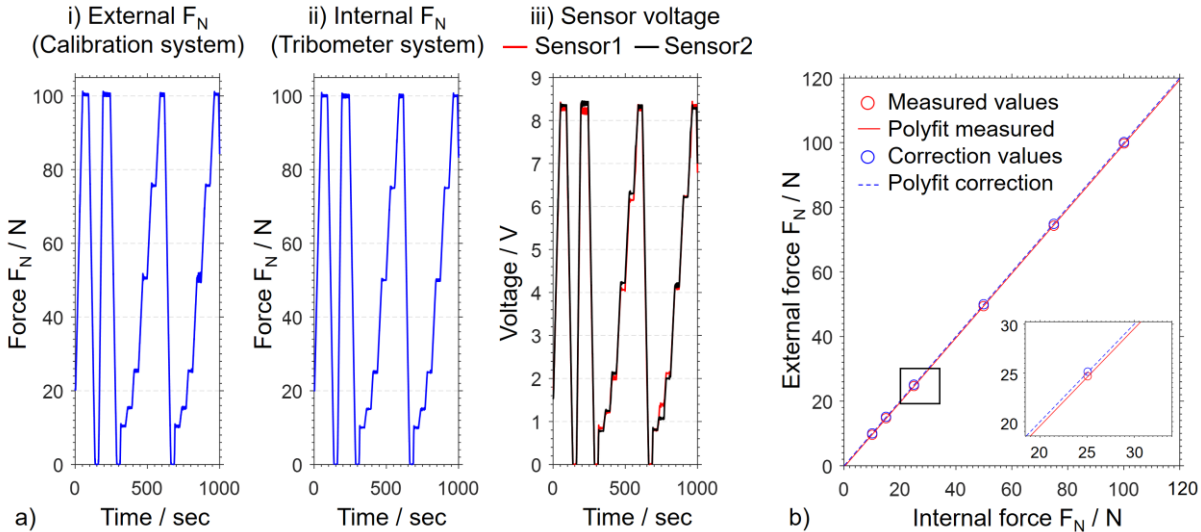


Figure 8.6: a) Example characteristic curves during the calibration procedure of the normal force sensors. b) Best-fit of the internal/external detected normal forces and the blue dashed target line with the calculated correction points in Matlab.

DuEPublico

Duisburg-Essen Publications online

UNIVERSITÄT
DUISBURG
ESSEN

Offen im Denken

ub | universitäts
bibliothek

Diese Dissertation wird via DuEPublico, dem Dokumenten- und Publikationsserver der Universität Duisburg-Essen, zur Verfügung gestellt und liegt auch als Print-Version vor.

DOI: 10.17185/duepublico/81742

URN: urn:nbn:de:hbz:465-20240328-142704-7

Alle Rechte vorbehalten.